Annual Report 2014

HI Jena

Helmholtz Institute Jena

Helmholtz Institute Jena
Fröbelstieg 3
07743 Jena
www.hi-jena.de

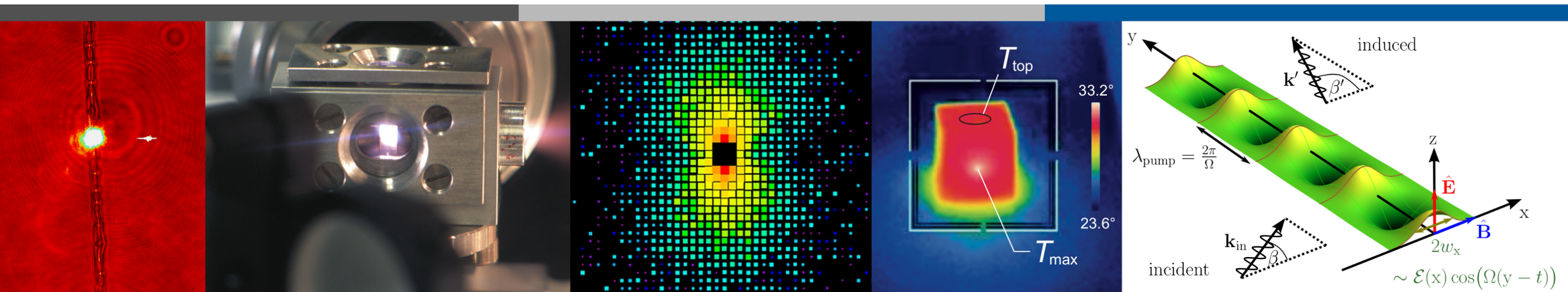

Helmholtz Institute Jena

Annual Report 2014

Contents

Introduction

The Helmholtz Institute Jena (HI-Jena) was founded in 2009 as a branch of the GSI Helmholtz Center for Heavy Ion Research located on the campus of the Friedrich-Schiller-University Jena (FSU). Since then, the combined expertise of the HI-Jena and its partner institutions on the development of high-intensity lasers, their applications for particle acceleration, and the detection and spectroscopy of high-energy photon and particle beams has promoted the HI-Jena to an internationally renowned centre for the physics of strong electromagnetic fields. This Annual Report for the year 2014 documents the excellence of the HI-Jena and the ongoing scientific progress. Highlights of this year include the development of the next generation of ultrafast fiber lasers, an upgrade and experiments on laser proton acceleration at POLARIS, accurate polarization measurements and theoretical studies on narrow band inverse Compton scattering x-ray sources, to highlight just a few. Much of the emphasis in 2014 was, however, placed on the HGF Programme-Oriented Funding, POF of the Helmholtz Association, in which the HI-Jena took part for the very first time (funding period 2015-2019). This was in particular challenging since the mother centre GSI was excluded from the evaluation due to its strong focus on the construction of FAIR. Within the research field “Matter”, the institute actively took part in both the programms “From Matter to Materials and Life (MML)” and “Matter and Technology (MT)”. In MML the contribution of HI-Jena has a clear focus on the In-house Research topic “Extreme States of Matter: From cold ions to hot plasmas” whereas in MT HI Jena concentrates on “Accelerator Research and Development” (with a small contribution to “Detector Technology and Systems“). An excellent rating has been achieved in both fields. With this success, the HI Jena with its strong link to the Friedrich-Schiller-University Jena is well recognized as partner of the large Helmholtz Centers in Darmstadt, Dresden and Hamburg. This role in supporting and forming a bridge between the large centers will continue to be the focus over the next years, underlining HI-Jena’s high visibility within the Helmholtz Alliance.

Two international conferences were organized by the HI-Jena together with the university and partners in Darmstadt and Gießen. The 9th ICAMDATA, an International Conference on Atomic and Molecular Data and Their Applications, continued a biannual series of international conferences to promote the use of atomic and molecular data in various fields of science and technology. This conference provides a forum for the interaction of data producers, database designers and compilers, and data users. It brought together experts from eighteen nations and from topics of astrophysics to fusion and plasma physics and up to biophysics, combustion and environmental sciences and technology. Moreover, a workshop of the Extreme Matter Institute EMMI on the Non-Exponential Two-Body Weak Decay has laid the ground for discussions about the ongoing research in storage-ring oscillations and their impact upon our understanding of neutrinos. In addition, HI-Jena together with DESY founded the spin-off company, Class 5 Photonics GmbH, which received the OptechNet start-up prize and Helmholtz Enterprise funding of the Helmholtz Association.

Finally, the Research School for Advanced Photon Science (APS) of the Helmholtz Institute continued their work in supporting young researchers. A highlight of this activity was a (second) lecture week in Buchenau, organized by APS in partnership with the Helmholtz Graduate School HGS-HIRe, bringing together 25 PhD students from five Universities with great interest in strong-field physics, and in line with the scientific program of the institute. This research school helps to educate the next-generation of scientists in strong-field physics and, hence, the further planning and preparation of the large facilities FAIR and XFEL within the next decade.

Research School of Advanced Photon Science of the Helmholtz Institute Jena

G. Weber[1,2], R. Märtin[1,2], Ch. Spielmann[3], and Th. Stöhlker[1,2,3]
[1]HI-Jena, Jena, Germany; [2]GSI, Darmstadt, Germany; [3]IOQ, University Jena, Jena, Germany

Among the most important tasks of the Helmholtz Institute Jena is the education and support of young scientists. The Research School of Advanced Photon Science (RS-APS) provides structured PhD education adapted to the research profile and organizational structure of the HI Jena. Emphasis is given to research being relevant for the international FAIR project in Darmstadt and the European XFEL facility in Hamburg, both being currently in the construction phase.

In 2014 about 25 PhD students (20 of them fully financed by RS-APS) were participating in the program of the research school. They were supervised by 14 principal investigators belonging directly to the Helmholtz Institute Jena or to institutes of the cooperating University Jena. Besides their doctoral work the students have the possibility to participate in the academic program which is offered directly by the Helmholtz Institute Jena and moreover they have access to the broad spectrum of courses provided by the cooperating graduate programs. More specifically, RS-APS is member of the graduate academy of the Jena university and additionally, the school is in close cooperation with both the Abbe School of Photonics, which resides at the Department for Physics and Astronomy (PAF), and the DFG graduate college "Quantum and Gravitational Fields". Moreover since 2013 the RS-APS is member of the Helmholtz Graduate School for Hadron and Ion Research (HGS-HIRe) which promotes structured PhD education for research associated with FAIR and GSI.

The regular on-site seminars of the Research School provide the students either a platform for presenting their recent results or meeting distinguished researchers in the field. Additionally in 2014 almost half of the students of the HI Jena participated in dedicated soft skill block courses offered by HGS-HIRe focusing on the strengthening the core competencies of young researchers. Furthermore students of the Helmholtz Institute attended so-called Power Weeks by HGS-HIRe. A Power Week is focused on a particular science topic. In contrast to a lecture week it is not interdisciplinary and therefore allows discussions on a much deeper level. In addition transferable skill courses offered on site by the graduate academy Jena have been visited, e.g. qualification in academic teaching.

One major event in 2014 was the second joint HGS-HIRe and RS-APS Lecture Week which took place in Buchenau Manor from November 16th to 20th. The whole week 25 students from RS-APS and HGS-HIRe dealt intensively with "X-ray spectroscopy as diagnostic tool in atomic and plasma physics". The PhD students have been supervised by the lecturers Alexander Gumberidze (EMMI and GSI), Paul Neumayer (GSI), Daniel Seipt (HI Jena) and Ulf Zastrau (University of Jena and LCLS, Stanford).

Figure 1: Participants of the joint lecture week at Buchenau Manor

The Research School of the HI Jena is not only supporting its students financially through scholarships but also every student has its own annual travel budget which he can spend individually. In 2014 more than two third of the doctoral candidates took use of this money for visiting international workshops and conferences to present their research results.

From the administrative point of view, the year 2014 brought a major improvement as all data of the students is now managed by a web-based system. Now the students can view and update their personal and academic data via the internet. Final adjustments of the new management system will take place in the upcoming months. We expect a significant gain in productivity and convenience compared to the old 'paper sheet based' system.

High Power Laser Development

100 TW upgrade and operation of the POLARIS laser system

M. Hornung[1,2,#], H. Liebetrau[2], S. Keppler[2], A. Kessler[1], J. Polz[2], M. Reuter[2], G.A. Becker[2], J. Reislöhner[2], F. Schorcht[1], M. Hellwing[2], J. Hein[1,2], M.C. Kaluza[1,2]

[1]Helmholtz Insitute Jena, Germany; [2]Institute of Optics and Quantum Electronics, Jena, Germany.

We report on the operation and an upgrade of POLARIS [1,2], which allows for daily operation on a 100 TW level. In 2014, three extensive experimental campaigns were performed using the POLARIS laser system.

Starting in December 2013 an experiment with cryogenically cooled, mass-limited hydrogen targets (see Fig. 1) was performed with A4-amplified laser pulses with 30 TW output power. This experiment lasted until May 2014 and was followed by the final commissioning of the last POLARIS amplifier A5 [3]. During this commissioning, the A5-pulses were compressed, the wavefront was adapted and finally the pulses were focussed by a f = 2 m off-axis parabola to meet the requirements of the following experiment. From June to September an electron acceleration campaign was accomplished with either A4 or A5 amplified laser pulses. Here a gas-cell was used as a target (e.g. H_2-gas).

The third experiment in 2014, starting in October lasting to February 2015, was a campaign with either ultra-thin, mass limited or cone targets. For this experiment, the 1030 nm POLARIS pulses were frequency-doubled to 515 nm with a large aperture KDP-crystal and focussed with a f = 300 mm off-axis parabola. The polarization of the 515 nm pulses could be varied from linear to circular.

Including low energy alignment pulses the POLARIS laser was used on 83% of the working days in 2014 for the realization of high-intensity experiments. As a result of the experimentalist's requirements and the commissioning of A5, POLARIS was used on 76 days with full power A4 pulses and 55 days with A5 pulses.

During the final commissioning of the last POLARIS amplifier A5 [3] we optimized this amplifier with respect to stability and long term operation. The obtained near field profile was furthermore adapted to the pulse compressor in order to achieve a minimal fluence on the compression gratings. After compression, a minimal pulse duration of 143 fs (FWHM) was measured in a single shot second harmonic autocorrelator. This measurement is shown in Fig. 2.

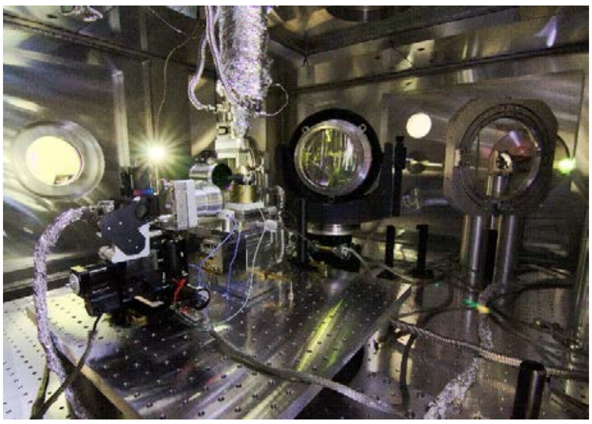

Figure 1: Photography of the POLARIS target chamber with 250 mm diameter turning mirrors, focussing parabola and installed hydrogen droplet source.

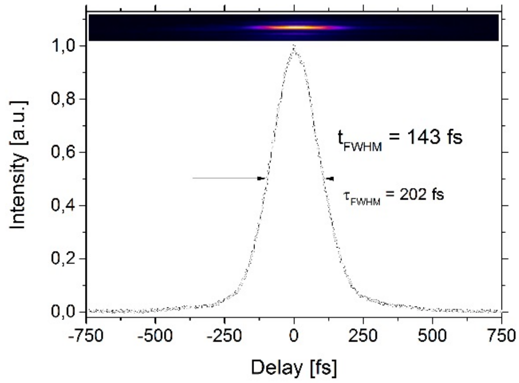

Figure 2: Second order far field autocorrelation measurement of the full amplified and compressed A5 laser pulses.

Up to now, we achieved a pulse energy of 20.3 J (before compression, 14 J on target), which is limited by the fluence of 4 J/cm^2 on the Yb:CaF_2 crystal used in A5. Focusing with a f=300 mm off-axis parabola leads to a FWHM focal spot size of 8 µm^2 and a peak intensity in excess of 6x10^{20} W/cm^2. This is to the best of our knowledge the highest peak power and intensity achieved so far with a diode-pumped laser system.

References

[1] M. Hornung, H. Liebetrau, A. Seidel, S. Keppler, A. Kessler, J. Körner, M. Hellwing, F. Schorcht, D. Klöpfel, A. K. Arunachalam, G. A. Becker, A. Sävert, J. Polz, J. Hein, and M. C. Kaluza, "The all-diode-pumped laser system POLARIS – an experimentalist's tool generating ultra-high contrast pulses with high energy", High Power Laser Science and Engineering **2**, e20 (2014).

[2] H. Liebetrau, M. Hornung, A. Seidel, M. Hellwing, A. Kessler, S. Keppler, F. Schorcht, J. Hein, and M. C. Kaluza, "Ultra-high contrast frontend for high peak power fs-lasers at 1030 nm" Optics Express 22, 24776 (2014).

[3] A. Kessler, M. Hornung, S. Keppler, F. Schorcht, M. Hellwing, H. Liebetrau, J. Körner, A. Sävert, M. Siebold, M. Schnepp, J. Hein, and M. C. Kaluza, "16.6 J chirped femtosecond laser pulses from a diode-pumped Yb:CaF_2 amplifier", Optics Letters, Vol. 39, Issue 6, pp. 1333-1336 (2014).

[#] Marco.Hornung@uni-jena.de

Second Harmonic Generation with the POLARIS Laser Pulses

M. Hornung[1,2,#], G.A. Becker[2], J. Reislöhner[2], A. Seidel[1], H. Liebetrau[2], S. Keppler[2], L. Bock[2], A. Kessler[1], F. Schorcht[1], M. Hellwing[2], J. Hein[1,2], M. Zepf[1,2], M.C. Kaluza[1,2]

[1]Helmholtz Insitute Jena, Germany; [2]Institute of Optics and Quantum Electronics, Jena, Germany.

We present experimental results of the second harmonic generation (SHG) of 100-TW POLARIS laser pulses centred at 1030 nm wavelength. Due to the nonlinearity of the second harmonic generation, the original laser pulse temporal profile is shortened and cleaned. The results were obtained during a five-month experimental campaign starting at the end of September 2014. In this experiment, ultra-thin targets (down to 5 nm) were used to study proton acceleration processes with high intensity laser pulses.

To increase the temporal contrast of the pulses [1,2] a 160 mm-diameter, 2 mm-thick potassium dihydrogen phosphate crystal (KDP) was used to convert the 1030 nm centre wavelength pulses to 515 nm. Gooche & Housego (Ohio, USA) manufactured the crystal with a crystal-cut angle of 41°. For optimal long-term and laser performance the input surface is SolGel AR-coated for 1030 nm and the output surface is SolGel AR-coated for 515 nm and 1030 nm, respectively. The polarization of the fundamental pulses is orientated horizontally in the target chamber and the newly generated SHG-pulses are polarized vertically.

In order to separate the fundamental pulses from the SHG pulses two high quality wavelength separators were installed between the KDP-crystal and the focussing parabola. These wavelength separators are 250 mm diameter, 45° angle of incidence turning mirrors with a high reflectivity (R>99.9%) for the SHG-pulses at 515 nm and a low reflectivity (R<0.1%) for the fundamental pulses at 1030 nm. Using two of these mirrors, which were manufactured by Layertec (Mellingen, Germany), the fundamental pulses could be attenuated by 6 orders of magnitude which was measured with an energy meter. A photography of the KDP crystal and a wavelength separator is shown in Figure 1.

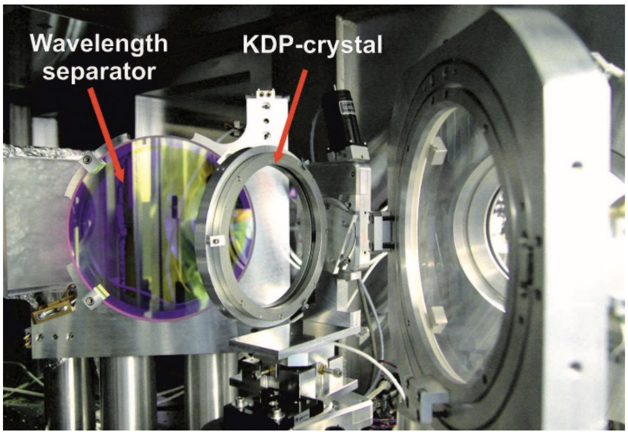

Figure 1: Photography of the KDP-crystal and one wavelength separation mirror to suppress the fundamental wave.

During the experiments, the KDP-crystal was illuminated with fully amplified and compressed laser pulses with a pulse energy of up to 14 J and a pulse duration down to 144 fs. For 10 J pulses, we typically measured a fluence of 200 mJ/cm^2 on the crystal, which results in a conversion efficiency of 25%. In Figure 2 the output pulse energy (515 nm) is plotted versus the input pulse energy.

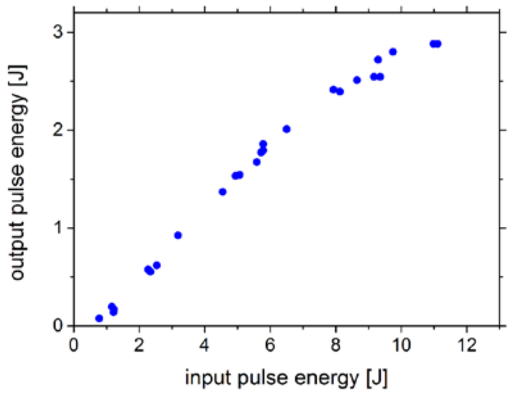

Figure 2: Output pulse energy at 515 nm wavelength vs. input pulse energy at 1030 nm.

The pulse duration of the converted laser pulses with respect to fundamental pulses is reduced by a factor of $\sqrt{\mathbf{2}}$, which was measured with a small-size KDP sample in a separate setup. To focus the 515 nm pulses we used a 300 mm off-axis parabola, which leads to a focal spot size with ~ 7 µm^2 FWHM focal spot area [2]. Furthermore, the temporal intensity contrast 200 ps before the arrival of the main laser pulse is estimated to be better than 10^{17}, which is a very high temporal contrast. With this ultra-high temporal contrast 5 nm thin diamond-like carbon foils could be successfully used as targets during the experimental campaign.

References

[1] M. Hornung, H. Liebetrau, A. Seidel, S. Keppler, A. Kessler, J. Körner, M. Hellwing, F. Schorcht, D. Klöpfel, A. K. Arunachalam, G. A. Becker, A. Sävert, J. Polz, J. Hein, and M. C. Kaluza, “The all-diode-pumped laser system POLARIS – an experimentalist’s tool generating ultra-high contrast pulses with high energy”, High Power Laser Science and Engineering **2**, e20 (2014).

[2] H. Liebetrau, M. Hornung, A. Seidel, M. Hellwing, A. Kessler, S. Keppler, F. Schorcht, J. Hein, and M. C. Kaluza, “Ultra-high contrast frontend for high peak power fs-lasers at 1030 nm“ Optics Express 22, 24776 (2014).

Marco.Hornung@uni-jena.de

Current status of the JETi 200 laser system

A. Sävert[1,2], G. Schäfer[2], B. Beleites[2], F. Ronneberger[2], M.C. Kaluza[1,2], M. Zepf[1], V. Bagnoud[1,3], T. Stöhlker[1,3]

[1]Helmholtz Institut Jena, Germany, [2]Friedrich-Schiller-Universität Jena, Germany, [3]GSI Darmstadt, Germany

One of the central research pillars of the Helmholtz Institute Jena is the field of laser-particle acceleration. The JETi 200 laser system with key parameters of 4J of compressed laser energy and <20 fs pulse duration is now routinely running at the Helmholtz Institute Jena. During the last year, significant improvements concerning the beam quality and temporal contrast were achieved. It became apparent that the beam quality and consequently the minimal achievable focal spot size depends on the repetition rate of the laser. When either operating in single shot mode or at 1 Hz, the wave front remains undisturbed. However, when operating at 5 Hz and over a time span of 10 min an astigmatism is introduced into the beam. As a major cause for this aberration, the vacuum windows in the cryogenic cooled amplifier were identified. The combined thermal load of the pump lasers (5x 5 J in 10 ns) and the amplified laser beam itself (4 passes, final energy 6 J) leads to stress in the windows made of BK7 equivalent glass, see Figure1.

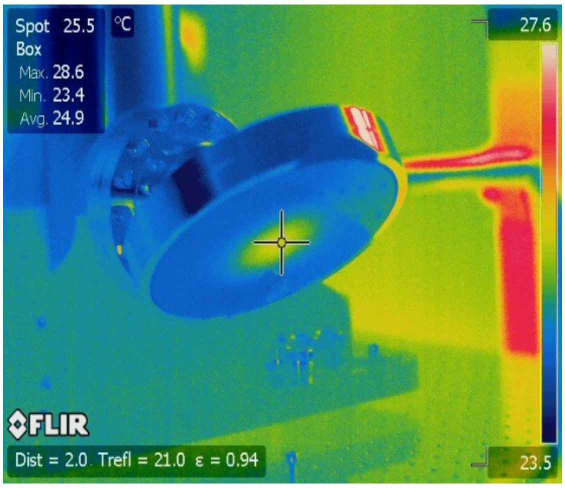

Figure 1: Temperatur rise in the vacuum windows under full power.

Together with the system's supplier, Amplitude System, the glass was exchanged to an IR grade fused silica variant with low residual hydroxide. Now the wave front remains undisturbed for all different repetition rate of the laser. Focussing the beam with an F/15 off-axis parabola results in a focal spot with a diameter of 17 µm (FWHM), see Fig. 2.Within the FWHM, 27% of the total energy are included. Installing a deformable mirror, which is planned for the next year, will increase the spatial contrast and double the peak intensity.

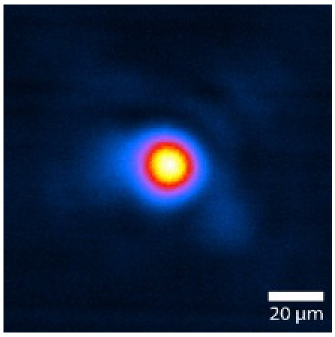

Figure 2: Focal spot of broad bandwidth (90 nm), 17 fs laser pulses.

The shape of the focal spot and the spatial contrast play a crucial role in the ultra high intensity regime ($I > 10^{21}$ Wcm^{-2}) as instabilities can grow before the peak in laser intensity is reached and therefore lead to non-reproducible experimental results. The temporal contrast of the JETi200 laser pulses was also improved as shown in Fig. 3.

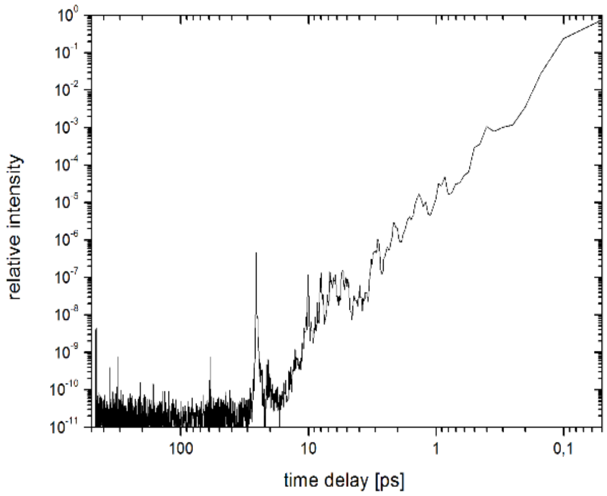

Figure 3: Temporal contrast of the full amplified beam.

The seed pulses for the XPW are now as short as 30 fs with a nice gaussian spectral distribution and generate a broad spectrum sufficient for a final pulse duration of < 17 fs. Simultaneously, the temporal contrast was also improved and the ASE level is in the order of 10^{-11} with only a small number of prepulses with identified sources. After completion of the new beam line to the target area, first experiments are scheduled for late summer 2015.

The generation of ASE in high-power CPA laser systems - a comparative study for various solid state laser materials*

S. Keppler†[1], *A. Sävert*[1], *J. Körner*[1], *H. Liebetrau*[1], *M. Hornung*[1,2], *J. Hein*[1,2], *and M. C. Kaluza*[1,2]
[1]Institute of Optics and Quantum Electronics, FSU Jena, Germany; [2]Helmholtz-Institute Jena, Germany

Relativistic laser-plasma physic utilizing high-intensity laser systems with peak intensities in excess of $I_0 = 10^{21}\,\mathrm{W/cm^2}$ were strongly investigated during the last decade. Higher pulse energies as well as shorter pulses lead to higher kinetic energies of accelerated electrons, protons and heavier ions. For this purpose, various classes of laser systems based on chirped pulse amplification (CPA) have been used. Key parameters of the different classes relevant for the experiments (e.g. wavelength, pulse duration and pulse energy) are well understood and can be compared directly. However, the temporal intensity contrast (TIC), which is one of the most crucial parameters for relativistic laser-plasma physics, has only been characterized for each individual laser system so far.

We developed a model which allows for a precise estimation of the TIC regarding the generation of amplified spontaneous emission (ASE) in different classes of laser systems. Based on the the easily accessible small signal gain averaged over the spectral bandwidth, $\bar{g}$, we calculated the fluorescence power P_1^{F}, which is emitted in the direction of the first amplifier pass to be:

$$P_1^{\mathrm{F}} \approx \bar{I}_{\mathrm{sat}} \frac{\Delta\Omega\, A}{4\pi}\, K_{\Delta\nu}\, p \log\left[\frac{\bar{g}}{1-L}\right], \qquad (1)$$

with $\bar{I}_{\mathrm{sat}}$ being the averaged saturation intensity of the considered laser medium. The parameter $\Delta\Omega\, A/4\pi$ describes the spatial and $K_{\Delta\nu}$ the spectral acceptance of the considered amplifier. p describes the probability of an emitted photon to match the polarization direction of the amplifier. Losses due to reabsorption or cavity losses are considered by the loss factor L, which allows for the description of reabsorbing 3-level materials, such as Yb^{3+}-doped materials as they are used in diode-pumped systems. Regarding the amplification of the TEM_{00}-mode only, which is the case in regenerative amplifiers commonly used for the pulse amplification to the mJ-level, the spatial acceptance is reduced to $\Delta\Omega\, A/4\pi = \lambda^2$. If the amplification dynamics are described by as a geometric series [1] the TIC can be estimated by [2]:

$$\mathrm{TIC}_{\mathrm{ASE}} = \frac{I_{\mathrm{ASE}}}{I_{\mathrm{pulse}}} \approx \frac{\bar{I}_{\mathrm{sat}}\lambda^2}{4\pi}\; p\, K_{\Delta\nu} \frac{\tau}{E_{\mathrm{in}}}, \qquad (2)$$

which only depends on the properties of the laser material and on the main pulse parameters such as the seed energy E_{in} and the final pulse duration τ. Since the RA supports only the TEM_{00} mode, the spatial characteristics of the main pulse and the ASE are identical. Hence, for eq. (2), a comparable focussing of the ASE and the main pulse was assumed, which was also measured experimentally [3]. Losses can be considered by multiplying eq. (2) with $(1 + L/(\bar{g} - 1))$.

Fig. 1 shows a comparison of various state-of-the-art laser materials such as Ti:Sapphire or Nd:glass and Yb^{3+}-doped materials like $\mathrm{Yb:FP20}$ or $\mathrm{Yb:CaF_2}$, which are used in the all-diode pumped laser system POLARIS. The study allows for a direct comparison of the minimal TIC which could be reached with a certain laser systems. Here we found, that Yb^{3+}-doped materials, suitable for high intensities with pulse durations around 100 fs, are also a promising alternative to state-of-the-art materials when the TIC is considered. Finally, the model was validated at two high-power laser system. The TIC measurements, carried out at the POLARIS (Yb:FP20) and the JETI (Ti:Sa) system are in excellent agreement to the presented model [2].

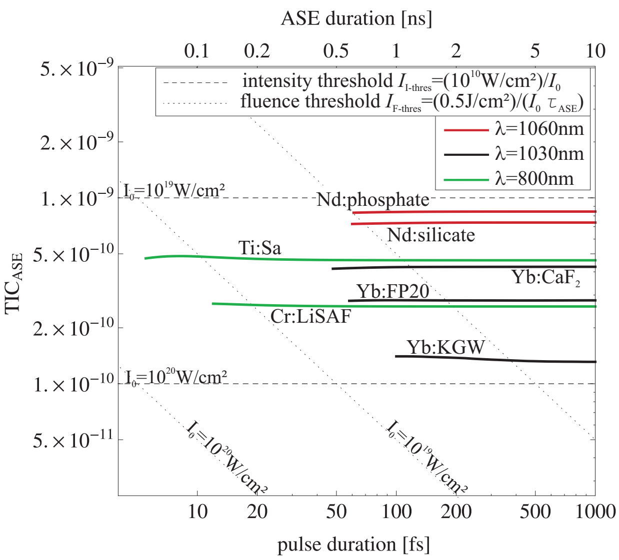

Figure 1: Comparative study of the TIC for common laser materials. Different colours indicate different laser wavelengths of the materials.

References

[1] V. V. Ivanov *et al.* Appl. Opt. **42**, 7231 (2003).

[2] S. Keppler *et al.* submitted

[3] S. Keppler *et al.* Opt. Express **22**, 11228 (2014).

*Work supported by the European Commisions (EC) 7^{th} Framework Programme (LASERLAB-EUROPE, grant no. 228334) and the Bundesministerium für Bildung und Forschung (BMBF) (03ZIK445 and 03ZIH531).

† Sebastian.Keppler@uni-jena.de

Multidimensional Amplification of Ultrashort Pulses

M. Kienel[1,2], M. Müller[1], A. Klenke[1,2], T. Eidam[1,2], J. Limpert[1,2,3], and A. Tünnermann[1,2,3]
[1]Institute of Applied Physics, Abbe Center of Photonics, Friedrich-Schiller-Universität Jena, Albert-Einstein-Str. 15, 07745 Jena, Germany;
[2]Helmholtz-Institute Jena, Fröbelstieg 3, 07743 Jena, Germany;
[3]Fraunhofer Institute for Applied Optics and Precision Engineering, Albert-Einstein-Str. 7, 07745 Jena, Germany

Scaling the performance of ultrafast high-power fiber-laser systems is challenging, since nonlinear pulse distortions and optically induced damage caused by the high peak intensities in the fiber core set an upper limit for the achievable pulse energies. Increasing the guided beam diameter and applying chirped-pulse amplification (CPA) can mitigate these effects to a certain amount. However, a further increase in mode-field diameter and the stretched pulse duration becomes more and more challenging.

Coherent beam combination (CBC) and divided-pulse amplification (DPA) are promising approaches to scale the achievable pulse peak power beyond the limitations of a single amplifier by applying spatial or temporal multiplexing [1]. Here, the laser pulses are spatially or temporally split prior amplification and coherently combined afterwards. In particular for DPA, typically passive double-pass implementations are used. However, for these setups the achievable pulse energy is restricted by saturation of the amplifier leading to a deformation of the pulse train. This additionally causes differences in the nonlinear phase (B-integral) among the replicas and, hence, a degradation of the combination efficiency. A solution is to separate the pulse division from the pulse combination in actively stabilized DPA, referred to as ADPA. Due to the increased number of degrees of freedom the input pulse train can be shaped independently from the output to pre-compensate for the deformation.

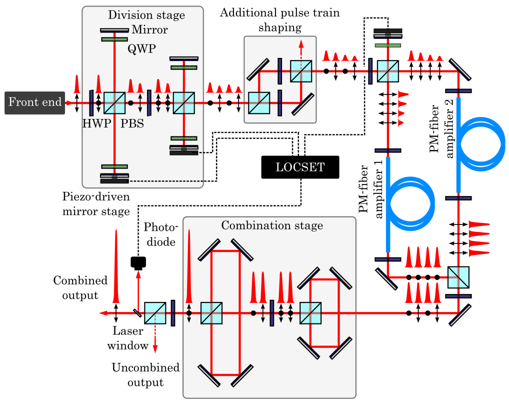

Fig. 1: Scheme of the multidimensional architecture (PBS - polarizing beam splitter, HWP - half-wave plate, QWP - quarter wave plate, PM – polarization maintaining).

* This work has been partly supported by the German Federal Ministry of Education and Research (BMBF) under contract 13N12082 “NEX-US,” contract 13N13167 “MEDUSA” and by the European Research Council under the ERC grant agreement no. [617173]. A. K. and M. K. acknowledge financial support by the Helmholtz- Institute Jena. T. E. acknowledges financial support by the Carl-Zeiss Stiftung.
† jens.limpert@uni-jena.de

We demonstrated in a proof-of-principle experiment the combination of both spatially and temporally multiplexing, meaning CBC and ADPA, in a scalable multidimensional amplification scheme of stretched femtosecond pulses [2], which is schematically depicted in Fig. 1. In particular, using interferometric free-space delay lines consisting of polarizing beam splitters and wave plates up to four temporally delayed pulse replicas were generated. Additionally, this pulse train is divided in two 6 µm-core fiber-amplifier channels. After amplification, all generated pulse replicas are recombined in a similar manner as in the division, as shown in Fig. 2. To ensure efficient re-combination an active feedback control using the LOCSET technique is applied.

With this concept pulse energies of 37 µJ were extracted from the amplifiers, which is far beyond the damage threshold (12 µJ) of the single fibers. Moreover, even for strong saturation and a high nonlinear phase, excellent combination efficiencies of >77% could be demonstrated.

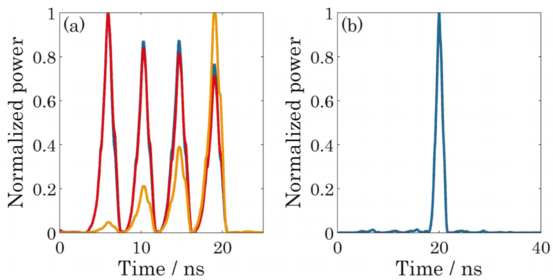

Fig. 2: (a) Photo-diode traces of the input pulse train (orange) and outputs of both amplifiers (red and blue) and (b) for the combined pulse at a pulse energy of 37 µJ.

In principle this technology is applicable not only to fibers but to any amplifier geometry. However, it is especially suited to fibers due to their simple single-pass setups and high gains. Thus, the next step will be employing advanced fiber designs that possess more than a factor of ten larger core diameters, which will scale the achievable pulse energy to the multi-mJ range. We are confident, increasing the channel and replica count will make TW-class fiber lasers for laser particle acceleration feasible in the near future.

References

[1] J. Limpert, A. Klenke, M. Kienel, S. Breitkopf, T. Eidam, S. Hädrich, C. Jauregui, and A. Tünnermann, IEEE JSTQE **20**, 268 (2014).

[2] M. Kienel, M. Müller, A. Klenke, T. Eidam, J. Limpert, and A. Tünnermann, Opt. Lett. **40**, 522 (2015).

Ultrafast thulium-based fiber laser systems with high peak and average powers*

M. Gebhardt[1,2], C. Gaida[1], F. Sutzki[1], S. Hädrich[1,2], J. Rothhardt[1,2], C. Jauregui[1], J. Limpert[#1,2,3], and A. Tünnermann[1,2,3]

[1]Institute of Applied Physics, Abbe Center of Photonics, Friedrich-Schiller-Universität Jena, Albert-Einstein-Str. 15, 07745 Jena, Germany; [2]Helmholtz-Institute Jena, Fröbelstieg 3, 07743 Jena, Germany; [3]Fraunhofer Institute for Applied Optics and Precision Engineering, Albert-Einstein-Str. 7, 07745 Jena, Germany

High-performance, ultrafast laser systems with emission wavelengths longer than 1 µm are interesting driving sources for applications in high-field physics. In particular, high-harmonic generation can greatly benefit from these longer driving wavelengths due to the favourable scaling of the ponderomotive potential. In this regard, high-power thulium-based fiber lasers, which are operated around 1.9 µm, are promising sources for driving phase-matched high-harmonic emission processes with photon energies well within the water window and beyond (>300 eV) [1].

However, the complex structure of the atmospheric absorption causes challenges for the emission of high-power ultrashort-pulses around 1.9 µm. In this wavelength range a strong molecular water-vapor absorption band coincides with the gain bandwidth of thulium-doped silica leading to free-space propagation effects in both the spatial and the temporal domains. These effects manifest themselves in the form of significant distortions of the beam profile (due to thermal lensing in air) and in the form of a decrease in the pulse contrast (as governed by the Kramers-Kronig relations) leading to a dramatic reduction in beam quality and pulse peak power, respectively. A rigorous study revealed that minimizing the absolute humidity and the propagation distance within the laser system are key prerequisites for performance scaling of ultrafast two micron lasers [2].

High peak power

We have demonstrated a thulium-based ultrafast fiber laser system delivering 120 µJ pulses with a record peak power of more than 200 MW. This result was enabled by the mitigation of the aforementioned propagation effects and the use of advanced very-large-mode-area fibers. The main amplification stage consisted of a thulium-doped large-pitch photonic crystal fiber, which allows for robust single mode operation with a mode-field diameter larger than 60 µm [3]. Further key components of the experimental setup (Fig. 1) were a home-built fiber oscillator and high-efficiency dielectric gratings used in the stretcher and compressor stages.

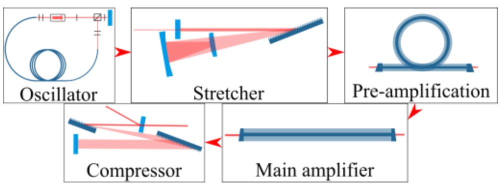

Figure 1: Schematic of the experimental setup.

*This work has been partly supported by the German Federal Ministry of Education and Research (BMBF)

#jens.limpert@uni-jena.de

The main amplification stage was operated at a repetition rate of 200 kHz. After amplification the pulses were compressed to a FWHM duration of ~360 fs. The impact of residual water-vapor absorptions on the pulse evolution can be predicted incorporating a self-developed simulation tool, which allows estimating the achieved pulse peak power to >200 MW (Fig. 2). This represents an increase by almost two orders of magnitude as compared to the previous generation of ultrafast two micron fiber lasers [4].

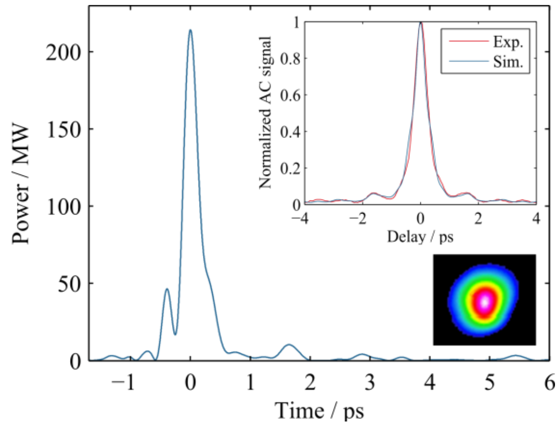

Figure 2: Retrieved pulse profile of the 120 µJ pulses. Insets: measured and simulated autocorrelation trace, image of the output beam profile

High average power

With a slightly modified setup [5] we have demonstrated the capability of ultrafast Tm-based laser systems to operate at high output average powers. At 49 MHz repetition rate a record compressed average power of more than 150 W in combination with sub-700 fs pulse duration was achieved.

Outlook Further power scaling and subsequent pulse peak power enhancements based on coherent combination and nonlinear compression will allow exploiting the full potential of Tm-based ultrafast fiber lasers for their applications. In particular, table-top high photon flux soft X-ray sources will be feasible by high-harmonic generation driven by these novel two micron fiber laser systems.

References

[1] T. Popmintchev et al., Science 336, 1287 (2012).
[2] M. Gebhardt et al., submitted to Optics Express (2015)
[3] F. Jansen et al., Opt. Lett. 37, 4546 (2012).
[4] R. A. Sims et al., Opt. Lett. 38, 121 (2013).
[5] F. Stutzki et al., Opt. Lett. 39, 4671 (2014).

Generation of multimillijoule redshifted beams for stimulated Raman scattering*

B. Landgraf[1,2], *A. Hoffmann*[1], *D. Kartashov*[2], *F. Gärtner*[3,4], *Z. Samsonova*[1,2], *P. Polynkin*[5], *J. Jacoby*[4], *T. Kühl*[1,3], *and C. Spielmann*[1,2]

[1]Helmholtz Institute Jena, Jena, Germany; [2]Institute of Optics and Quantum Electronics, Abbe Center of Photonics, Friedrich-Schiller University Jena, Jena, Germany; [3]GSI, Darmstadt, Germany; [4]Institute for Applied Physics, Plasmaphysics, Goethe-University Frankfurt/Main, Frankfurt/Main, Germany; [5]College of Optical Sciences, The University of Arizona,Tucson, USA

Introduction

Stimulated Raman backscattering (SRBS) is a possible candidate to overcome scaling limitations of state of the art chirped pulse laser amplifiers [1]. SRBS describes a three wave interaction in laser plasmas in which a plasma wave is generated due to the ponderomotive force of a beatwave originating from two counter-propagating and frequency shifted laser pulses. The frequency shift difference defines the optimal plasma frequency. To achieve an efficient energy transfer between the counter-propagating pulses a frequency difference between $5 - 10\%$ $(500 - 1500 cm^{-1}$, 50-100 nm for typical CPA systems) is necessary [2].

Redshift with stimulated Raman scattering

The necessary parameters for a seed beam are: i) a well-defined redshift which must be independent of the energy available; ii) a single spatial mode beam and iii) a pulse duration much shorter than the pump pulse. The introduced Group Velocity Mismatch (GVM) it is suitable to partially recompress the pulse and forego further recompression techniques. To support a high total energy output gases are ideally suited for this application. SF_6 provides a 100 nm redshift at 1053 nm ($775 cm^{-1}$).

Experimental results

The presented data [3] were collected in the XRay Lab at the PHELIX Laser facility. The laser provides up to 200 J in 500 fs at 1053 nm every 90 minutes. Figure 1 shows the aquired spectra. To generate the seed beam the energy was reduced to 0.1-0.4 J at the axicon every 3 minutes.

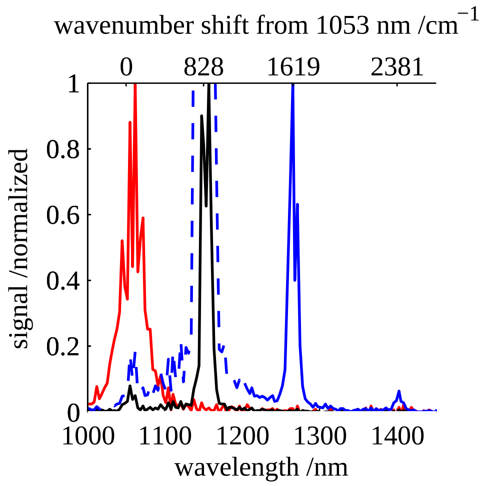

Figure 1: Spectral evolution of Raman shifted pulses using SF_6 with short (black line), long (blue dotted) caustic length, and Ar with significant spectral broadening for fundamental pulses at 1053 nm.

Conclusion

We characterized a simple but reliable method for the generation of redshifted seed beams for SRBS. The results show that with minimal alignment, fitting for few shot systems like PHELIX it is possible to generate customized high quality beams. The redshift is not energy dependent and tunable by the Raman medium and the order of the process used. Results show further a high absolute energy of the seed beam suitable to be used in the nonlinear Raman regime. With these seed source we are now in the favourable situation to complete our SRBS experiment at PHELIX, which will be a major step forward to realize a hight power pulse light source for studying the interaction of intense pulses with heavy ions, or dense plasmas generated with heavy ions, as available at FAIR.

* Work supported by GSI(PHELIX)/HI Jena/HGShire/European Regional Development Fund (EFRE)/state of Thuringia (TMBWK) under Grant No. B 715-08008/TR 18/US Air Force Office of Scientific Research through grants No. FA9550-12-1-0143 and No. FA9550-12-1-0482/US Defense Threat Reduction Agency through grant No. HDTRA 1-14-1-0009

References

[1] V. M. Malkin, G. Shvets, and N. J. Fisch. "Fast compression of laser beams to highly overcritical powers." Physical review letters 82.22 (1999): 4448.

[2] R. M. G. M. Trines, et al. "Simulations of efficient Raman amplification into the multipetawatt regime." Nature Physics 7.1 (2011): 87-92.

[3] B. Landgraf, et al. "Generation of multi-millijoule red-shifted pulses for seeding stimulated Raman backscattering amplifiers" Optics Express (2015) accepted.

Design and construction of a high repetition rate seeding laser for FLASH2*

H. Höppner[1], A. Hage[1], T. Tanikawa[1], R. Riedel[2,4], M. Schulz[1,4], F. Tavella[3], and M. J. Prandolini[† 2,4]
[1]DESY, Hamburg, Germany; [2]HI-Jena, Jena, Germany; [3]SLAC, Menlo Park, USA; [4]Class 5 Photonics GmbH, Hamburg, Germany

High repetition rate free-electron lasers (FEL), producing highly intense extreme ultraviolet (EUV) and X-ray pulses, require new high power tunable femtosecond lasers for FEL seeding and FEL pump-probe experiments. A tunable, 112 W (burst mode) optical parametric chirped-pulse amplifier (OPCPA) is demonstrated with center frequencies ranging from 720–900 nm, pulse energies up to 1.12 mJ and a pulse duration of 30 fs at a repetition rate of 100 kHz.

Introduction

Free-electron lasers (FEL) based on large scale linear electron accelerators are sources of highly intense extreme ultraviolet (EUV) and X-ray radiation. In particular, the development of high repetition rate FELs requires new optical laser developments to meet the needs of laser-induced FEL seeding and for lasers used in FEL pump-probe experiments. The future requirements of a tunable, high repetition rate laser with sufficient pulse energy can be met with optical parametric chirped-pulsed amplification (OPCPA). From FEL simulations using the package SIMPLEX covering a FEL wavelength range from 26.7 nm to 42.9 nm [1], the required seed laser energy should be around 1 mJ at a tunable range from 720–900 nm operating at 100 kHz in the burst mode of FLASH2.

Results

For high power (mJ pulse energy) OPCPA applications, a three stage OPCPA setup was used. The first stage amplifies the signal pulses from the nJ to the μJ level with a gain between 10^4 and 10^5. This reduces the amplified parametric fluorescence in the second and third stages, where 90% of the pump energy is used. The gain in the second and third stages is in the range of 50-100 and 2 for the second and third stages respectively. This system was pumped using a Yb-based fiber laser from Helmholtz-Institut Jena reaching 50 W and a booster InnoSlab amplifier from AMPHOS reaching a final output power of 1.5 kW [1]. Both the OPCPA and the pump laser were seeded with a Ti:Sa ultrabroadband oscillator from Venteon.

The OPCPA signal was prepared using a SF57 prism pair to achieve approximately 30 fs pulses across a broad spectrum with approximately 1 mJ of pulse energy (Fig. 1). The output pulses demonstrated excellent beam quality (see

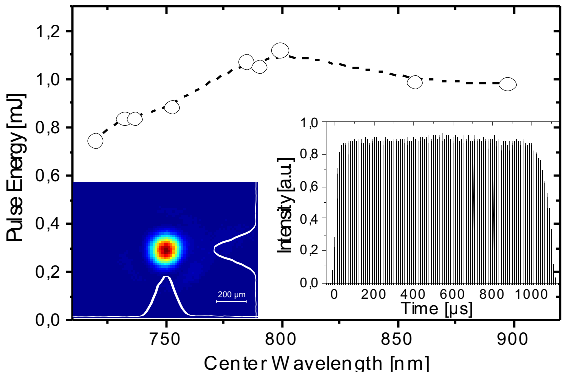

Figure 1: The dependence of pulse energy on center wavelength for the three-stage OPCPA system. Insert Left: Far-field beam profile at 800 nm. Insert Right: Typical 100 kHz burst structure of the OPCPA.

Fig. 1, left insert). From the caustic measured in both transversal directions, an M^2 of 1.1 and 1.2 was fitted for the x- and y-axis, respectively.

This OPCPA system is designed for a user facility and demonstrates excellent long-term energy, center frequency and pointing stability measured over 23 hours. Except for the feedback on the center frequency, no further feedback regulation was required for these results. Improvements in short-term energy and pointing stability of the laser can be implemented by using a longer burst (see insert right in Fig. 1), allowing the InnoSlab amplifier more time to reach equilibrium, as well as, by enclosing the laser in a sealed, temperature stable environment.

In conclusion, a 112 W burst mode OPCPA has been developed with good beam quality and reliable long-term stability needed to seed high repetition rate FELs. Sufficient seed laser energy from the OPCPA is expected to cover FEL wavelengths ranging from 26.7 to 42.9 nm at a repetition rate of 100 kHz.

References

[1] H. Höppner, A. Hage, T. Tanikawa, M. Schulz, R. Riedel, U. Teubner, M. J. Prandolini, B. Faatz, and F. Tavella, "An optical parametric chirped-pulse amplifier for seeding high repetition rate free-electron lasers," *Submitted to New J. Phys.* (2015).

* Work supported by HI Jena/DESY. Class 5 Photonics GmbH is currently funded by the Helmholtz Association

† mark.prandolini@desy.de

Thermal properties of borate crystals for high power OPCPA*

R. Riedel† [1,7], *J. Rothhardt* [1,8], *K. Beil* [2], *B. Gronloh* [3], *A. Klenke* [1,8], *H. Höppner* [4], *M. Schulz* [4,7], *U. Teubner* [5], *C. Kränkel* [2], *J. Limpert* [1,8], *A. Tünnermann* [1,8], *M. J. Prandolini* [1,7], *and F. Tavella* [6]

[1]HI-Jena, Jena, Germany; [2]Uni. Hamburg, Hamburg, Germany; [3]Fraunhofer ILT, Aachen, Germany; [4]DESY, Hamburg, Germany; [5]Uni. Oldenburg, Oldenburg, Germany; [6]SLAC, Menlo Park, USA; [7]Class 5 Photonics, Hamburg, Germany; [8]Uni. Jena, Jena, Germany

The potential of borate crystals – BBO, LBO and BiBO – for high average power scaling of optical parametric chirped-pulse amplifiers is investigated. Up-to-date measurements of the absorption coefficients at 515 nm and the thermal conductivities are presented. In addition, the limits to power scaling of OPCPAs are discussed.

Introduction

A major challenge for high power optical parametric chirped-pulse amplification (OPCPA) is thermal effects, caused by the absorption of the pump, signal and idler pulses within the nonlinear crystals at high pump powers. Previous measurements of absorption coefficients of borate crystals were only given as upper limits. In this work, we conduct up-to-date thermal conductivity and absorption measurements. For the linear absorption, we carried out the photothermal common-path interferometry (PCI) method, measured at the Fraunhofer Institute for Laser Technology. In addition, a new method for estimating the linear and nonlinear absorption using thermal imaging at high intensities was developed [1]. Finally, with these new results simulations were conducted to estimate the power scaling limits of OPCPA [1, 2].

Summary of main results

Using the PCI method, absorption values at 515 nm for LBO, BBO and BiBO were about 1–2 orders of magnitude lower than previous literature values (Table 1). These results were confirmed using the thermal imaging method at higher intensities (Fig. 1). This method provides absorption values averaged over the crystal calculated from a finite element analysis. In comparisons to the PCI method which uses low radiation intensities, the thermal imaging method uses much higher laser intensities, and is therefore sensitive to various nonlinear absorption processes at the surfaces and in the bulk. In particular, a large variation in absorption was found for BBO, acquired from different manufacturers. In the case of BiBO, a significant nonlinear absorption coefficient was measured at 515 nm, making this crystal not suitable for high power applications. In addition, for the first time thermal conductivities of BiBO were measured (Table 1).

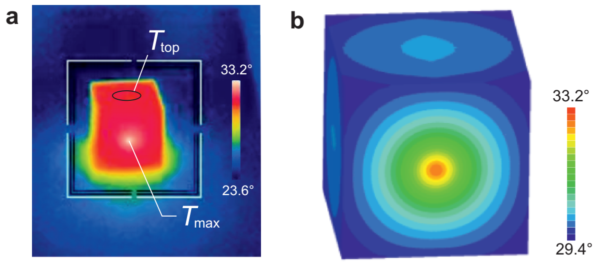

Figure 1: An example absorption measurement using thermal imaging (a) and corresponding simulation with finite element analysis (b): taken from [1].

Simulations including self- and cross-phase modulation were carried out on a proposed ultrabroadband 100 W laser [2]. In this work strategies to achieve good spatial beam quality were discussed. Using the new absorption values, further simulations of high power OPCPA were carried out discussing thermal absorption, including all parasitic signals, and simulating the effects of different heat-sink geometries [1]. Thus based on these simulations it should be possible to operate an OPCPA with an average power of many hundreds of watts.

Table 1: Selected properties of nonlinear crystals: The thermal conductivities at room temperature (κ $\parallel$ to the phase matching (PM) direction) and the average linear absorption coefficient at 515 nm in bulk (α_{515}) and taken from Ref. [1].

	$\kappa \parallel$ to PM [$\mathrm{Wm^{-1}K^{-1}}$]	α_{515} [ppm $\mathrm{cm^{-1}}$]
BBO	0.97 ± 0.07	13, 43, 226†
LBO	3.08 ± 0.03	37 ± 4
BiBO	10.54 ± 0.42	312 ± 150

†Values using crystals from different manufacturers [1].

References

[1] R. Riedel, J. Rothhardt, K. Beil, B. Gronloh, A. Klenke, H. Höppner, M. Schulz, U. Teubner, C. Kränkel, J. Limpert, A. Tünnermann, M. J. Prandolini and F. Tavella, 2014 *Opt. Express* **22** 17607–17619

[2] M. J. Prandolini, R. Riedel, M. Schulz, A. Hage, H. Höppner and F. Tavella, 2014 *Opt. Express* **22** 1594–1607

* Work supported by HI Jena/DESY. Class 5 Photonics GmbH is currently funded by the Helmholtz Association

† robert.riedel@desy.de

Demonstration of a compact, supercontinuum seeded MHz-repetition rate, high power OPCPA*

R. Riedel† [1,4], *M. Schulz* [2,4], *F. Tavella* [3], *and M. J. Prandolini* [1,4]

[1]HI-Jena, Jena, Germany; [2]DESY, Hamburg, Germany; [3]SLAC, Menlo Park, USA; [4]Class 5 Photonics GmbH, Hamburg, Germany

Optical parametric chirped-pulse amplifiers (OPCPA) with high average power are possible with novel high power Yb:YAG amplifiers with kW-level output powers. We demonstrate a compact wavelength-tunable sub-30-fs amplifier with 11.4 W average power with 20.7% pump-to-signal conversion efficiency. The broadband seed is generated via supercontinuum generation in a YAG crystal.

Introduction

For applications requiring wavelength-tunable, high power femtosecond pulses, OPCPA is a most promising technology achieving maintenance-free continuous operation over days. Previously, these systems were quite complex and required a large footprint on an optical table. The first step towards simplifying these complex systems was the use of white light continuum generation (WLG). We have extensively tested this source at these wavelengths for generating OPCPA seed signals [1]. The second important step was the choice of a OPCPA pump system. Here, we used a compact InnoSlab amplifier from AMPHOS GmbH with a flexible repetition rate front-end as seeder, operated at 3.25 MHz repetition rate. The average power used for the experiment was 140 W. Finally, theoretical and experimental tests were conducted to demonstrate the output power scalability of OPCPA up to hundreds of watts of continuous power with femtosecond pulses [2].

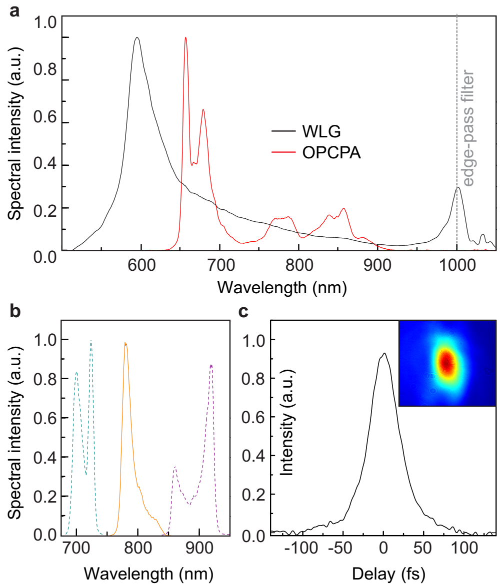

Figure 1: High-power OPCPA [2]: a) Broadband amplified signal (OPA, red) with $\Delta\lambda = 238$ nm at 5% intensity maximum; WLG spectrum (WLG, grey line). b) Selected tunable narrow-band spectra between 700–900 nm, with $\Delta\lambda = 54$ nm bandwidth at 10% intensity maximum. c) Autocorrelation (black line) at 800 nm (orange spectrum in (b)), with a pulse duration of 29.1 fs FWHM. Inset: amplified signal beam profile.

Results

The OPCPA results are shown in Fig. 1. First, the OPCPA was optimized for broadband amplification. The average output power was 11.4 W (pulse energy of 3.5 μJ) with a spectrum supporting a Fourier-limited pulse of 6 fs FWHM (Fig. 1a). Second, a wavelength-tunable option was tested with a central wavelength between 700 and 900 nm (spectra shown in Fig. 1b). As an example, an autocorrelation measurement of a compressed pulse at center wavelength of 800 nm, with pulse duration of 29.1 fs FWHM was demonstrated (Fig. 1c). For more details see [2]. The complete OPCPA setup was demonstrated on a bread board 80×80 cm^2.

Preliminary results, based on new absorption measurements of BBO at the OPCPA pump wavelength of 515 nm, demonstrate the scalability of OPCPA to many hundreds of watts [2]. Therefore, the current power limits for this system are currently set by the availability of suitable pump amplifiers.

In summary, this system avoids a broadband Ti:sapphire seed oscillator and a CPA scheme in the pump amplifier, thus representing a major step toward the availability of compact and stable ultrashort-pulse amplifiers at average powers above 10 W. The intent of this work is to improve the building blocks for a high-power amplifier system and increase the repetition rate for laser experiments that require fast data acquisition.

References

[1] R. Riedel, M. Schulz, M. J. Prandolini, A. Hage, H. Höppner, T. Gottschall, J. Limpert, M. Drescher, and F. Tavella, *Opt. Express* **21** 28987 (2013).

[2] R. Riedel, A. Stephanides, M. J. Prandolini, B. Gronloh, B. Jungbluth, T. Mans and F. Tavella, *Opt. Lett.* **39** 1422–1424 (2014).

* Work supported by HI Jena/DESY. Class 5 Photonics GmbH is currently funded by the Helmholtz Association

† robert.riedel@desy.de

Laser Particle Acceleration

Acceleration of quasi-monoenergetic electron pulses at POLARIS

M. Reuter[1,2], *J. Bohn*[2], *M. Hellwing*[1,2], *M. Hornung*[1,2], *S. Keppler*[1,2], *A. Kessler*[1,2], *D. Klöpfel*[1,2], *O. Kononenko*[3], *H. Liebetrau*[1,2], *Z. Najmudin*[4], *J. Osterhoff*[3], *C.A.J. Palmer*[3], *K. Poder*[4], *W. Ziegler*[1,2], *and M. C. Kaluza*[1,2]

[1]HI Jena, Germany; [2]IOQ Jena, Germany; [3]DESY, Germany; [4]Imperial College London, UK

We present experimental results on laser-driven electron acceleration achieved with the POLARIS laser delivering pulses of 2.4 J in 160-170 fs. Here, we observed the generation of quasi-monoenergetic electron pulses by self-modulated laser wakefield acceleration. We found a clear correlation between the accelerating length and the peak electron energies.

The acceleration of electrons with high-intensity laser pulses is a field of rapidly growing interest. By numerical simulations it was found that the interaction of long pulses ($\geq$ 100 fs) with underdense plasmas can produce electron beams with kinetic energies in excess of 10 GeV. However, for that, high laser energies ($\geq$ 25 J) are required [1, 2].

A high intensity laser focused into a gas creates a plasma with an electron density n_e and excites a plasma wave with the wavelength $\lambda_p \propto \frac{1}{\sqrt{n_e}}$. The plasma wave is resonantly generated if the pulse duration of the laser fits into one half of the plasma wavelength, $\tau_L = \frac{\lambda_p}{2c}$ [3]. If the plasma wave is excited at higher densities or with laser pulses extending over more than one plasma period, the laser pulse is not only compressed and self focused but it splits into a train of pulselets separated by λ_p.

If electrons are injected into the plasma wave, the high longitudinal electric fields $\mathcal{E}_{acc}$ of the wave can generate quasi monoenergetic electron pulses with a kinetic energy of

$$E_{peak} = -e \int_0^{l_{acc}} \mathcal{E}_{acc}(z)\,\mathrm{d}z, \tag{1}$$

where e is the elementary charge and l_{acc} is the length over which the electrons were accelerated. After covering the maximal acceleration length given by $l_{acc,max} = \lambda_p n_c/n_e$ the electrons run into the decelerating phase of the plasma wave, where n_c is the critical density of the laser.

The experiment was carried out using the fourth amplifier stage of the POLARIS laser in Jena delivering 2.4 J in 160-170 fs. The pulses were focused by an f/14 off axis parabolic mirror to peak intensities of $1.8 \times 10^{18}\,\mathrm{W/cm^2}$. A gas cell of variable length was used as a target. Raman-shifted satellites – indicative of longitudinal pulse break up – were observed in the spectrum of the transmitted laser radiation and could be used to determine the plasma density. The energy of the accelerated electrons was measured in a magnetic spectrometer.

In this experiment we observed the generation of quasi-monoenergetic electron pulses. In addition to the small energy spread (as small as $\frac{\Delta E}{E} = 4\%$) these electron pulses exhibit hardly any background current (Fig. 1). Using Eq. (1) and the target length l_T as the effective acceleration length we were able to reproduce the experimental results assuming a linear $\mathcal{E}$-field distribution inside the plasma

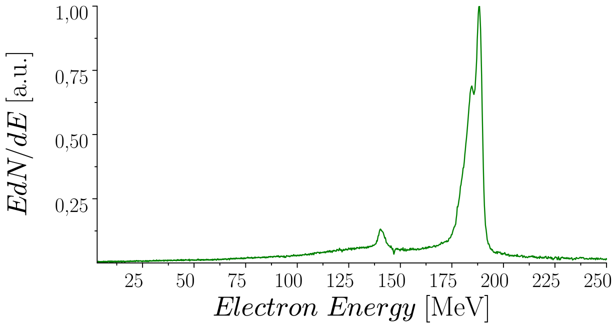

Figure 1: Quasi-monoenergetic electron pulse.

wave leading to a parabolic dependence of the electron energy as a function of the acceleration length (Fig. 2). Note that the interaction length is not confined to the gas cell due to out-streaming gas. The acceleration process can be di-

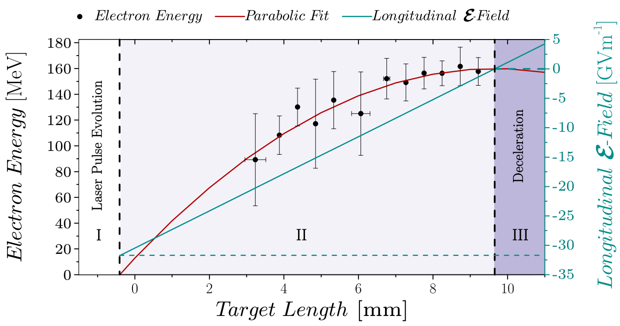

Figure 2: Correlation of the electron energies to the accelerating field and the acceleration length.

vided into three steps. First, the laser intensity increases most likely in the region of out-streaming gas in front of the gas cell. (I in Fig. 2). When the laser intensity is sufficiently high wavebreaking occurs. The estimated wavebreaking field is $\mathcal{E} \approx 31\,\frac{\mathrm{GV}}{\mathrm{m}}$ (dashed blue line in Fig. 2). Afterwards, the electron energy grows with the acceleration length in the linearly decreasing $\mathcal{E}$-field amplitude (II in Fig. 2). Once the electron pulse approaches the decelerating electric field ($\mathcal{E} > 0$) of the plasma wave, the electron energy reaches its maximum achievable value. For longer target lengths the electrons would experience a positive electric field and deceleration is expected (III in Fig 2).

References

[1] W. Lu et al., PRST AB 10, 061301 (2007)

[2] X Wang et al., Nature Communications 4, 1988 (2013)

[3] T. Tajima and J.M. Dawson, PRL 43, 4 (1979)

Experiment on guiding laser-accelerated electrons towards a transverse-gradient undulator using electron optics*

M. Leier[1], *C. Widmann*[2], *A. Bernhard*[†2], *W. Werner*[2], *A. Sävert*[1,3], *M. Schwab*[1], *S. Kuschel*[3], *and M.C. Kaluza*[1,3]

[1]IOQ, Jena, Germany; [2]KIT, Karlsruhe, Germany; [3]HIJ, Jena, Germany

At the JETI-40 laser system an experiment was performed to test an electromagnetic chicane for the transport of laser-accelerated electrons from the plasma source to a superconducting transverse-gradient undulator (SCTGU).

Experimental setup

A SCTGU has a transverse gradient in the magnetic field strength, so that a transversely chirped electron beam with a broad energy distribution can produce narrow-band undulator radiation [1]. The electrons, accelerated in a gas cell with the JETI-40 laser, were sent through a chicane of six quadrupole and two dipole magnets. Figure 1 shows a schematic sketch of the chicane. The quadrupoles Q were in-house-developed electromagnets and used to collimate and shape the electron pulses. The electromagnetic dipoles D were used to deflect the electron pulses downwards and disperse them in the deflection plane. By changing the current in the magnets the focusing and deflecting power of the quadrupoles and dipoles, respectively, could be adjusted.

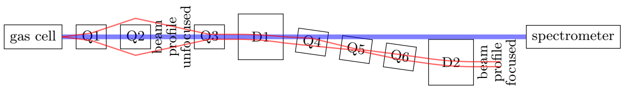

Figure 1: Schematic sketch of the chicane (side view), blue is the undisturbed electron beam direction and red is the schematic electron beam envelope with all magnets.

Beam profile and shaping of the beam

The freely propagating electron beam profile was measured behind the second quadrupole Q2. In figure 2a the averaged beam profile with the magnets turned off is shown. The divergence of the averaged electron beam is 10 mrad (FWHM).

The finite transverse acceptance of the SCTGU requires a chromaticity-corrected focusing of the beam down to the sub-mm range. As a first step in this experiment a linear, i.e. not chromaticity corrected beam optic was realized, providing the correct focusing only for a narrow band out of the beam energy spectrum. Figure 2b shows the result when the first three quadrupoles were used. The beam is focused to less than 3 mm in horizontal direction and less than 6 mm in vertical direction at a distance of 2.9 m behind the target. When all six quadrupoles were used, the focus was less than 3 mm in both directions (figure 2c). This is

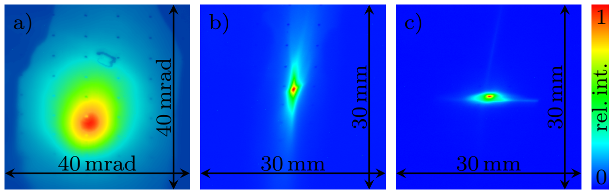

Figure 2: In a) the averaged electron beam profile with a divergence of 10 mrad is shown. b) and c) show the focused, averaged electron beam with one and two quadrupole-triplets, respectively.

showing, that the quadrupoles are able to collect the beam and transport and focus a relatively broad energy range. The size of the focus is still determined by the chromatic aberrations of quadrupoles and a slightly out-of-focus scintillating screen. To focus the whole energy range required for the SCTGU to the desired size a chromaticity-corrected chicane will be needed in the next step of the experiment.

Spectrum of the electrons

The first three quadrupoles were used to focus the beam into the spectrometer at a distance of more than 3 m to the electron source. The dipoles were turned off for these measurements, since they deflect the electron beam away from the original axis, to which the electron spectrometer was aligned. Usually, only a very weak electron signal is detectable with the spectrometer, since the electron beam divergence is too large to get a signal which is sufficiently strong. The quadrupoles act as energy filters and, therefore, only a certain energy could be focused into the spectrometer. Figure 3 shows three averaged spectra peaked at different energies, since the quadrupoles were driven with different currents to guide a certain energy through the chicane.

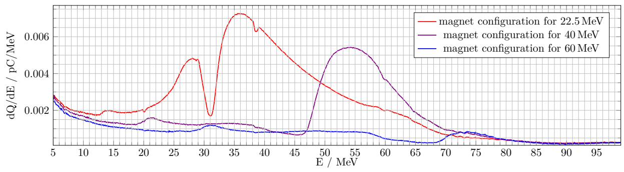

Figure 3: Averaged spectra of the electrons for different settings for the magnets

References

[1] G. Fuchert et al., “A novel undulator concept for electron beams with a large energy spread”, NIM A 672, 33-37 (2012)

* Work supported by BMBF (contract 05K10SJ2 and 05K10VK2)
† axel.bernhard@kit.edu

Diagnosing Laser Wakefield Accelerators with Few-Cycle Pulses

D. Ullmann[1], M. B. Schwab[2], S. Kuschel[1,2], M. Yeung[1,2], A. Sävert[1,2], M. Zepf[1,2,3], and M. C. Kaluza[1,2]

[1]Helmholtz-Institute Jena, Germany; [2]Institute of Optics and Quantum Electronics Jena, Germany; [3]Department of Physics and Astronomy - Queens University Belfast, UK

Experimental setup

The $40\ TW$ JETI laser system at the Institute of Optics and Quantum Electronics and at the Helmholtz-Institute Jena is capable of producing ultra short electron bunches generated during the interaction of the intense laser radiation with an underdense gas target. Focussing the laser beam with a f/13 off axis parabolic mirror to a spot diameter of $14\mu m$ (FWHM), a peak intensity of $4 \cdot 10^{18} W/cm^2$ was achieved, successfully accelerating electrons to peak energies of $\approx 200\ MeV$.

New designed gas cell

For optimum electron acceleration at the JETI-40 laser system, a gas cell used as a target was specially designed (Fig. 1). In this cell, the gas distribution seen by the laser pulse is more homogeneous than in conventional super sonic jets. Thereby the next step has been taken to converge experimental conditions and theoretical assumptions. Cylinders with conical entrance holes forming the entrance and exit of the target can be adjusted, changing the effective interaction length of the pulse with the gas. A mixture of helium and nitrogen (95:5) was used.

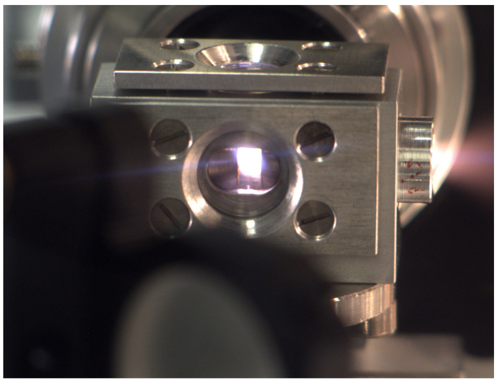

Figure 1: New gas cell for investigation of plasma driven electron acceleration. A window for transverse probing is in the center and the main pulse can propagate through cylinder endings.

By applying different background pressures to the cell, the signal of the generated electrons was optimized, resulting in good shot-to-shot stability and well collimated electron beams with better pointing properties than when compared to conventional gas jets. Using the few-cycle probe beam [1], shadowgraphic and density diagnostics were implemented. The latter method was realized with a wavefront sensor, which was a new appoach for interferometric density measurement in our group. With a commercial device (Phasics SID 4 visible), the laser plasma interaction induced phase change could be reconstructed on-the-fly during the experiment using the included software.

Results and Outlook

A typical density reconstruction from the wavefront measurements is depicted in Fig. 2, showing the arrival of the main-pulse propagating from left to right, located around the most intense area. To obtain the radial density distribution a symmetric Abel inversion was performed, leading to maximum densities in the range of 1.30 to $1.35 \cdot 10^{19}\ cm^{-3}$, which can be translated to a plasma wavelength of $\lambda_{pw} = 9.1 \pm 0.2\ \mu m$, assuming that the main-pulse is traveling with approximately the speed of light. This is in good agreement with shadowgraphic direct measurements of the plasma wave length. In an upcoming experiment it is planned to simultaneously record the electron density profile via wave front measurement and the shadowgram to pinpoint the exact position of the plasma wave in the electron density distribution.

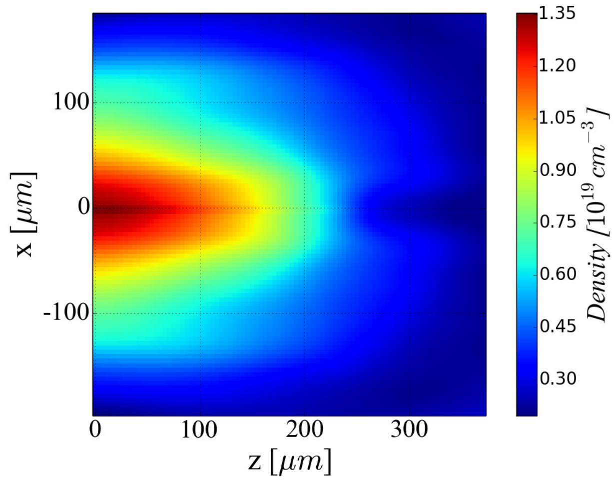

Figure 2: Plasma density distribution reconstructed from Abel inverted phase distribution showing the arrival of the main-pulse.

References

[1] M. B. Schwab et al., "Few-cycle optical probe-pulse for investigation of relativistic laser-plasma interactions", Appl. Phys. Lett. 103, 191118 (2013)

Demonstration of plasma lensing of a laser wakefield accelerated electron bunch

S. Kuschel[1,2]*, T. Heinemann*[3]*, O. Karger*[3]*, M. Schwab*[1]*, D. Ullmann*[1]*, A. Knetsch*[3]*, D. Hollatz*[1]*, M. Yeung*[2]*, M. Leier*[2]*, A. Sävert*[2]*, M. C. Kaluza*[2]*, B. Hidding*[3,4,5]*, and M. Zepf*[1,2]

[1]Institute for Optics and Quantumelectronics, University of Jena, Max-Wien-Platz 1, 07743 Jena, Germany; [2]Helmholtz Institute Jena, Fröbelstieg 3, 07743 Jena, Germany; [3]Institute for Experimental Physics, University of Hamburg, Luruper Chaussee 149, 22761 Hamburg, Germany; [4]SUPA, Department of Physics, University of Strathclyde, G4 0NG Glasgow, UK; [5]Particle Beam Physics Laboratory, UCLA, USA

We report on the first all-optical demonstration of plasma lensing using laser wakefield accelerated electrons in a two-stage setup. The LWFA electron bunch was focused by a second plasma stage without any external fields applied.

Plasma wakefields can provide electrical fields in the order of hundreds of GV/m und thus allow to build compact particle accelerators. However, transportation, shaping and focusing of accelerated particle beams still requires conventional structures which will be much larger than the accelerator itself. As a plasma is used for the acceleration process, it has been shown, that a plasma can be used for focusing the particle bunch as well due to transversal fields inside the plasma wave[1, 2].

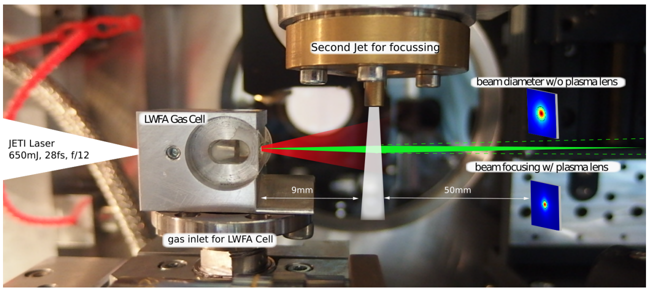

Figure 1: Illustrated photo of experimental setup: the laser pulse, incident from the left, drives an LWFA stage in a mixed-species gas cell, and the generated electron beam expands in vacuum according to its obtained divergence. If the second gas jet is turned on, the remnant and diverged laser pulse preionizes the H_2 gas and the trailing electron beam experiences plasma lensing, which reduces the divergence substantially as observed on a Lanex (Fig 2).

The experiment presented here was conducted at the 40 TW "JETI" Ti:sapphire laser system at the University of Jena, delivering $\tau = 28$ fs pulses at a central wavelength $\lambda_0 = 800$ nm with $E = 650$ mJ on target. The laser pulses were focused by an f/12 off-axis parabolic mirror to a spot size $\pi w_0^2 \approx 120\,\mu m^2$ (FWHM), resulting in a vacuum peak normalized amplitude of $a_0 \approx 2.2$. The laser focus was aligned to the entrance aperture of a $z_C = 2.5$ mm long gas cell (acceleration stage) as seen in figure 1. The gas in the gas cell was composed of a 95% He, 5% N_2 mixture in order to make use of higher-level laser ionization injection [3, 4]. The LWFA stage produced electron bunches up to $E_{\max} = 130$ MeV with a large energy energy spread and a total charge of up to 10 pC.

As soon as the focusing stage is turned on, the solid angle covered by the electron beam on the Lanex scintillator screen reduces from 16 mrad^2 to 6 mrad^2 (figure 2) while the total charge of the bunch decreases to 75% of its inital value only (not shown). Thus not only a decrease of the electron divergence but also an increase in electron intensity on the Lanex (a net focusing effect) was measured.

The measured focusing matches the results from particle-in-cell simulations with the EPOCH Code (not shown here).

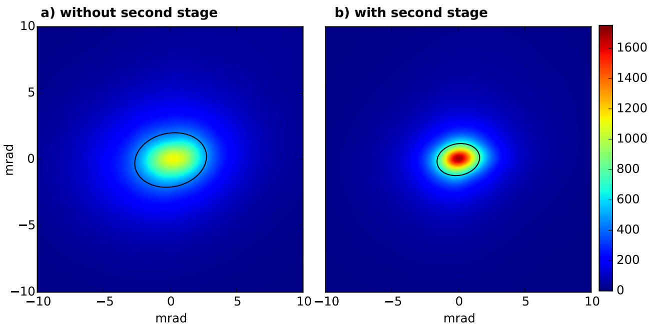

Figure 2: Averaged and center aligned (pointing corrected) beam profile as seen on the Lanex: a) 227 reference shots with the acceleration stage only. b) 175 shots with the second lensing stage. In both pictures the ellipse encloses the standard deviation of a best fit 2D gaussian function to the beam profile. The ellipse reduces its area from 16 mrad^2 (left) to 6 mrad^2 (right) when the focusing stage is turned on.

References

[1] G. Hairapetian, P. Davis, C. E. Clayton, C. Joshi, S. C. Hartman, C. Pellegrini, and T. Katsouleas, Phys. Rev. Lett. 72, 2403 (1994).

[2] R. Govil, W. P. Leemans, E. Y. Backhaus, and J. S. Wurtele, Phys. Rev. Lett. 83, 3202 (1999).

[3] M. Chen, Z.-M. Sheng, Y.-Y. Ma, and J. Zhang, Journal of Applied Physics 99, 056109 (2006).

[4] A. Pak, K. A. Marsh, S. F. Martins, W. Lu, W. B. Mori, and C. Joshi, Phys. Rev. Lett. 104, 025003 (2010).

Smith-Purcell radiation generation by a proton beam from a laser-driven ion accelerator

A. H. Woldegeorgis[1,2]*, S. Herzer*[1]*, P. Singh*[1]*, G. G. Paulus*[1,2]*, T. May*[3]*, and A. Gopal*[*1,2]

[1]Institut für Optik und Quantenelektronik, Jena, Germany; [2]Helmholtz-Institut Jena, Jena, Germany; [3]Leibniz-Institut für Photonische Technologien, Jena,Germany

We report the first experimental observation of secondary T-ray (terahertz radiation) generation by MeV proton beam from a laser-driven ion accelerator by Smith-Purcell (SP) effect. Sub μJ T-rays were recorded using a pyroelectric detector. Simultaneous measurement of the ion spectra allowed us to estimate power of the emitted radiation and compare it with the experimental results.

Charged particles passing close to a periodic structure can emit radiation by Smith-Purcell effect [1]. The wavelength of the emitted radiation is given by the formula $\lambda_{\rm n} = \frac{\rm D_g}{|\rm n|}(1/\beta - \cos\theta)$, with n the diffraction order, $\rm D_g$ the grating period, β the relativistic velocity of the particle and θ the angle of observation. Besides being a tunable radiation source, the SP radiation from protons can be employed to characterize the longitudinal (time) profile of the proton bunch itself [2, 3]. The goal of our proof-of-principle experiment was the demonstration of SP radiation using proton beams.

A proof-of-principle experiment was carried out at the JETI40 laser system at the Institute of Optics and Quantum Electronics. The multi-terawatt laser pulses were focused to 5 μm thick Titanium foil targets to generate intensities above 10^{19} $\rm W/cm^2$. The ion spectra measured with a Thomson parabola detector recorded maximum proton energies of 2.3 MeV. Periodic grating structures (79 lines/mm) were placed parallel to the target normal direction in a remote controlled carousel. An aperture was used to select only the high energy particles. Smith Purcell radiation was collected and sent to a pyroelectric detector placed outside the experimental vacuum chamber through a Silicon window.

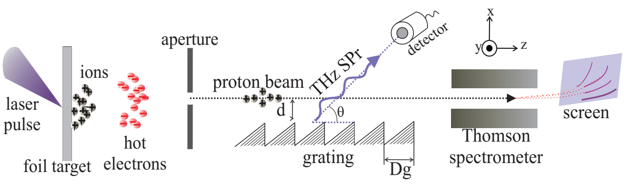

Figure 1: Schematic overview of the experimental setup.

Simultaneous recording of the proton spectra and the Smith Purcell radiation allowed us to compare the strength of the recorded radiation with the expected value calculated using the corresponding particle spectra and grating parameters. Our estimate shows that sub-microJoule T-ray pulses are generated. Besides, the distance d between the particle beam and the grating structure was varied to optimize the generation process. Measurements reveal that the emission is peaked when the distance between the particle beam and the grating structure is on the order of the interaction length (h_{int}).

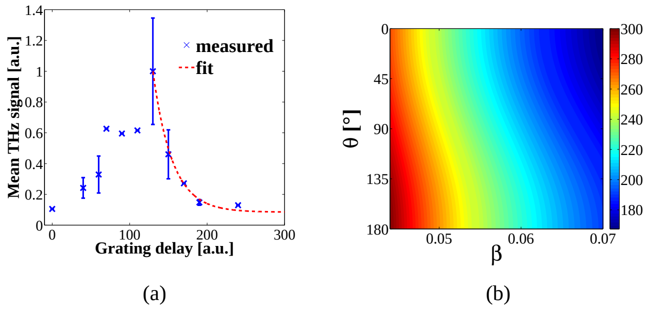

Figure 2: (*Left*) plot of peak THz signal, averaged over multiple shots, as a function of the grating delay (the error bars show the shot-to-shot fluctuation) and the exponential fit function (red-dashed line); (*right*) calculated wavelength (in μm) of the SP radiation from the observation angle θ for different proton energies.

The THz signal decays exponentially as d is increased from the optimum distance. On the other hand, when $d < h_{int}$ the beam interacts physically with the grating. Therefore, the signals detected (shown in Figure 2a, to the left of the peak) could be a transition radiation from such kind of interaction.

Future studies will focus on the generation of coherent radiation and its use as an online non invasive diagnostic for proton bunch duration. In addition grating and target parameters will be varied to generate even more powerful T-rays by Smith-Purcell effect.

References

[1] S.J. Smith and E.M. Purcell, Phys. Rev. **92**, 1069 (1953)

[2] M. C. Lampel, Nucl. Instr. and Meth. A **385**, 19 (1997); D. C. Nguyen, Nucl. Instr. and Meth. A **393**, 514 (1997)

[3] G. Doucas *et al.*, Phys. Rev. ST Accel. Beams **5**, 072802 (2001)

* amrutha.gopal@uni-jena.de

Laser proton acceleration from solid hydrogen targets

Jens Polz[1], Georg A. Becker[1], Rui Alexandre Costa Fraga[3], Robert Grisenti[3], Marco Hellwing[1], Marco Hornung[1, 4], Anton Kalinin[3], Sebastian Keppler[1], Diethard Klöpfel[1], Hartmut Liebetrau[1], Alex P.L. Robinson[2], Frank Schorcht[1, 4], and Malte C. Kaluza[1, 4]

[1]Institut für Optik und Quantenelektronik, Friedrich-Schiller-Universität, D-07743 Jena, Germany
[2]Central Laser Facility, Rutherford-Appleton Laboratory, Chilton, Oxon., OX11 0QX, UK
[3]Institut für Kernphysik, Goethe-Universität, D-60438 Frankfurt, Germany
[4]Helmholtz-Institut Jena, D-07743 Jena, Germany

Introduction

Laser-driven proton acceleration in the TNSA regime has been a topic of extensive research since its discovery in 2000 [1]. Usually these experiments are performed with metal foils as a target, which are coated with hydrocarbon contaminations. However, this approach has a few drawbacks, such as the production of debris and the unwanted energy transfer to secondary ion species. To avoid these disadvantages a target of pure solid hydrogen would be favourable. Here, we report on an experiment where we used solid hydrogen filaments as a target for laser ion acceleration in the TNSA regime.

Experimental Setup

The experiment was performed at the POLARIS laser facility, which delivered pulses of 2.5 J energy and 217 fs duration. They were focused by an f/2.5 off-axis parabolic mirror to a FWHM focal spot size of 8.4 μm^2. 25.9% of the laser energy were encircled in this area resulting in an intensity of 3.5×10^{19} W/cm^2.

The cryogenic source [2] generating the hydrogen filament was operated at temperatures between 14 and 19 K. The liquefied hydrogen was forced through a nozzle with diameter of 10 µm at pressures of 10 to 30 bar. When injected into vacuum the hydrogen further cooled down due to evaporation, leading to solidification before the liquid stream could break up into droplets, hence forming a filament of solid hydrogen with the same diameter as the nozzle. Since the hydrogen was fed at a rate of 345 to 620 ml_n/min into the vacuum chamber, it had to be removed by a differentially pumped target catcher in order to maintain the pressure inside the target chamber at a reasonable level.

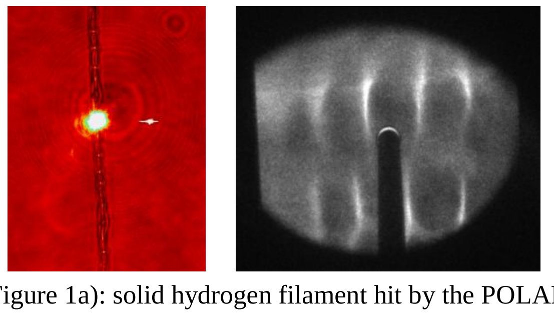

Figure 1a): solid hydrogen filament hit by the POLARIS laser 1 b): recorded scintillator screen image providing a rendition of the ion beam profile (right)

The filament was aligned with respect to the laser focal spot using an optical probe beam. The protons accelerated by the laser, which was incident under 0° on the filament, propagated towards a fast responding scintillator, which was imaged onto a gateable CCD. Due to the time-of-flight of the accelerated protons, the gateable CCD could record energy-resolved images of the proton beam profile. The part of the proton pulse propagating in laser forward direction could pass through a hole in the scintillator towards a Thomson parabola spectrometer. Here, the full energy spectrum of the central part of the proton beam was recorded.

Experimental Results

An exemplary image of the recorded proton beam profile is shown in figure 1 b). It shows a sub-structure aligned parallel to the filament. This structure was present in all shots. It was also observed on CR39 detectors positioned in the beam on few shots.

Several proton spectra obtained during the experiment are shown in figure 2. While the low energy part of the spectra shows a typical exponential decay, as expected from TNSA, the high energy part exhibits a clear non-thermal behaviour.

While previous theoretical investigations [3] predicted that the formation of non-thermal structures in the proton spectra is due to the presence of a secondary heavier ion species and a spatially confined proton source, this explanation cannot be used here. Theoretical investigations to explain this behaviour are currently under way.

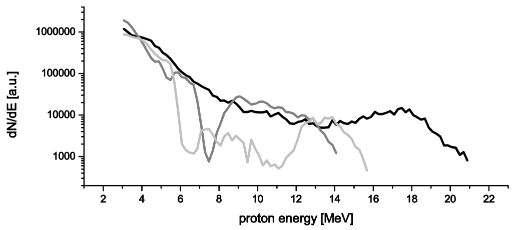

References

[1] R. A. Snavely *et al.* Phys. Rev. Lett. **85**, 2945 (2000)
[2] R. A. C. Fraga *et al.* Review of Scientic Instruments **83**, 025102 (2012).
[3] A. P. L. Robinson *et al.* Plasma Physics and Controlled Fusion **51**, 024001 (2009)

Laser-Driven Proton Acceleration at POLARIS with SHG and nm thin foils*

G. A. Becker[1], J. Reislöhner[1], M. Hornung[2], A. Seidel[2], J. Bin[3,4], L. Bock[1], F. Brack[5], M. Hellwing[1], P. Hilz[3,4], S. Keppler[1], A. Kessler[2], S. Kraft[5], S. Kuschel[2], H. Liebetrau[1], J. Polz[1], H-P. Schlenvoigt[5], F. Schorcht[2], H. Wang[2], K. Zeil[5], U. Schramm[5], M. Zepf[1,2,6], J. Schreiber[3,4], and M. C. Kaluza[1,2]

[1]Institut für Optik und Quantenelektronik, Friedrich-Schiller-Universität Jena, Germany; [2]Helmholtz-Institut Jena, Germany; [3]Fakultät für Physik, Ludwig-Maximilians-Universität München, Germany; [4]Max-Planck-Institut für Quantenoptik, München, Germany; [5]Institut für Strahlenphysik, Helmholtz-Zentrum Dresden-Rossendorf, Germany; [6]School of Mathematics and Physics, Queens University Belfast, UK

In most experiments on laser-proton acceleration *Target Normal Sheath Acceleration* (TNSA) is the dominant acceleration mechanism. A disadvantage is the scaling of the achievable proton energy as $E_p \propto \sqrt{I_L}$, where I_L is the laser pulse intensity [1]. One mechanism which is predicted to scale as $E_p \propto I_L$ is *Radiation Pressure Acceleration* (RPA) in the *(leaky) light sail* (LS) regime [2]. Here, the laser is focused under normal incidence on a foil. Electrons on the front side of the target are pushed via the ponderomotive force inwards and form a charge separation layer with the inert ions until the electrostatic and the light pressure balance each other. This leads to the condition [3]

$$a_0 \approx \sigma = \frac{n_e d}{n_c \lambda}\ , \tag{1}$$

with the amplitude of the normalized vector potential $a_0 = \sqrt{I_L \lambda^2 / 1.37 \cdot 10^{18}\ \mathrm{W/cm^2 \mu m^2}}$, the normalized areal density σ, the electron density n_e and the critical density n_c. The optimal target thickness, for *diamond-like carbon* (DLC) which corresponds to $n_e \approx 180 n_c$ ($\lambda = 515$ nm, $a_0 \approx 4$) is about $d \approx 11$ nm which means that the laser must have a very high temporal intensity contrast so that the laser pulse interacts with a mainly intact solid foil target, which has not been destroyed by the prepulse.

An experiment was performed at the POLARIS laser. To achieve the required temporal intensity contrast a KDP crystal was installed in the target chamber to generate the second harmonic at $\lambda = 515$ nm with an pulse energy of $E \approx 3$ J. By focussing with an f/2.5 off-axis parabola, under normal incidence on target, we achieved an average intensity of about $I_L \approx 8 \cdot 10^{19}\ \mathrm{W/cm^2}$ which corresponds to $a_0 \approx 4$. To change the laser polarization a $\lambda/4$ plate was placed in the target chamber. As the ion diagnostics we used a *Thomson parabola* (TP) equipped with a MCP-detector to detect ions in target normal direction inside a solid angle of $\Omega = 0{,}4$ µsr, as well as a square plastic scintillator with two gateable CCD-cameras to measure the energy-resolved proton beam profile.

Besides DLC foils with $d \approx 5$ nm up to $d \approx 40$ nm also plastic foils (CH, $n_e \approx 90 n_c$) with $d \approx 20$ nm up to $d \approx 800$ nm were used as targets. For each target thickness and material at least 20 shots were typically taken. The averaged proton temperature T_p was taken from the five best shots, reducing the influence of shot-to-shot fluctuations. The square plastic scintillator surrounding the entrance of the TP allowed us to confirm whether the maximum of the ion beam profile was on or near the TP entrance or not. For example the ion beam divergence for $d \approx 10$ nm DLC is about 7° while the main direction between two shots fluctuates up to 15°.

The results are plotted in figure 1. In both figures, a maximum occurs at $\sigma \approx 5$ with $T_p \approx 1{,}65$ MeV which agrees with $a_0 \approx 4$ (eq. 1). However, theory predicts that circular polarization should work better for LS [2, 3]. However, in another experiment [4] the contrary was measured where linear polarization was better for $a_0 \approx \sigma$.

In Figure 1a.) the proton temperature steadily falls for higher σ in contrast to b.). In the latter case we observe a second maximum at $\sigma \approx 30$. Here, we expect TNSA to be the dominant proton acceleration mechanism favored due to jxB-heating, which only occurs for linear polarization and enhances the hot-electron production.

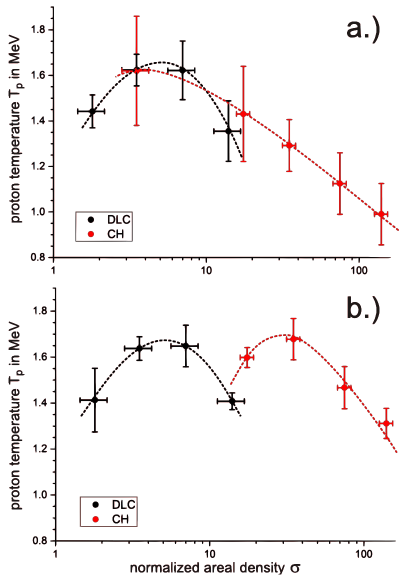

Figure 1: T_p vs. σ for DLC foils (black) and CH foils (red). a.) shows the results obtained with circular laser polarization and b.) with linear polarization.

* Work is part of the SFB TR18 and onCOOPtics

References

[1] Wilks et al., Phys. Plasmas 8, 542 (2001).
[2] Qiao et al., Phys. Rev. Lett. 105, 155002 (2010).
[3] Yan et al., Phys. Rev. Lett. 100, 135003 (2008).
[4] Henig et al., Phys. Rev. Lett. 103, 245003 (2009).

Shaping high-current proton bunches in the picoseconds range from a laser-driven source*

S. Busold[1,2], *D. Schumacher*[1], *C. Brabetz*[1], *D. Jahn*[3], *F. Kroll*[4], *O. Deppert*[3], *A. Blazevic*[1,2], *V. Bagnoud*[1,2], *and M. Roth*[3]

[1]GSI Helmholtzzentrum für Schwerionenforschung GmbH, Darmstadt, Germany; [2]Helmholtz Institut Jena, Germany; [3]TU Darmstadt, IKP, Germany; [4]Helmholtz-Zentrum Dresden - Rossendorf, Germany

LIGHT beamline at GSI.
The German national collaboration "LIGHT" (Laser Ion Generation, Handling and Transport, [1]) has implemented a worldwide unique laser-driven proton beamline at GSI. The compact acceleration up to nearly 30 MeV proton energies is driven by the PHELIX laser via the TNSA mechanism and a pulsed high-field solenoid provides for beam collimation and energy selection [2].
A radiofrequancy (rf) cavity is implemented in the beamline at 2 m distance to the source for phase rotation of the created single bunch, which shows a typical energy spread of around 20% (FWHM around central energy) and high particle numbers of up to 10^9. Energy compression of the bunch below 3% was demonstrated in an experimental run in 2013 [3].
For the 2014 campaign, the beamline has been extended by a diagnostic chamber at 6 m distance to the source, two quadrupole doublets for beam transport and a third doublet for final focusing of the bunch. The additional space behind the cavity, which is again used at -90 deg synchronous phase but this time at higher rf power to 'over-focus' the bunch in longitudinal phase space, is necessary as drift space for phase focusing experiments.

Results on temporal compression via phase focusing.
Proton bunches with a central energy of 7.8 MeV were selected from the source and propagated through the beamline, containing typically particle numbers in the range of 2×10^8 to 5×10^8 within FWHM. The temporal bunch profile measurement was done by two independent and parallel working diagnostics: on the one hand the emitted radiation of a fast plastic scintillator (BC422Q with 1% benzene quenching from Saint Gobain), temporally resolved by a streak camera; and on the other hand a specially developed diamond detector (constructed by GSI's detector laboratory).
Both detectors yield consistent results, with the accuracy of the streak suffering from the still large decay time of the scintillator of 700 ps and thus only setting an upper limit of the bunch length. Figure 1 shows the signal of both detection systems for the shortest measured bunch with a FWHM bunch length of τ=(462±40) ps. This minimum is obtained by injection at a synchronous phase of Φ_s=-90 deg into the rf field and scanning the rf power (indicated by the normalized rf amplitude $U_{rf,n}$) for the optimum working parmeters (see figure 2).

* This work is supported by the Helmholtz Institute Jena.

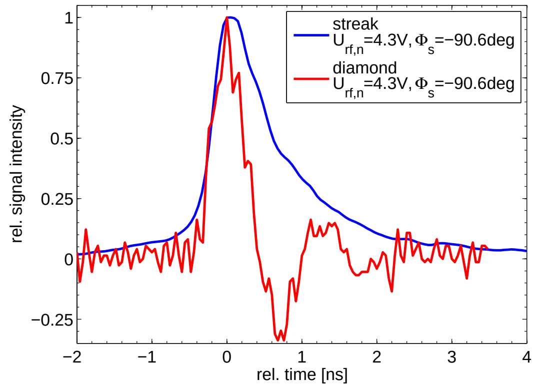

Figure 1: Measurement of the temporal profile of the proton bunch. While the scintillator of the streak camera image suffers from a slow decay time, the diamond detector provides for a high temporal resolution.

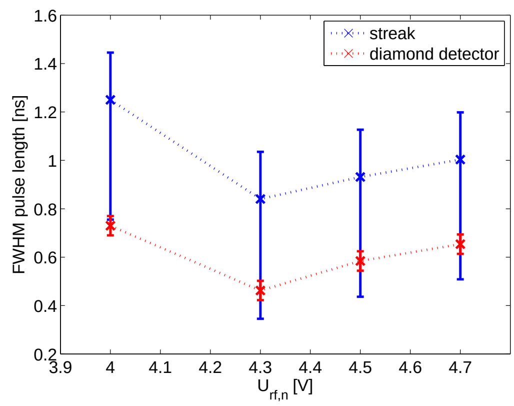

Figure 2: Scan of the applied rf power $U_{rf,n}$ at Φ_s=-90 deg synchronous phase to achieve the shortest bunch length. The streak data represents the upper limit and the diamond detector provides a high-precision measurement.

References

[1] S. Busold *et al.*, NIMA **740**, 94-98 (2014)
[2] S. Busold *et al.*, PRSTAB **16**, 101302 (2013)
[3] S. Busold *et al.*, PRSTAB **17**, 031302 (2014)

High-energy monoenergetic proton beams from two stage acceleration with a slow laser pulse

H.Y.Wang[1], *X. Q. Yan*[2], *and M.Zepf*[*1]

[1]Helmholtz Institute Jena, Fröbelstieg 3, 07743 Jena, Germany; [2]State Key Laboratory of Nuclear Physics and Technology, Peking University, Beijing 100871, China

We present a new regime to generate high-energy monoenergetic proton beams which takes place when the laser pulse is slowed down (laser group velocity $v_g < c$) by an extended near-critical density plasma. In this regime, ions initially accelerated by the light sail (LS) can be further trapped and reflected by the relatively slow propagating laser snowplow potential. These two acceleration stages are connected by the onset of Rayleigh-Taylor-like (RT) instability. It is shown by two-dimensional particle-in-cell simulation that quasi-monoenergetic proton beams with energy up to 300 MeV can be generated at laser intensities of $\sim 2.5 \times 10^{21} W/cm^2$.

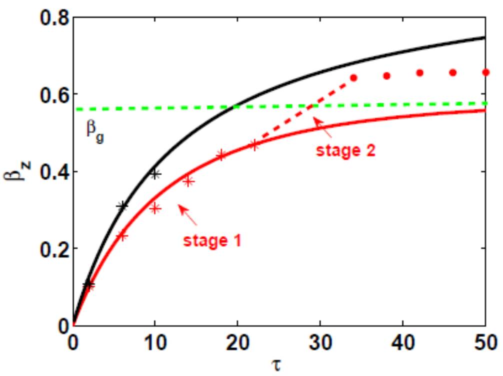

Figure 1: (color online). The peak velocities β_z of ion beams varying with the acceleration time τ the cases, respectively, of theory prediction ($\beta_g = 1$)(black line), theory prediction ($\beta_g = 0.58$) (red line), simulation results for single solid layer target ($\beta_g = 1$, black stars), and simulation for two layer target ($\beta_g = 0.58$, red stars and red dots are denoted to the proton peak velocity observed in the first stage and after the second stage, respectively.)

The light sail scheme has drawn much interest due to the possibility to reach very high ion energies with foreseeable laser and target technology [1,2]. However, the typical LS stage maintains only for a limited time due to the development of Rayleigh-Taylor-like instability (RTI). The characteristic time for RTI is:

$$\tau_{RT} = \tau_0/\beta_g, \tag{1}$$

where τ_0 is the characteristic time for RTI at $\beta_g = 1$ for standard LS regime. Thus the smaller the β_g, the longer LS acceleration one may expect. It is shown in Fig. 1 that the increase of ion peak velocities in the LS stage follow well with the theory prediction. A about 2 times longer LS acceleration is observed from the two layer target.

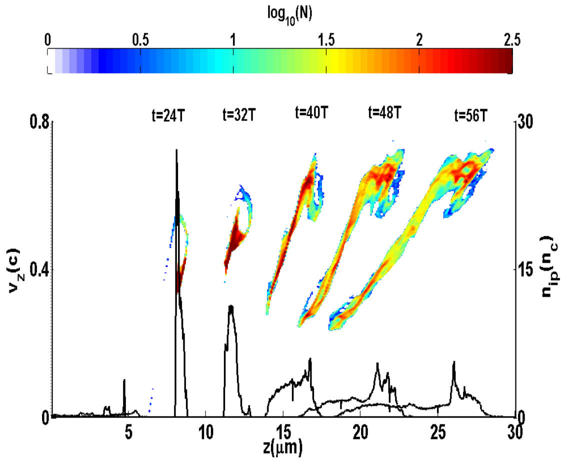

Figure 2: (color online). Time evolution for the proton phase space distributions and the corresponding proton density distributions. The color bar represents the proton numbers in log scale.

More interestingly for the two layer target, a second stage acceleration is connected with the first LS stage after the development of RTI, which is related to reflection of the LS ions by the slow propagating snowplough potential formed in the near-critical density plasma. These two stage acceleration process can be clearly seen from the proton phase space evolution shown in Fig. 2. At early stages, The protons show a clear "spiral structure", which is a typical feature for the LS ion acceleration. This "spiral structure" disappear at $t = 40T$ and the proton beam debunches in the longitudinal direction, implying the termination of the LS stage by the development of RTI. At later time, some fast LS ions are trapped and reflected by the laser snowplow potential, forming a pronounced density peak there(see $t = 56T$), this conrresponds to a quasimonoenergetic proton beam with the peak energy $\sim 300MeV$, density $5n_c$ and the divergence $< 10°$.

References

[1] X. Q. Yan et al., Phys. Rev. Lett. 100, 135003 (2008).

[2] B. Qiao, M. Zepf, M. Borghesi, and M. Geissler, Phys. Rev. Lett. 102, 145002 (2009).

* m.zepf@uni-jena.de

Impact of cold target electrons on laser-driven ion acceleration from foils with rear-surface density gradients

T. Kiefer[1], *T. Schlegel*[1,2], *and M. C. Kaluza*[1,3]

[1]Helmholtz-Institut Jena, Jena, Germany; [2]GSI Helmholtzzentrum für Schwerionenforschung GmbH, Darmstadt, Germany; [3]Friedrich-Schiller University, Jena, Germany

In the literature different theoretical models are used for the interpretation of ion acceleration experiments in the Target Normal Sheath Acceleration (TNSA) regime. Commonly, these models use a one-dimensional electrostatic description where the Poisson equation plays a central role. In the TNSA process, the laser-heated, hot electrons generate exclusively the quasi-electrostatic field which drives the ion acceleration. As a consequence, in most models, one only considers the hot electrons (1T-model) while ignoring the cold, dense background electrons of the target foil. In a recent study [1], we show that this approach is sufficient for targets with a step-like rear-side ion density profile (see Fig. 1). Such density profiles are usually present at the beginning of the TNSA process in experiments with relatively thick target foils. However, it was found that the models assuming a step-like target rear-side fail for thin targets (see Fig. 1 for $L \lesssim 10\mu\mathrm{m}$). It turns out that this is caused by a deviation of the target rear side from the assumed step-like shape. For thin targets, the laser prepulse leads to the formation of a finite rear-surface ion density gradient [2] (similar to Fig. 2a). In our study, we examine that for such an ion density profile neglecting the cold background electrons is no longer sufficient. Instead, one must consider both electron populations, hot and cold (2T-model).

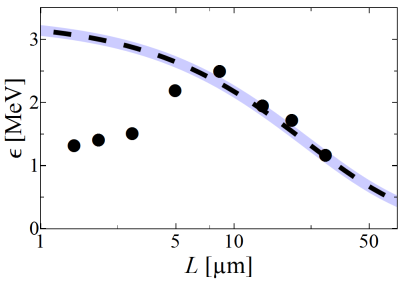

Figure 1: Comparison of the 1T model (light blue) curve) and the 2T model (dashed black curve) assuming a step-like ion density profile with experimental data (black dots) taken from Ref. [2].

Fig. 2 shows an example for the different results for the electric field obtained by the 1T- and the 2T-model for a non-step-like ion distribution. Here, a target with an exponential rear-side density gradient and a cutoff at varying position x_{cut} is considered. In the 1T-model, the electric field decreases with increasing value of x_{cut}. This is what one would expect according to Ref. [3]. However, for the 2T-model it turns out that the maximum electric field initially stays constant with increasing value of x_{cut}. Only for large values of x_{cut}, the maximum electric field starts to drop significantly. Hence, in this case the 1T- and the 2T-model predict remarkable different electric fields which lead to significantly different maximum ion energies. Since 2T-models are in general more accurate, this illustrates the need for such models in the case of laser-driven ion acceleration from targets with rear-surface density gradients.

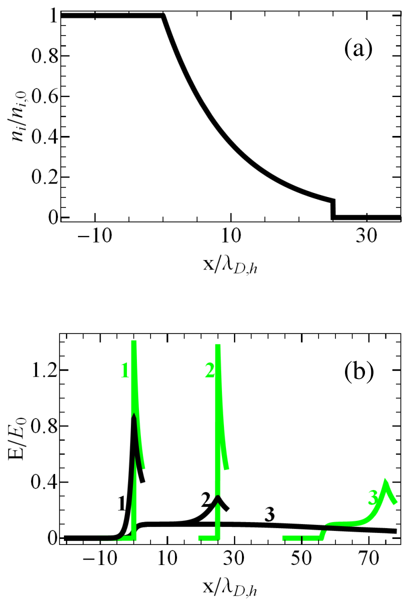

Figure 2: The electric field for a target with an exponential rear-side density gradient and a cutoff (cf. panel (a)). The decaying length is set to $10\,\lambda_{\mathrm{D,h}}$, where $\lambda_{\mathrm{D,h}}$ denotes the hot electron Debye length. In (b), the electric fields are plotted for the 1T-case (black curves) and the 2T-case (green curves) for cutoff positions $x_{\mathrm{cut}} = 0$, $x_{\mathrm{cut}} = 25\,\lambda_{\mathrm{D,h}}$ and $x_{\mathrm{cut}} = 75\,\lambda_{\mathrm{D,h}}$ labeled by "1", "2" and "3", respectively.

References

[1] T. Kiefer, T. Schlegel, and M. C. Kaluza. Impact of cold target electrons on laser-driven TNSA ion acceleration from foils with rear-surface density gradients. March 2015.

[2] M. Kaluza, J. Schreiber, M. I. K. Santala, G. D. Tsakiris, K. Eidmann, J. Meyer-ter-Vehn, and K. J. Witte. Influence of the laser prepulse on proton acceleration in thin-foil experiments. *Phys. Rev. Lett.*, 93(4):045003, 2004.

[3] T. Grismayer and P. Mora. Influence of a finite initial ion density gradient on plasma expansion into a vacuum. *Phys. Plasmas*, 13:032103, 2006.

Photon and Particle Spectroscopy

First X-Ray Measurements with a Magnetic Metallic Calorimeter at the ESR Storage Ring

T. Gassner[*1,2], G. Weber[1,2], R. Märtin[1,2], Th. Stöhlker[1,2,3], D. Hengstler[4], M. Keller[4], C. Schötz[4], J. Geist[4], M. Krantz[4], S. Kempf[4], L. Gastaldo[4], A. Fleischmann[4], and C. Enss[4]*

[1]Helmholtz Insitute Jena, Jena, Germany; [2]GSI, Darmstadt, Germany; [3]Institute for Optics and Quantum Electronics, Jena, Germany; [4]Kirchhoff-Institute for Physics, Heidelberg, Germany

Presently the Facility for Antiproton and Ion Research (FAIR) which will be an expansion to the GSI Helmholtz Centre for Heavy Ion Research is under construction and first beams are expected in 2019. FAIR will deliver ion beams with unprecedented intensities and quality which will open a window to observe physical effects which were not accessible with previous facilities.

To benefit the most from these exciting opportunities the detector portfolio of the Helmholtz Institute Jena has to be upgraded with the most advanced systems available. For this purpose a collaboration was started with the ultra-low temperature group of the Kirchhoff-Institute for Physics (KIP) from the university of Heidelberg in order to develop the next generation of **m**icrocalorimeter **a**rrays for high-resolution **X**-ray **s**pectroscopy (maXs) [1]. The energy resolution of these detectors is more than one order of magnitude higher than that of the best conventional high-purity semiconductor detectors. Due to the large active area accomplished by 64 individual pixels a reasonable efficiency can be guaranteed. In 2013 a modern dilution refrigerator was bought by the Helmholtz Institute Jena and detector prototypes were fabricated in Heidelberg. In first laboratory tests it could be demonstrated that the achieved resolution is comparable to the one obtained with the best systems available word-wide.

In two test beam times in April and August 2014 the performance of the prototypes was investigated at the ESR storage ring at the GSI Helmholtz Centre. Since the working principle of the calorimeter relies on the measurement of magnetisation of a diamagnetic probe it was not clear if a good performance could be achieved in a storage ring environment where strong and fast ramping magnetic fields are omnipresent. Both tests were conducted very successfully since the achieved resolution was as good as in the well controlled laboratory environment.

Figure 1 shows, in blue, a preliminary x-ray spectrum of a Xe^{54+} ion beam hitting a Xe gas-jet target. The kinetic energy of the ion beam amounted to 50 MeV/nucleon and the spectrum was recorded under an emission angle of 60° with respect to the ion-beam direction. At an x-ray energy around 30 keV a broad structure can be seen which stems from Xe gas which emits K_α radiation at different energies depending on the charge state created by the collision ranging from Xe^{+} up to Hydrogen-like Xe^{53+}. In the vicinity of 35 keV the K_α radiation of H-like and He-like $Xe^{53+/52+}$ can be observed which corresponds to the characteristic radiation emitted by an ion in the beam following a single or double electron capture in the target, respectively. For higher energies different characteristic transitions in the H- and He-like system can be identified ranging up to K_η radiation (n = 7 → 1) for H-like Xe^{53+}. To compare these marvellous results with a conventional high resolution semiconductor detector the whole spectrum has been convoluted with a Gaussian profile (600 eV FWHM) and plotted in red into the same graph. As can be seen several lines (like the K_α or $K_{\delta-\eta}$) appear blended if observed with a semiconductor detector preventing a more precise analysis of each individual transition. It could successfully be demonstrated that the development of the next generation of x-ray detectors is on a very promising path which will enable the Helmholtz Institute Jena to extract significant measurement data from this world-unique facility.

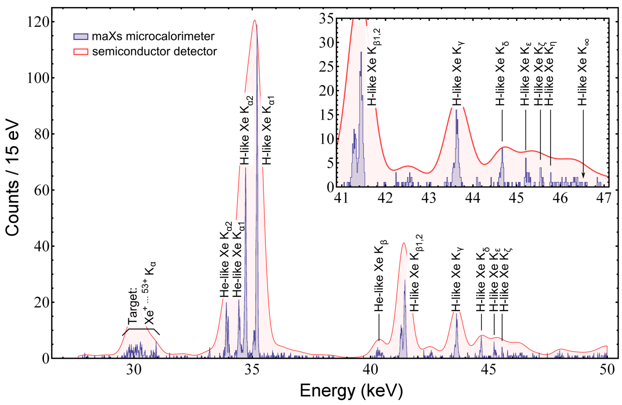

Figure 1: *Blue*: preliminary x-ray spectrum from the maXs microcalorimeter recorded at the collision of a 50 MeV/nucleon Xe^{53+} ion beam with a Xe gas-jet target. *Red*: Estimated spectrum of the same process recorded with a conventional semiconductor detector.

References

[1] C. Pies *et al.*, maXs: Microcalorimeter Arrays for High-Resolution X-ray Spectroscopy at GSI/FAIR, Journal of Low Temperature Physics **167**, 269-279 (2012)

* t.gassner@gsi.de

Experimental studies on elastic X-ray scattering*

K.-H. Blumenhagen†[1,2,3], *T. Gaßner*[1,2,3], *A. Gumberidze*[3,4], *R. Märtin*[1,3], *N. Schell*[5], *U. Spillmann*[3], *S. Trotsenko*[1,3], *G. Weber*[1,3], *and Th. Stöhlker*[1,2,3]

[1]HI-Jena, Germany; [2]IOQ, University of Jena, Germany; [3]GSI, Darmstadt, Germany; [4]EMMI, Darmstadt, Germany; [5]HZG, Geesthacht, Germany

Photon scattering in the presence of strong electromagnetic fields has been studied in an experiment where hard X-rays (175 keV) were elastically scattered by a high-Z (gold) target. Previous studies already covered a broad range of photon energies and target materials [1, 2]. While in most of those experiments the differential scattering cross section was studied, we performed a combined measurement of the angular distribution and the angle-dependent linear polarization of elastically scattered hard X-rays. As in this energy regime the scattering cross section is relatively small, in particular at backward angles, a high-intensity photon source for monoenergetic hard X-rays was required. Moreover, for our study we wanted to use polarized inicdent X-rays. These requirements made the use of a novel 3rd generation synchrotron radiation source mandatory. On the other hand, we needed an efficient polarization-sensitive detector which could be fulfilled with a large-volume, segmented solid state detector that can act as a Compton polarimeter. The incident 175-keV photon beam was provided by the High Energy Material Science Beamline P07 [3] at the synchrotron radiation source PETRA III at DESY, Hamburg. It was scattered by a thin solid gold target and the scattered radiation was detected by a 2D Si(Li) strip polarimeter [4] and a standard high-purity germanium detector. This setup allowed the parallel measurement of the differential cross section and the polarization. In this report, we present preliminary results for the differential cross section, the analysis of the polarization will follow later. Figure 1 (a) shows the energy spectrum of the germanium detector mounted at a scattering angle $\theta = 30°$. The main features are the Rayleigh peak (elastically scattered photons), the Compton peak (inelastically scattered photons) and the Au Kα and Kβ lines (fluorescence from the target). The differential cross section is obtained by determining the intensity of the Rayleigh peak and normalizing it to (i) the Au-Kα_1 cross section and (ii) the Compton cross section. This procedure allows to cancel effects from the experimental geometry and fluctuations in the incident beam intensity. The main task of the data analysis was the area determination of the Kα_1-, the Compton- and the Rayleigh peak. For the narrow Kα_1- and Rayleigh lines, the sum of an analytical peak shape and a linear background was fitted to the data. For the broad Compton peak, a non-analytical fit curve based on the theoretical Compton profile of gold was created. A Monte Carlo simulation corrected the distribution for photons that were scattered from parts of the target chamber. The spectrum from the simulation - corrected for detector efficiency and resolution was then the fit function. Preliminary results are shown in figure 1 (b).

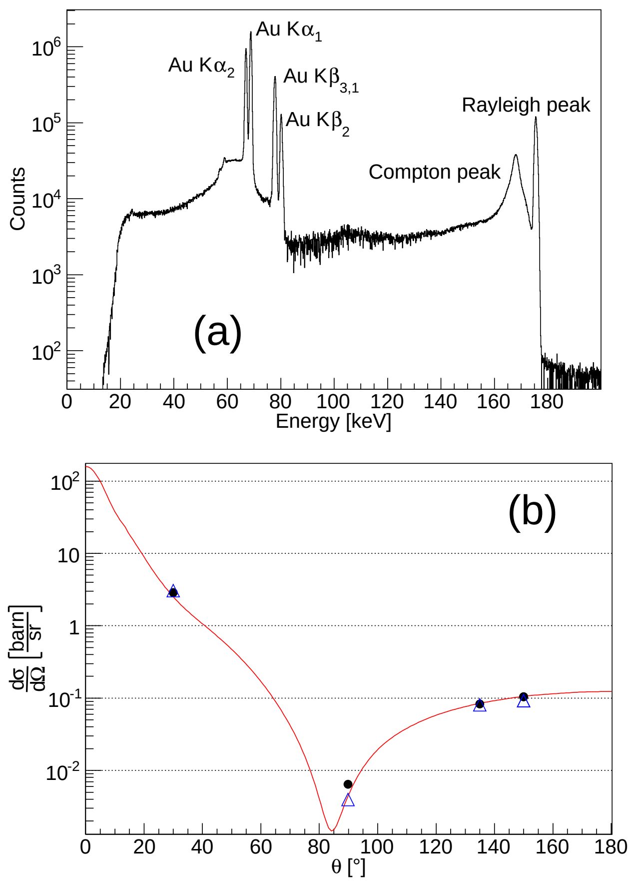

Figure 1: Preliminary results: (a) Energy spectrum of the germanium detector at $\theta = 30°$; (b) Differential cross section: Kα_1 normalization (solid circles), Compton normalization (open triangles), preliminary theory [5] (solid line). Statistical errors are smaller than the point size, systematic errors are not yet included.

* Work supported by HGS-HIRe / Helmholtz Alliance (HA216/EMMI) / DESY and HZG support at beamline P07.

† k.-h.blumenhagen@gsi.de

References

[1] P. P. Kane et al., Phys. Rep. 140, 75-159 (1986).

[2] D. A. Bradley et al., Radiat. Phys. Chem. 56, 125-150 (1999).

[3] N. Schell et al., Mater. Sci. Forum 772, 57-61 (2014).

[4] D. Protic et al., IEEE Trans. Nucl. Sci. 53, 3181-3185 (2005).

[5] A. Surzhykov et al., submitted to J. Phys. B.

Precise polarization studies of radiative electron capture

G. Weber[*1,2], *H. Ding*[2,3], *H. Bräuning*[1], *R. Hess*[1], *S. Hess*[1], *R. Märtin*[1,2], *U. Spillmann*[1], *S. Trotsenko*[1,2], *D. F. A. Winters*[1], *and Th. Stöhlker*[1,2,3]

[1]GSI, Darmstadt, Germany; [2]Helmholtz Institut Jena, Germany; [3]IOQ, FSU Jena, Germany

The capture of electrons into bound states of ions is of significant importance for both experiment and theory in the fields of atomic and plasma physics as well as for astrophysics. The capture process is called radiative if it is accompanied by the emission of a photon that carries away the initial electron's kinetic energy and the binding energy of the final state it is captured into. If the initial electron is considered to be free, the capture process is referred to as radiative recombination (RR), being the time-reversal of the photoelectric effect, whereas the capture of a bound electron is called radiative electron capture (REC) [1].

The REC process is a prominent charge-changing process for fast, highly-charged ions interacting with dedicated target materials or with residual gas being present in the beamlines of accelerators and storage rings. Moreover, when low- to medium-Z targets and heavy, highly-charged projectile ions are considered, the to-be-captured electrons can be treated as free particles having a momentum distribution equal to the one of the bound target states. This so-called impulse approximation reduces the REC description to the RR cross section convoluted with the incident electron momentum distribution. Consequently, both the REC and the RR process as well as the photoeffect can be treated within the same theoretical framework. Moreover, when compared to the photoeffect, the RR/REC process offers several experimental advantages, such as a more uniform emission pattern due to the partial cancelation of retardation and Lorentz transformation for a moving emitter system and the fact that x-rays, in contrast to electrons, can typically leave the target zone unaffected by secondary-collision effects. These facts motivated various REC measurements aiming for a deeper insight into the photoeffect while exploiting the advantageous experimental conditions present for the study of electron capture into fast, highly charged ions.

A first study of the linear polarization of REC photons was published in 2006 [2] where a 4×4 pixel Ge(i) detector was used for Compton polarimetry of x-rays emitted in collisions of bare uranium ions with a N_2 target at the experimental storage ring (ESR) of GSI. The experimental findings are presented together with theory values in figure 1a. Having only 16 pixels, the relatively low granularity of the detector resulted in a poor angular resolution of the Compton scattering distribution, which limited the experimental accuracy to an uncertainty between $\pm 5\,\%$ and $\pm 10\,\%$ with respect to the degree of linear polarization. The much higher granularity of a newly developed Si(Li) polarimeter [3](see figure 1b) enables more precise studies and this instrument was already applied in a series of test measurements also addressing the REC radiation [4,5]. Data analysis is still in progress and we expect an experimental uncertainty for these new polarization studies in the order of $\pm 1\,\%$ of the degree of linear polarization. With regard to future experiments at the new FAIR facility it is worth noting that while the existing ESR is limited to typical ion energies not higher than 400 MeV/u for beams of heavy ions, the planned high-energy storage ring (HESR) will reach up to approximately 5 GeV/u for bare uranium. With the extended energy range it will become possible to probe the cross-over effect in the degree of REC photon linear polarization which is predicted to occur at collision energies above 600 MeV/u and for forward emission angles, see the theory data for 800 MeV/u in figure 1a. In terms of the photoeffect this feature indicates that the initially bound electron is no longer preferentially ejected in the direction of the incident photon electric field vector, instead emission along the magnetic field vector is dominant.

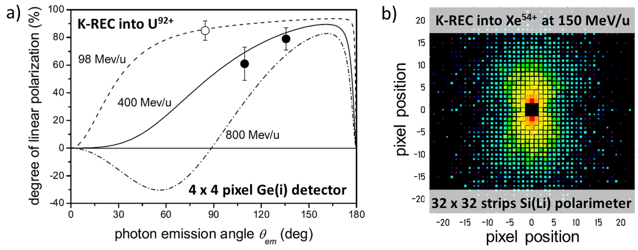

Figure 1: a) Degree of linear polarization of the radiative electron capture (REC) into the K-shell of bare uranium projectiles measured with a 4×4 pixel Ge(i) detector applied as a Compton polarimeter [2]. b) Position distribution of Compton scattered K-REC photons inside the Si(Li) polarimeter for the capture into bare xenon ions. Data analysis with respect to the degree of linear polarization is ongoing. The much higher granularity of the new detector is expected to enable significantly more precise measurements compared to the 16 pixel detector.

References

[1] J. Eichler and Th. Stöhlker, Phys. Rep. **439** (2007) 1

[2] S. Tashenov et al., Phys. Rev. Lett. **97** (2006) 223202

[3] G. Weber et al., JINST **5** (2010) C07010

[4] S. Hess et al., J. Phys. Conf. Ser. **163** (2009) 012072

[5] S. Hess et al., J. Phys. Conf. Ser. **194** (2009) 012025

* g.weber@gsi.de

Towards a fast calculator for the radiation characteristics of radiative recombination and radiative electron capture

G. Weber[*1,2], *H. Ding*[2,3], *M. O. Herdrich*[2,3], *and A. Surzhykov*[2]

[1]GSI, Darmstadt, Germany; [2]Helmholtz Institut Jena, Germany; [3]IOQ, FSU Jena, Germany

The radiative capture of free electrons (radiative recombination, RR) and bound electrons (radiative electron capture, REC) are among the most important charge changing processes for fast, highly-charged ions passing through matter. In particular for ongoing highly-charged ion studies at the ESR and for future experimental campaigns planned at the CRYRING@ESR and the high-energy storage ring (HESR) of the FAIR facility, precise knowledge of REC characteristics in a broad range of collision energies from about 1 MeV/u up to 5 GeV/u is highly desirable. When low- to medium-Z targets and heavy, highly-charged projectile ions are considered, the to-be-captured electrons can be treated as free particles having a momentum distribution equal to the one of the bound target states. This approximation reduces the REC description to the RR cross section folded with the incident electron momentum distribution. Consequently, both the REC and the RR processes, as well as the photoeffect (the time-reversal of RR), can be treated within the same theoretical framework [1]. While total cross sections can be obtained by an approximate formula with reasonable accuracy, the estimation of angular distributions and polarization properties of the emitted radiation requires a fully relativistic treatment that is numerical expensive. Therefore we recently started the development of a fast calculator (called RECAL) for all relevant characteristics of RR and REC photons. The program is based on a grid of rigorously calculated data points for RR into bare ions, between which interpolation is performed to obtain radiation characteristics for specific collision systems.

For the grid points, differential cross sections and linear polarization values of the RR photons were calculated using parts of the DIRAC toolkit, see [2]. The accuracy of the RR calculation is mainly determined by the accuracy of the continuum wavefunction representing the initial state of the incident electron, which is described by a series expansion in terms of partial waves. A careful choice of the number of partial waves, defined by $\nu = 2\kappa_{\text{max}}$, with κ_{max} being the maximum number for the Dirac angular momentum to be taken into account, is of particular importance. More precisely, a too small choice of κ_{max} may lead to truncation errors, while, on the other hand, a too large value increases significantly computation time (approximately scaling with κ^3_{max}) and eventually leads to an explosion of numerical errors due to the rapid oscillations of the radial part of the continuum wavefunction.

For first test calculations, we generated a RR data base of capture into bare projectiles for atomic numbers Z between 1 and 92 and more than 100 kinetic energies between 2 MeV/u and 1 GeV/u. A comparison of angular differential RR cross sections obtained from the RECAL interpolation algorithm to fully relativistic calculations from [3] is shown in Fig. 1. Here the radiation stemming from the capture of free electrons into the ground state of bare lead ions was studied for several collision energies. An increasing deviation at high collision energies is seen, most probably due to an improper choice of κ_{max} for the underlying RR data base of the RECAL program. Currently, we are working on an optimized data base to provide reliable RR/REC cross section and linear polarization values for arbitrary collisions systems at ion beam energies between 1 MeV/u and 5 GeV/u.

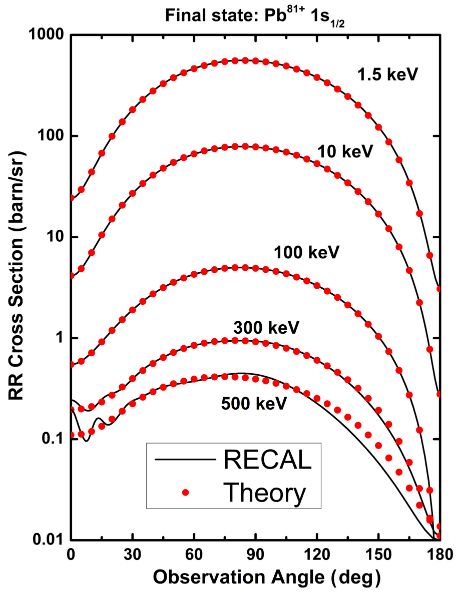

Figure 1: Angular differential RR cross sections for electron capture into the ground state of bare lead ions. Fully relativistic calculations from [3] are compared to RECAL predictions. An increasing deviation at high collision energies is seen due to an improper choice of κ_{max} for the underlying data base of the RECAL calculator.

* g.weber@gsi.de

References

[1] J. Eichler and Th. Stöhlker, Phys. Rep. **439** (2007) 1

[2] A. Surzhykov et al., Comput Phys Commun **165** (2005) 139

[3] A. Ichihara and J. Eichler, At. Data Nucl. Data Table **79** (2001) 187

Study of the two-photon decay in He-like gold

S. Trotsenko[1,2], D.Banas[3], A.Gumberidze[2], C.Kozhuharov[2], R. Zhang[2], A. Ananyeva[2,5], H.Beyer[1,2], K.-H. Blumenhagen[1,7], C. Brandau[2,4], A.Bräuning-Demian[2], W. Chen[2], B. Gao[2], T. Gassner[1,2,7], S.Hagmann[2,5], P.-M. Hillenbrand[2], M. Lestinsky[2], Y. Litvinov[2], N. Petridis[2], S. Schippers[4], D. Schury[2], U.Spillmann[2], C. Trageser[2,4], M. Trassinelli[6], X. Tu[2], D. Winters[2], X. Zhu[2], and Th. Stöhlker[1,2,7]

[1]Helmholtz-Institut Jena, D-07743 Jena, Germany; [2]GSI Helmholtzzentrum für Schwerionenforschung, D-64291 Darmstadt, Germany; [3]University of Kielce, Kielce, Poland; [4]Justus-Liebig-Universität Giessen, Germany, [5]University of Frankfurt, Frankfurt a.M., Germany; [6]INSP, CNRS and UMPC, Paris, France; [7]Friedrich-Schiller-Universität Jena, D-07743 Jena, Germany

Further experiment from our program on studies of the two-photon transitions in heavy highly charged ions [1-3] at the experimental storage ring (ESR) is presented in this contribution.

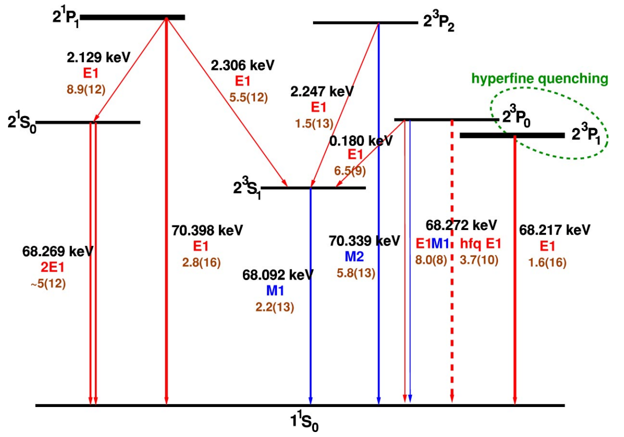

Figure 1: Level scheme of He-like gold with transition energies, decay modes, and transition probabilities indicated. The transition probabilities are in 1/s with numbers in brackets indicating powers of 10 [4].

K-shell ionization of Li-like high-Z projectiles occurring in ion-atom collisions has been found to be a highly selective mechanism for the population of singly excited states (1s2s) in He-like ions [1-3]. They decay to the ground state via M1 (2^3S_1-1^1S_0) and 2E1 (2^1S_0-1^1S_0) transitions (Fig. 1). Most important, this process allows one to measure the undistorted two-photon energy distribution for the 2E1 decay of the [1s2s] ($^1S_0$) state, which is of particular interest for a decisive test of theoretical predictions.

Extending our previous experiments on He-like ions to the measurement of a system with non-zero nuclear spin, we present here first data of the two-photon decay energy distributions in He-like gold (Z=79). The experiment was performed at the storage ring ESR with 300 MeV/u Li-like gold ions (Au^{76+}) colliding with N_2 target. For the details of the experimental setup we refer to [1-3]. In Fig. 2 (bottom) we present a preliminary spectrum measured by a Ge x-ray detector in coincidence with the up-charged Au^{77+} ions. The spectrum is dominated by an intense line at 51.5 keV (lab. frame) corresponding to the M1 de- cay of the [1s2s] $^3S_1$ state and a broad continuum towards lower energies representing the 2E1 decay of the [1s2s] $^1S_0$ level. For comparison, in Fig. 2 (top) we present a total x-ray spectrum (no coincidences). Note, the absence of x-rays lines from the decay of the 2p or higher states (Fig. 2: bottom) ensures that there is no intra/inter-shell excitation simultaneous with the K-shell ionization (compare [1-3]). The data analysis is in progress.

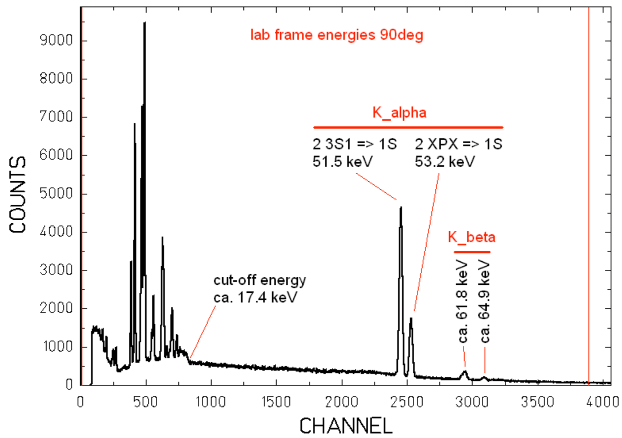

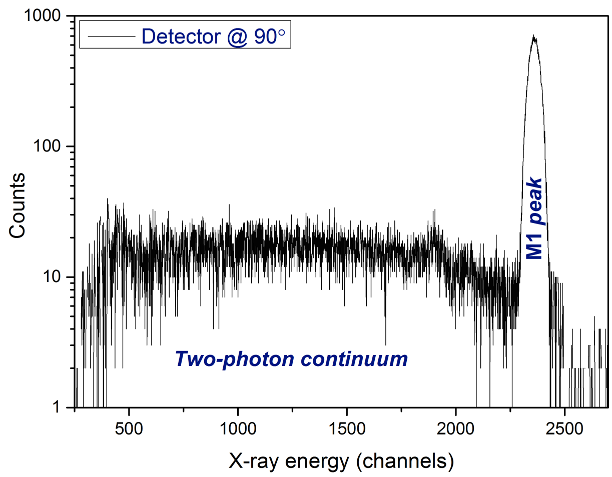

Figure 2: Preliminary projectile x-ray spectra as registered by the Ge-detector without coincidences (top), and with coincidences (bottom) with ionization particle detector.

References

[1] D. Banas et al., PRA 87, 062510 (2013)
[2] S. Trotsenko et al., PRL 104, 033001 (2010)
[3] J. Rzadkiewicz et al., PRA 74, 012511 (2006)
[4] S. Toleikis et al., PRA 69, 022507 (2004)

Preparations for the investigation of the refractive index at γ-ray energies

M. M. Günther[1,2,#], M. Jentschel[3], M. Zepf[2], W. Ziegler[2]
[1]GSI, Darmstadt, Germany; [2]Helmholtz-Institut Jena, Jena, Germany; [3]Institut Laue-Langevin, Grenoble, France

The knowledge of the refractive properties of materials plays an important role in many optical applications. In biomedical and material science refractive optics are well established and used in the energy range of soft x-rays up to hard x-rays. Very recent investigations of the refractive index of several materials were done up to 133 keV hard x-ray energy [1]. A next step is the application of refractive optics in the γ-ray energy range. In many nuclear science applications as well as material and radio oncology science such optics would be an interesting tool. However, the refractive behaviour of materials at such high photon energies is'nt well known. First experiments on Silicon were performed at the ILL in Grenoble (France) [2]. The result was surprising because an enhancement was observed about 1 MeV γ energy. Up to now the observed refractive properties in the energy range about 1 MeV couldn't be completely explained. The refraction index is related to a complex scattering amplitude. Therefore, to learn more about the index of refraction it is necessary to investigate scattering physics at materials with different atomic charge numbers Z. In an experimental campaign starting 2015 the refractive index will be measured at different materials in an energy range from several hundreds of keV up to several MeV. The experiment will be performed on the new GAMS6 high resolution double flat crystal γ-spectrometer at the ILL high flux reactor in Grenoble (France) (see Figure 1).

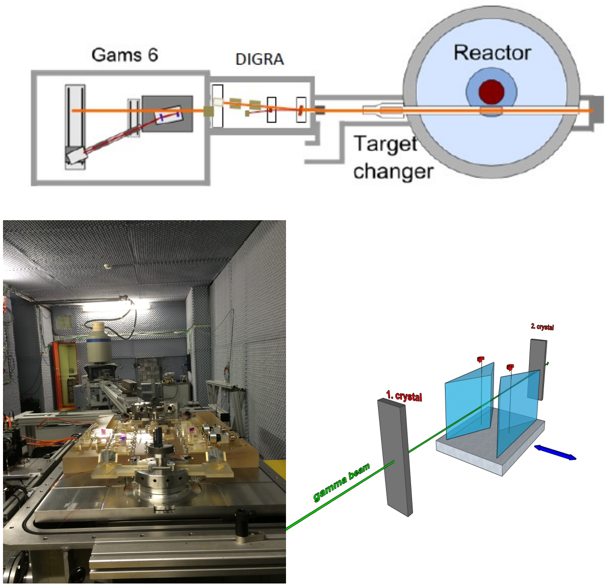

Figure 1: GAMS6 and schematic of the experiment systematic (see text)

A spectrometric method is used for the measurement of the angular deviation of a γ beam after the propagation through a prism. At γ-ray energies the expected deviation angle is within the range of about 10^{-8} radians because refraction is very weak. A double flat perfect Si crystal high resolution γ spectrometer is used [3]. The spectrometer is operated in non-dispersive geometry. The first crystal defines the γ energy band by Bragg diffraction and collimates the beam. The second crystal acts as an angle analyser by rocking around the vertical axis. The rotation angle is controlled by a heterodyne Michelson interferometer. The angular resolution is about 10^{-9} radian. After propagation of the beam through the two crystals the angular intensity profile is measured by a HPGe detector. The maximum of the rocking curve presents the angular position of the γ beam. Therefore, by positioning a prism between the two crystals the deviation angle is measured, related to the index of refraction. The γ beam is generated by neutron capture processes of an in-pile $BaCl_2$ target close to the nuclear fission reactor core, where the ^{36}Cl is the γ source. The γ emission rate is about 10^{16} γ/s. The γ beam is collimated with the result of a 2 mm small beam at GAMS6 with a flux of more then 10^9 γ/s. Besides new Si and Ge prisms, fused silica hollow prisms are used each with a prism angle of 120 degree. The hollow prisms are filled with different compound and pure Z fluids.

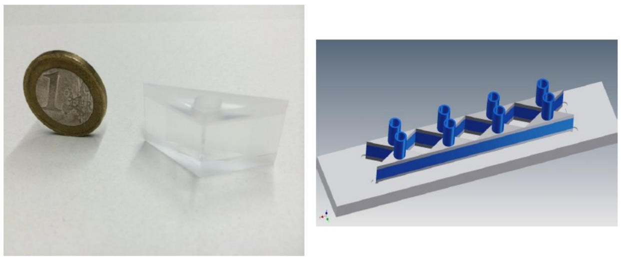

Figure 2: Hollow prism system.

Prism pairs of the same material but opposite prism angle on the right and the left side are placed on the prism mount within the beam (see Figure 1 and 2). By moving the prism right and left within the beam, the prism pairs refract the beam in opposite directions. This allows on the one hand to measure smaller refractive effects and on the other hand to use lower prism angles, which reduces the attenuation.

References

[1] M. Ruiz-Yaniz et al., Phys. Rev A **91**, 033803 (2015)
[2] D. Habs, M.M. Günther et al., Phys. Rev. Lett. **108**, 184802 (2012)
[3] E.G. Kessler Jr. et al., NIM A **457**, pp. 187-202 (2001)

m.guenther@gsi.de

Precision measurement of undulator polarization

B. Marx[2], K.S. Schulze[1,2], I. Uschmann[1,2], T. Kämpfer[1,2], O. Wehrhan[1,2], H.C. Wille[3], K. Schlage[3], R. Röhlsberger[3], E. Weckert [3], T. Stöhlker[1], E. Förster[1,2] and G.G. Paulus[1,2]

[1]Helmholtz-Institut Jena, Germany; [2]Friedrich-Schiller-Universität Jena, Germany; [3]Deutsches Elektronen Synchrotron DESY, Germany.

Today, undulators are the fundamental devices of the most brilliant x-ray sources. Their conception was described by Ginzburg in 1947 [1]. The first undulator was built up by Motz and coworkers in 1953 [2]. Many studies on undulator radiation has been performed since then, but only few on polarization properties. The knowledge of the precise polarization of undulator radiation is one of the most important properties for their application and of fundamental interest to the increasing community of scientists using XFEL- and synchrotron radiation. So we have measured the degree of linear polarization purity with hitherto unachievable precision at an undulator beamline at Petra III [3].

Polarization Measurement

The measurement of the undulator polarization was performed at the "High Resolution Dynamics Beamline" P01 at DESY. The undulator at P01 is built up of two segments with a 32mm period. Each of the segments is 5m long and has a minimum gap of 12.5mm. Figure 1 shows schematically the setup of the measurement.

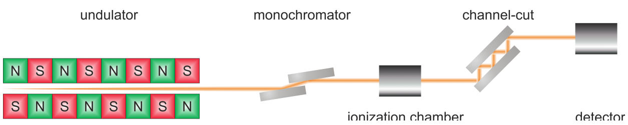

Figure 1: Experimental setup of the polarization precision measurement of the undulator at beamline P01 in Hamburg (DESY).

The incoming beam from the undulator was monochromatized by a Si (111) double crystal monochromator, restricted by a variable slit and finally analysed by a 6- reflection silicon (800) channel-cut crystal. To set up the energy at exact 12914eV, a silicon crystal monolith with reflecting surfaces parallel to the (100) and (010) planes was used instead of the channel-cut crystal, in a first step. For the precision measurement of the undulator polarization, the channel-cut crystal was rotated around the beam axis (η) by a goniometer with a full-step resolution of 0.9 arc sec. In each η-position the rocking curve was recorded by a second goniometer with the same resolution. The incoming flux on the crystal was monitored by an ionization chamber. As detector, we used a calibrated silicon photodiode. To restrict the horizontal and vertical divergence of the beam, the measurements were done for two different slit sizes. One for an aperture of 1mm x 1mm and the other for 3mm x 3mm.

Results

Figure 2 shows the integrated intensity of each rocking curve normalized to the integrated intensity of the rocking curve in the parallel position (η=0°) for an aperture of 3mm x 3mm.

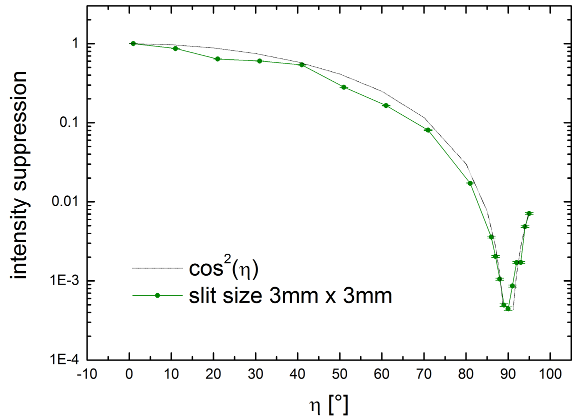

Figure 2: Results of the polarization purity measurement for a slit size of 3mm x 3mm (green line).

The degree of polarization purity was determined to $\delta_0=(2.4\pm0.2)\times10^{-4}$. This value differs from the theoretical value of $\delta_0=5.9\times10^{-5}$ of the beamline for the same parameters. The difference could be explained by a slight shift of the slit position to the center of the beam by 0.7mm during the measurement. In conclusion we showed a very precise and easy method to measure the degree of polarization purity at synchrotron and XFEL facilities.

References

[1] V. L. Ginzburg, "On emission of micro waves and their absorption in air,"Izv. Akad. Nauk. SSSR, Ser. Fiz 1, 165 (1947)

[2] H. Motz, W. Thon, and R. N. Whitehurst, "Experi ments on radiation by fast electron beams," J. Appl. Phys. 24, 826 (1953)

[3] B. Marx, K.S. Schulze, I. Uschmann, T. Kämpfer, O. Wehrhan, H.C. Wille, K. Schlage, R. Röhlsberger, E. Weckert, E. Förster, T. Stöhlker and G.G. Paulus, "High precision measurement of undulator polarization", Applied Physics Letters 105, 2014.

Polarisation Gating of Attosecond Pulse Trains in the Relativistic Regime

M. Yeung[1], J. Bierbach[1,2], S. Kuschel[1,2], G. Paulus[1,2], C. Rödel[1,2], S. Rykovanov[1], E. Eckner[2], M. Förster[2], M. Coughlan[3], S. Cousens[3], B. Dromey[3] and M. Zepf[1,2,3]

[1]Helmholtz Institute Jena, Fröbelstieg 3, 07743 Jena, Germany; [2]Institute for Optics and Quantum Electronics, Friedrich-Schiller Universität, Max-Wien-Platz 1, 07743 Jena, Germany; [3]Queen's University Belfast, University Road, BT7 1NN, UK

Overdense plasma surfaces driven by intense laser pulses to relativistic velocities can Doppler upshift the reflected light to extreme-ultraviolet wavelengths in a process that can be modelled as a relativistically oscillating mirror (ROM) [1]. This process occurs each laser cycle and produces a train of pulses of attosecond scale duration which could potentially be used to probe the dynamics of bound electrons in atomic and molecular systems. This pulse train is observed as high harmonics of the driving laser frequency.

Reducing the pulse train to a single isolated pulse requires temporal gating of the generation mechanism. One common method is the polarisation gating technique [2] that has been extensively studied for high harmonic generation (HHG) due to electron recombination in gaseous media. If the generation mechanism is suppressed when the laser is elliptically polarised then a pulse which changes from circular to linear to circular polarisation can gate the process. Indeed HHG from the ROM mechanism is known to be suppressed by elliptical polarisation in normal or near-normal incidence interactions [1,3].

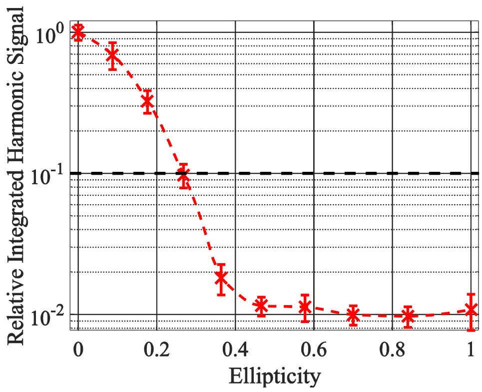

Figure 1: Ellipticity dependence for harmonics 13 to 28

Using the 30fs, 800nm, 700mJ JETI40 Ti:Sapphire laser system, a proof of principle experiment was performed to test a novel polarisation gating method whereby the laser beam is split into two half beams with opposite handed circular polarisation which then interfere at focus to create a linear gate for the region of temporal overlap. This method has the advantage that it minimises transmissive optics which are used in other polarisation gating schemes and can lead to B-integral problems in very high power systems. Furthermore, the gating is enhanced because the two circular pulses are not collinear with the gated pulse and have a larger focal spot area.

The laser pulse was contrast enhanced by a plasma mirror and focused with an F-3 off-axis parabola onto a fused silica target at an angle of incidence of 22.5°. The reflected radiation was filtered by a 200nm aluminium foil and detected in a one to one imaging spectrometer consisting of a toroidal mirror and gold transmission grating.

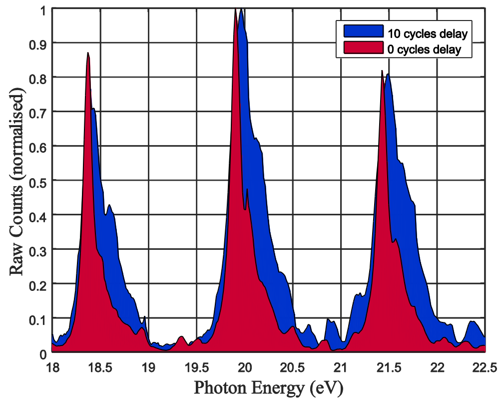

Figure 2: Normalised spectra for ungated (front shaded area) and gated (back shaded area) pulses.

A full-beam quarter waveplate was used to test the ellipticity dependence for this geometry (figure 1) for a peak intensity of ≈$5X10^{19}Wcm^{-2}$. Clear suppression of the harmonic signal is observed for circular polarisation while the relative signal is 10% for an ellipticity of 0.27 which is comparable to HHG from gases.

The polarisation gating setup consisted of two 500 μm fused silica wafers which can be rotated to control the relative phase and delay of each half beam and a split mica quarter wave plate which makes each beam half circular with opposite handedness. For no delay between the pulses (no gate) the intensity is ≈$2X10^{19}Wcm^{-2}$. Observed spectra averaged over 10 shots are shown in figure 2 where clear broadening of the harmonics is seen in the gated case. The gated harmonic bandwidth corresponds to an ideal pulse train of 3.5 pulses (at the 10% level) which is broadly consistent with the expected gate width which is, from considering only the gating from the ellipticity variation, approximately 4 cycles.

In conclusion, a new method using split beams to achieve polarisation gating of attosecond pulse trains has been demonstrated. This method is well-suited to large diameter high power laser beams.

References

[1] R. Lichters *et al.*, Phys Plasmas 3 (1996) 3425
[2] P. B. Corkum *et al.* Opt. Lett. 19 (1994) 1870
[3] S. G. Rykovanov *et al.* New J. Phys. 10 (2008) 025025

Generation of soft X-rays up to the water window with a high average power few-cycle fiber laser

Jan Rothhardt,[1,2] Steffen Hädrich,[1,2] Arno Klenke,[1,2] Stefan Demmler,[1] Armin Hoffmann,[1] Thomas Gotschall[1], Manuel Krebs,[1] Tino Eidam,[1,2] Jens Limpert,[1,2,3] Andreas Tünnermann,[1,2,3]

[1]Institute of Applied Physics, Friedrich-Schiller University Jena, [2]Helmholtz-Institute Jena,
[3]Fraunhofer Institute of Applied Optics and Precision Engineering, Jena

Few cycle laser pulses are of enormous interest due to their short pulse duration and electric field asymmetry. High harmonic generation particularly benefits from such pulses, which allow to phase match higher photon energies and to generate isolated attosecond pulses. So far most few-cycle lasers are based on post compression of Ti:Sa laser system and, thus, limited in average output power and repetition rate.

Here, a femtosecond fiber chirped pulse amplifier (FCPA) system [1] is employed for the generation of energetic few-cycle laser pulses at high repetition rate and average power. The FCPA incorporates coherent combination of two fiber amplifiers delivering ~210 fs, 1 mJ pulses at 150 kHz repetition rate. These pulses are subsequently shortened in two hollow-fiber based post-compression stages. The first stage consists of a 1 m long hollow-fiber (250 µm diameter) filled with 2.5 bar of argon for spectral broadening. The second stage utilizes a 0.5 m long hollow-fiber (250 µm diameter) filled with 8 bar of neon for further spectral broadening. Chirped mirrors are employed to compress the pulses down to 30 fs after the first stage [2]. After the second stage ultra-broadband chirped mirrors are employed to compress the pulses to only 7.8 fs (2.4 optical cycles) pulse duration. The compressed pulse energy is ~350 µJ, which corresponds to an average output power as high as 53 W at 150 kHz repetition rate. This value represents the highest average power provided by any few-cycle laser system so far [3].

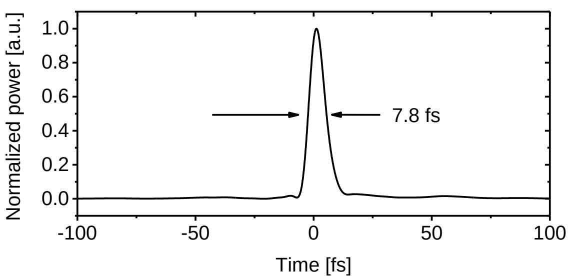

Figure. 1. Temporal profile of the few-cycle laser pulse characterized by SPIDER.

High harmonic generation (HHG) experiments demonstrate the unique capabilities of this laser system. More than 10^9 photons/second have been generated in a neon gas jet within a 1 % bandwidth at 120 eV. Helium even allowed reaching a high photon flux (>10^6 photons/s) within the water window spectral region. Two spectra recorded with and without an additional Parylene N filter clearly show the generated photon flux beyond the carbon absorption edge.

This unique table-top high photon flux soft X-ray source will pave the way e.g. for nanometer-scale imaging and element- and chemical bond selective studies near X-ray absorption edges.

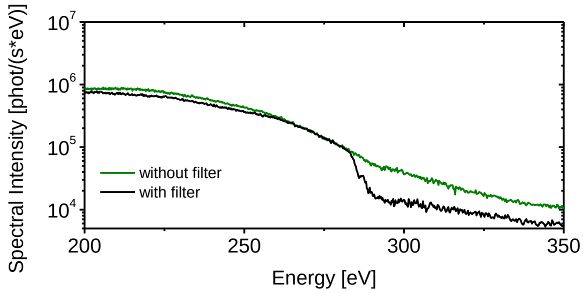

Figure 2. HHG spectrum recorded with (black) and without (green) and additional Parylene N filter. The carbon K-edge at ~284 eV is clearly visible.

Currently, thermally-induced deformations of the metal-coated mirrors employed for beam steering limit the average output power of the laser system. However, broadband dielectric mirrors will reduce such effects by more than an order of magnitude. The average power scalability has been further investigated by coupling a 1 kW cw fiber laser into the hollow fiber used for the first compression stage. A transmitted average power of 712 W has been obtained for more than 20 minutes without thermal drifts and with excellent (fundamental mode) beam quality.

Thus, we are confident that multi-100-W average power, multi-millijoule pulse energy few-cycle lasers will be feasible with the presented approach in the near future. As a result, the photon flux of coherent soft X-rays sources will increase accordingly. In addition, the carrier envelope phase stabilization of the whole laser system will be investigated in future.

Hence, a new class of high power few-cycle lasers will be available for applications in attoscience, strong-field physics and laser-particle acceleration.

References

[1] A. Klenke et al., Opt. Lett. **38**, 2283–2285 (2013).
[2] S. Hädrich et al., Opt. Lett. **38**, 3866–3869 (2013).
[3] J. Rothhardt et al., Opt. Lett. **39**, 5224–7 (2014).

Towards nano-scale imaging with soft-X-ray coherence tomography*

S. Fuchs† [1,2], *M. Wünsche* [1,2], *S. Aull*[1], *J. Bernert*[1], *J. Biedermann*[1], *M. Möller*[1,2], *C. Rödel*[1,2], *and G.G. Paulus*[1,2]

[1]University, Jena, Germany; [2]Helmholtz Institute, Jena, Germany

Optical coherence tomography (OCT) is a well-established method to retrieve three-dimensional, cross-sectional images of biological samples in a non-invasive way using near-infrared radiation [1]. The axial resolution of OCT with broadband visible and near-infrared sources typically reaches axial (depth) resolutions in the order of a few micrometers. We developed soft-X-ray coherence tomography (XCT), which takes advantage of the fact that the coherence length can be significantly reduced if broadband extreme UV (XUV) and soft X-ray (SXR) radiation is used. XCT can display its full capabilities when used in the spectral transmission windows of the sample materials. For instance, the silicon transmission window (30-99 eV) corresponds to a coherence length of about 12 nm, thus suggesting applications for semiconductor inspection. In the water window at 280-530 eV, a coherence length as short as 3 nm can be achieved and highlights possible applications of XCT for life sciences.

Our setup utilizes a variant of a Fourier-domain OCT setup that completely avoids a beamsplitter [2,3]. Broadband XUV light is focused on the surface of the sample. The reflected spectrum is measured either with a grating spectrometer, consisting of a gold transmission grating and a toroidal mirror (spectrometer-based OCT) [4], or with a photo diode (swept-source OCT) and a tunable source. The top layer reflection assumes the role of a reference beam. A Fourier transform including dispersion correction of the reflected spectrum needs to be computed for retrieving the structural information. A 3D-image can be captured by scanning the focus over the sample. A proof-of-principle experiment has been performed at synchrotron sources successfully.

Since XCT exploits the spectral broadness of the light source to achieve axial resolution it can be regarded as a perfect application for laser-driven high-harmonic generation sources due to their intrinsic broad bandwidths. In fact, the bandwidth of HHG would have disadvantages for other imaging methods such as confocal microscopy or coherent diffraction imaging. In addition, HHG enables XCT to become a table top nanometer imaging technique. Thus we developed a suitable HHG source in the energy range of the silicon transmission window (30-99eV) with sufficient flux by using laser pulses with an energy of 1.8mW, a pulse duration of 50fs, and a wavelength of 1300nm driven by an OPA. In XCT, the depth information is contained in spectral modulations of the reflected light. Thus, the harmonic structure of HHG with multi-cycle laser pulses superimposes and therefore weakens the modulations of the XCT signal. Hence, it is necessary to flatten the HHG spectrum. Therefore we used the ability of the OPA to shift the wavelength of the driving laser rather quickly. We changed the driving laser wavelength during a single CCD exposure time in such a way that the HHG structure in the time-averaged spectrum on the CCD almost vanished (from 1250nm to 1310nm). Figure 1 shows the difference between harmonic spectra with and without shifting the wavelength. In 2015 we will use this XUV source to drive XCT.

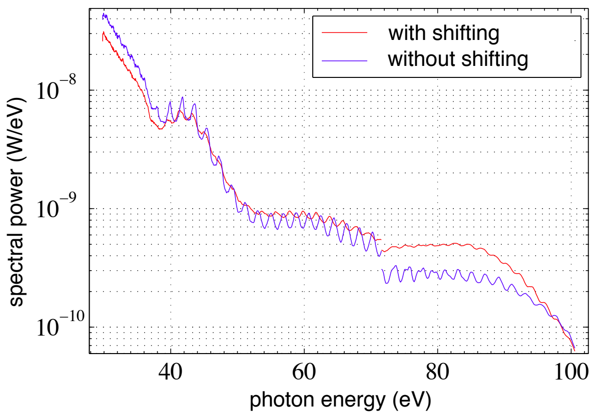

Figure 1: Harmonic spectra in Argon: The blue line shows a spectrum without modulation of the driving wavelength thus the harmonic structure is clearly visible. The red line shows an avaraged harmonic spectrum by sweeping the driving wavelength and the harmonic structure vanishes. The jump at 71eV is due to a change of filters.

References

[1] Huang, D. *et al.*, "Optical coherence tomography", Science 254, p. 1178 (1991)

[2] Fuchs, S. *et al.*, "Optical coherence tomography using broad-bandwidth XUV and soft X-ray radiation", Appl. Phys. B 106, p. 789-795 (2012)

[3] Paulus G. G. and Rödel, C. , "Short-wavelength coherence tomography", U.S. Patent US 7,656,538 B2 (2010)

[4] Fuchs, S. *et al.* , "Sensitivity calibration of an imaging extreme ultraviolet spectrometer-detector system for determining the efficiency of broadband extreme ultraviolet sources", Rev. Sci. Instrum. 84, p. 23101 (2013)

* Work supported by BMBF VIP-Project "X-CoherenT", HI Jena, and DFG TR18 A7

† silvio.fuchs@uni-jena.de

XUV Coherent Diffraction Imaging at the Abbe Limit

M. Zuerch[*1], *J. Rothhardt*[2,3], *S. Haedrich*[2,3], *S. Demmler*[2], *M. Krebs*[2], *J. Limpert*[2,3], *A. Tuennermann*[2,3,4], *A. Guggenmos*[5,6], *U. Kleineberg*[5,6], *and C. Spielmann*[1,3]

[1]IOQ, FSU Jena, Germany; [2]IAP, FSU Jena, Germany; [3]HI Jena, Germany; [4]Fraunhofer IOF, Jena, Germany; [5]LMU Munich, Garching, Germany; [6]MPQ, Garching, Germany

FELs and synchrotrons are used since a decade as sources to provide insight into matter and dynamics at the nanoscale. The key requirements for imaging at the nanoscale are: i) a short illumination wavelength, ii) a high photon flux, and iii) a narrow bandwidth. High Harmonic Generation sources are a promising alternative and were successfully used for coherent diffraction imaging (CDI) before [1]. Typically Ti:Sa laser driven HHG sources feature a high relative bandwidth ($\triangle\lambda/\lambda \sim 3 \times 10^{-2}$) and thus prevent CDI at the Abbe limit by violating condition iii).

To overcome this limitation we used a XUV source based on a high repetition rate fiber CPA system (λ = 1030 nm, f_{rep} = 100 kHz, E_p = 250 μJ, P_{avg} = 25 W) with subsequent nonlinear compression in a noble gas filled hollow core fiber [2]. The long pulse duration of $\tau \sim 60$ fs causes harmonic lines having a small relative bandwidth of $\triangle\lambda_{\text{FWHM}}/\lambda = 5 \times 10^{-3}$. Hence, requirement iii) is fulfilled much better. The CDI setup (Fig. 1a) contains specially designed XUV mirrors for selecting a single narrow-bandwidth harmonic line (31st harmonic @ 37.3 eV or 33.2 nm) out of the harmonic frequency comb. Two curved XUV mirrors are used to enhance the spectral selectivity, while the first mirror collimates the XUV beam and the second focuses it down onto the sample. The focal spot size was determined to $d \sim 5\,\mu$m (FWHM).

Using this setup, we recently achieved a spatial resolution down to 26 nm, which corresponds to 0.8λ [3]. A typical measured diffraction pattern is depicted in Fig. 1b. The object we used was our institute's logo milled into a gold coated silicon nitride membrane. Spatial features of this object are as tiny as 30 nm. The coherent fringes measured by illuminating this object with the 33.2 nm radiation extend well to the edge of the detector corresponding to a numerical aperture of 0.8. The reconstruction of the image (Fig. 1c), which is done by retrieving the phase from the diffraction pattern using established algorithms, features our institute's logo in great detail. Accordingly, we managed to perform the first demonstration of sub-wavelength imaging in the extreme ultraviolet, which is true for any source type including FELs and synchrotrons.

Moreover, we performed a measurement series using very short integration times in the order of a second. In that case, we could still achieve a reasonable reconstruction of our object down to a resolution below 80 nm. Full details on our results can be found in [3].

Further scalability of the FCPA system may soon allow to reduce the integration time further and/or achieve a higher resolution at current integration times. Moreover, scaling towards shorter wavelengths and thus towards biologically interesting absorption edges seems possible. This technique and the combination of competences within the HIJ might thus soon allow for real-time imaging of arbitrary objects at the nanoscale.

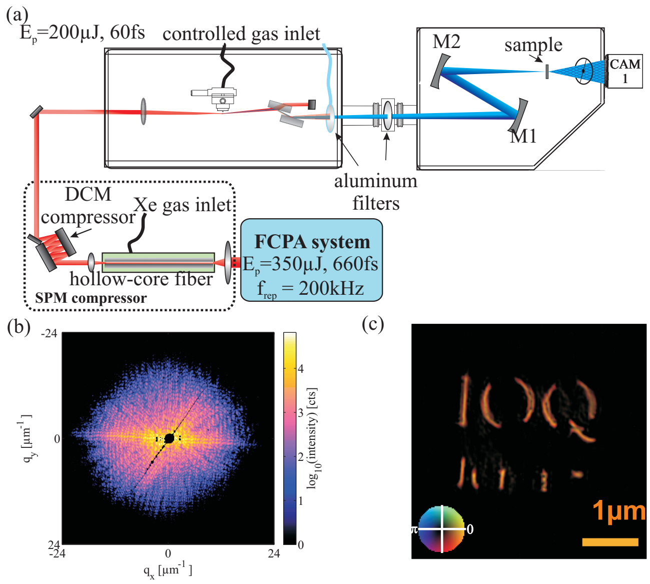

Figure 1: (a) Scheme of the experimental setup (see text for details). (b) Typical measured diffraction pattern at a high numerical aperture. (c) Reconstruction of the object featuring the institutes log. The achieved resolution is around 26 nm.

References

[1] J. Rothhardt, et al., "1 MHz repetition rate hollow fiber pulse compression to sub-100-fs duration at 100 W average power", Opt. Lett. 36 (2011), pp. 4605-4607

[2] M. Zuerch, C. Kern, and C. Spielmann, "XUV coherent diffraction imaging in reflection geometry with low numerical aperture", Opt. Express 21 (2013), pp. 21131-21147

[3] M. Zuerch, J. Rothhardt, et al., "Real-time and Subwavelength Ultrafast Coherent Diffraction Imaging in the Extreme Ultraviolet", Sci. Rep. 4 (2014), 7356

* michael.zuerch@uni-jena.de

Momentum resolved study of the saturation intensity in multiple ionization

P. Wustelt[1,2]*, M.Möller*[1,2]*, T. Rathje*[1,2]*, A.M. Sayler*[1,2]*, S. Trotsenko*[1]*, T. Stöhlker*[1,2]*, and G.G. Paulus*[1,2]
[1]Helmholtz Institute Jena, Germany; [2]Institute of Optics and Quantum Electronics, Jena, Germany

Strong-field ionization of atoms is of fundamental interest for many phenomena like laser-based electron or ion acceleration by ultra-intense laser pulses. When atoms are exposed to super-intensive or relativistic laser intensities, they will be ionized to high charge states. In the optical regime, the ionization probability depends highly nonlinear on the field strength. Therefore, for a pulsed field, ionization is concentrated in a narrow intensity and a correspondingly narrow time interval for each ionization step. This intensity where ionization peaks is named saturation intensity. An accurate determination of the saturation intensity for atomic ionization in intense femtosecond laser field plays an important role in appropriate modeling of not only strong-field laser matter interaction. In particular, in Plasma physics, accurate modeling of ionization dynamics over a large range of charge states, e.g. predictions for the time dependent charge density or the ionization injection in plasma waves, is essential.

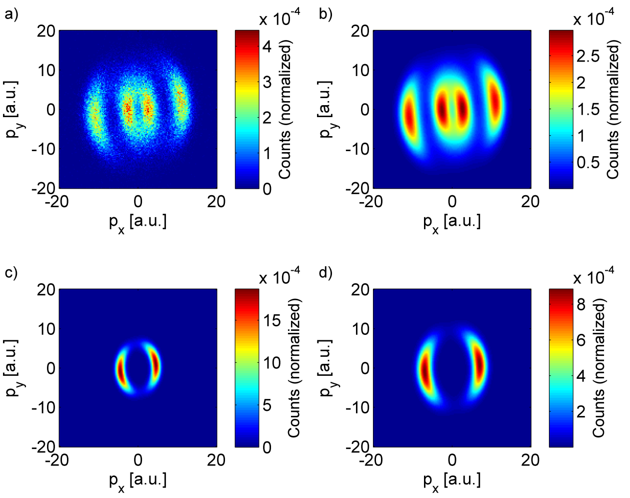

Figure 1: a) Measured ion momentum distribution of Ne^{3+}, b) Simulated momentum distribution for Double ionization from fit method, Simulated momentum distribution for first (c) and second (d) single ionization from fit method.

Experimentally, the recently developed ion beam apparatus is used together with a high-power high-repetition rate laser system that delivers 10-mJ, 35-fs laser pulses. The ion beam is produced by a duoplasmatron ion source or an EBIT (electron beam ion trap). In order to produce a dense and collimated beam at the interaction point with the laser, the ion beam is accelerated to several keV and guided through a series of Einzel lenses, a Wien filter, deflectors and pinholes. After the laser matter interaction, the full three dimensional momentum distribution of the resulting fragments are measured with a position- and time-sensitive detector.

Status of the project: The momentum and charge state distributions of ions resulting from the ionization of singly charged Xenon, Neon and Helium are studied as a function of intensity and ellipticity of the laser pulses. Peak intensities up to $6{\cdot}10^{16}$ W/cm^2 allow the observation of highly charged ions up to Xe^{8+}, Ne^{5+} and He^{2+}. A method to deconvolve the measured momentum distribution of multiply ionized ions and extract the saturation intensities from the ion momenta for each single ionization step in the multiple sequential ionization process was developed (see Fig.1). Thereby, removing the typically large experimental uncertainties in the intensity determination, this allows the retrieval of averaged ionization times of all charge states created in the laser focus [1]. The measured results are compared with predictions of the frequently used models of over-the-barrier ionization and modeling the ionization by quasistatic tunneling ionization rates based on the theory of Ammosov, Delone and Krainov (ADK) (see Fig.2). Due to the dependence of the ionization rate on the absolute value of the m quantum number, the simulation results in a broad range of possible momenta, which includes the results of the measurement.

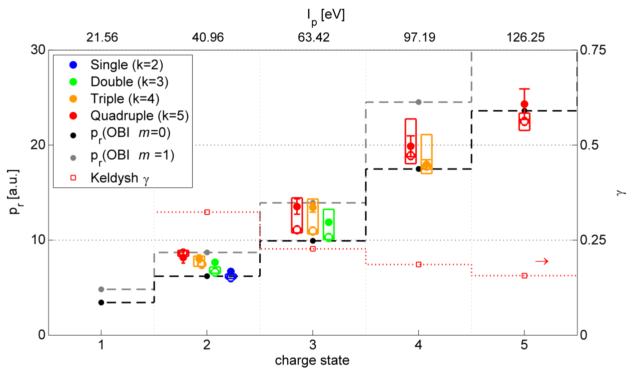

Figure 2: Comparison of the measured final momentum (solid circles) with results of calculations of the ionization rate (open circles and rectangles). The red open squares (right scale) represent the trend of Keldysh parameter.

References

[1] P. Wustelt, M. Möller, T. Rathje, A. M. Sayler, T. Stöhlker, and G. G. Paulus, *Phys. Rev. A* **91**, 031401(R) (2015)

HILITE – trapped ions in intense photon fields

S. Ringleb[1], M. Vogel[2], S. Kumar[3], W. Quint[2,4] G.G. Paulus[1,5], Th.Stöhlker[1,3,5]

[1] Institut für Optik und Quantenelektronik, Friedrich-Schiller-Universität, 07743 Jena, Germany
[2] GSI Helmholtzzentrum für Schwerionenforschung GmbH, 64291 Darmstadt, Germany
[3] Inter-University Accelerator Centre, 110067 New Delhi, India
[4] Physikalisches Institut, Ruprecht Karls-Universität Heidelberg, 69120 Heidelberg, Germany
[5] Helmholtz-Institut Jena, Fröbelstieg 3, 07743 Jena, Germany

Recent experiments on laser-ionization of atoms [1] made it necessary to use an ion storage tool to provide well defined ion target to investigate ionization dynamics of field-ionization and multiphoton ionization. Due to its strong trapping force we decided to build a Penning trap for experiments with ions and intense laser radiation [2].

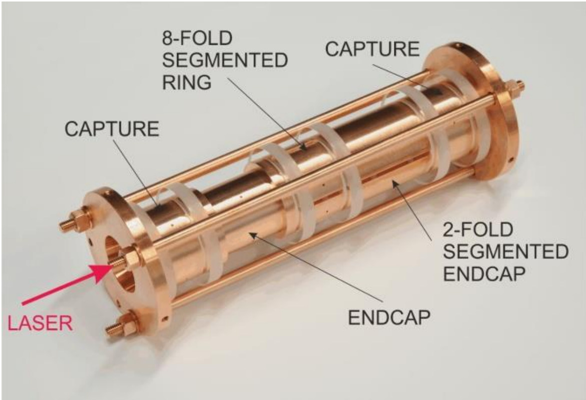

Figure 1: Photograph of the Penning trap.

The Penning trap is designed to support the preparation of well defined ion targets concerning ion shape, ion species and charge state with the Rotation Wall mechanism [3]. Using this confinement technique we will can compress an ion cloud to about $10^9\,cm^{-3}$. Applying resistive and sympathetic in-trap ion-cooling technologies[4] we will cool down the ions to cryogenic temperatures to assure a good confinement of the ion cloud. Using the FT-ICR method the Penning trap also will be used to measure the stored number of particles precisely for every single charge state non-destructively and simultaneously before and after laser interaction. Therefore we will be able to measure ionization cross sections of all ionization channels to achieve a better knowledge of ionization mechanisms. The non-destructive measurement techniques will be gauged before by destructive detectors such as multichannel plates. Due to the well defined target we plan to use the ion target as a probe to determine the shape of the laser pulse. So we can determine the shape of the laser-focus in situ.

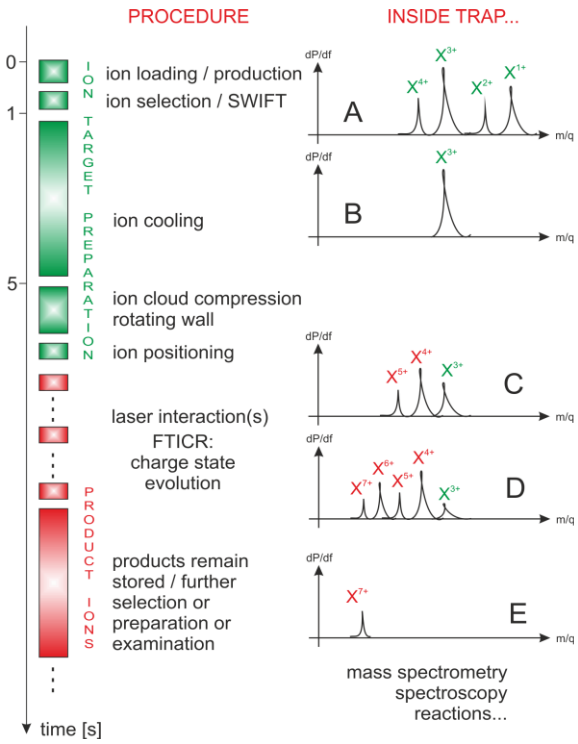

Figure 2: Experimental timing scheme.

The whole setup is designed in a flexible fashion and can therefore be transferred easily to different laser-facilities such as Phelix, Polaris, Jeti and Flash. So we will cover a large spectrum of ionization parameters.

References

[1] Richter, M. et al. 2009. Extreme Ultraviolet Laser Excites Atomic Giant Resonance. *Physical Review Letters*, 102(16), S.163002.

[2] Vogel, M. et al., 2012. A Penning trap for advanced studies with particles in extreme laser fields. *Nuclear Instruments and Methods in Physics Research Section B: Beam Interactions with Materials and Atoms*, 285, S.65–71.

[3] Bharadia, S. et al., 2012. Dynamics of laser-cooled Ca+ ions in a Penning trap with a rotating wall. *Applied Physics B*, 107(4), S.1105–1115.

[4] Vogel, M. et al., 2014. Resistive and sympathetic cooling of highly-charged-ion clouds in a Penning trap. *Physical Review A*, 90(4), S.043

Development of ion detectors for the 1–10 MeV/u energy range*

C. Hahn[†1,2], *A. Bräuning-Demian*[3], *A. Gumberidze*[3], *E. Lamour*[4], *J. Rangama*[5], *Th. Stöhlker*[1,2,3], *D. Vernhet*[4], *G. Weber*[1,3], *and the Fit-FISIC collaboration*[2,3,4,5]

[1]Helmholtz Institute Jena, Germany; [2]FSU, Jena, Germany; [3]GSI, Darmstadt, Germany; [4]INSP, Paris, France; [5]CIMAP, Caen, France

Physics case

Within the universe, matter is commonly found in the state of ionized plasma, where collisions between ions occur regularly. The interaction cross sections of the involved charge-exchange processes are largest in the so-called *intermediate regime*, where the electron and relative target–projectile speed are comparable. For a proton colliding with a hydrogen atom, this regime corresponds to an energy of about $10\,\mathrm{keV}$; heavier ions require some $10\,\mathrm{MeV}$. Unfortunately, it is difficult to calculate the relevant cross sections theoretically, as the rigorous electronic treatment of the system amounts to an N-body problem. On the other hand, experimental investigations are hampered by the fact that the probabilities of a variety of interaction mechanisms attain similar magnitudes, which causes "interference effects". Therefore the intermediate collision regime, despite its undeniable importance, is only barely investigated, with experimental data lacking for all but the lightest systems.

The Franco-German *Fit-FISIC* cooperation ("**Fi**rst steps **t**owards atomic physics of **F**ast **I**on–**S**low **I**on **C**ollisions") constitutes a novel attempt to better understand these ion–ion interactions. Using intense high-quality ion beams that are available at French and German accelerator facilities such as SPIRAL2 and FAIR (currently under construction at Caen and Darmstadt, respectively), collisions of multi-charged ions will be realized under well-controlled conditions [1]. The planned setup is outlined in Figure 1.

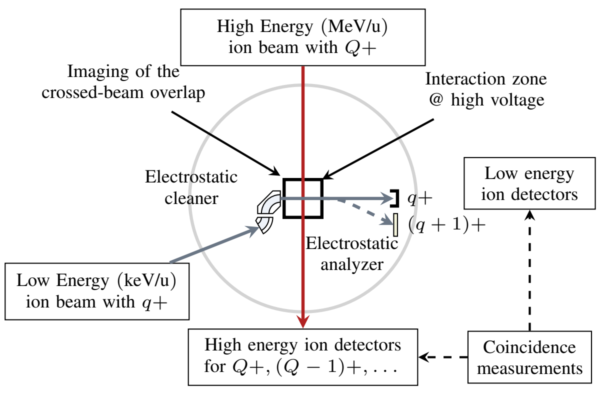

Figure 1: Planned setup for the Fit-FISIC project. Coincidence measurements of the low- and high-energy branches will be used to detect charge-exchange reactions. Figure reproduced from [1]

Ion detector development

As a collaborative effort of both GSI and FSU, a detection system for the high-energy branch of the project is currently being developed. This detector will have to cope with MHz count rates of ions having energies between sub-$\mathrm{MeV/u}$ and $15\,\mathrm{MeV/u}$, while remaining windowless so as to not stop impinging ions before they reach the actual sensor material. A movable stage will position the detector relative to the beam of charge-exchanged ions. Since the projected energy and ion range are only scarcely investigated with respect to suitable detector models, extensive research into possible sensor configurations is necessary.

Above all else, radiation hardness is a critical demand: charged particles deposit their energy locally, evident in the so-called *Bragg peak* of the energy loss curve, leading to conventional semiconductor and plastic scintillator detectors being virtually "scorched" by the incident ion flux, which renders them unusable almost immediately.

A favorable material choice for these conditions is artificial diamond, one of the most resilient materials around. CVD diamond also offers a desirably high charge carrier mobility [2], although it is somewhat diminished by grain boundaries present in polycrystalline substrates. Its behavior under prolonged ion bombardment, most notably the long-term signal stability, will be studied in 2015 at tandem accelerators capable of delivering the required ion species and energies.

In parallel, alternative detector models are being considered. Among these, scintillator crystals such as cerium-doped yttrium aluminum perovskite (YAP:Ce) appear particularly promising. The material has been successfully employed to detect ions in earlier experiments, where it exhibited a surprising level of radiation hardness [3]. A test setup to investigate the feasibility of these alternative approaches is currently being assembled at Helmholtz Institute Jena, and will be used for initial measurements in 2015.

References

[1] Fit-FISIC Collaboration, ed., "Project Fit-FISIC: Scientific Document" (2013)

[2] G. Kramberger et al., "Radiation damage in diamond detectors", Vertex 2012 (2012)

[3] M. Tokman et al., "Towards a Determination of QED Effects in Cu-Like Pb Recombination Resonances Near Threshold", Phys. Scripta 2001 (2001) 406

* We acknowledge support by the DFG under grant no. STO 346/4-1.

† christoph.hahn@uni-jena.de

S-EBIT at HITRAP: Status Report

S. Trotsenko[1,2], W. Chen[2], J. Menssen[1,2,3], G. Vorobjev[2], D. Racano[2], A. Gumberidze[2,4], C. Kozhuharov[2], O. Forstner[5], P.-M. Hillenbrand[2], F. Herfurth[2], R. Schuch[6], and Th. Stöhlker[1,2,4,5]

[1]Helmholtz-Institut Jena, D-07743 Jena, Germany; [2]GSI Helmholtzzentrum für Schwerionenforschung, D-64291 Darmstadt, Germany; [3]Hochschule Rhein Main, University of Applied Sciences, D-65428 Rüsselsheim, Germany; [4]ExtreMe Matter Institute EMMI, D-64291 Darmstadt, Germany; [6]Friedrich-Schiller-Universität Jena, D-07743 Jena, Germany; [5]Department of Physics, Stockholm University, SE-10691 Stockholm, Sweden

The Super-EBIT (S-EBIT) [1] plays an important role for accomplishing the mission of Helmholtz Institute Jena (HI-Jena) towards Facility for Antiproton and Ion Research (FAIR). It considerably expands the opportunities for developing new technologies and procedures for novel experiments with highly charged ions (HCI). In the S-EBIT program of HI-Jena the emphasis is put on X-ray spectroscopy and the interaction of intense laser radiation with HCI, including the respective diagnostics. The project will open up further points of contact, e.g. in the fields of X-ray wavelength standards, astrophysics, and material sciences. The S-EBIT will contribute substantially to the research program at GSI/FAIR as well as to the required R&D activities such as the development of x-ray spectrometers, calorimeter detectors, x-ray optics, and traps for the interaction of intense laser light with highly charged ions. Moreover, the S-EBIT program of Helmholtz Institute Jena is of substantial importance for bridging the gap of the transition time for heavy ion experiments between GSI and FAIR. In particular, as an operating source of highly charged ions during the shutdown period of the GSI accelerator, the S-EBIT will facilitate research and development works indispensable for SPARC experiments at FAIR. Within this decade the new laboratory building at the HI-Jena is expected to be available. This will allow moving the S-EBIT installation from GSI to the HI-Jena where it can be coupled to the available unique laser infrastructure where intense laser pulses with high repetition rate are provided (JETI200, POLARIS). Still, S-EBIT will serve also as an R&D facility for FAIR both in combinations with the intense laser pulses but also as a standalone device.

Currently, the S-EBIT is being installed at the experiment platform of the HITRAP facility [2] at GSI and it will be used not only as a standalone device but also as an ion source for highly charged heavy ions. At the experiment platform, various experimental setups have already been installed and are available for operation such as traps for QED experiments, surface experiments, gas target stations, and recoil ion spectrometers. The HITRAP decelerator is currently getting commissioned and is not yet operational [2] and in particular also first experiments with highly-charged ions in intense laser fields can be anticipated (PHELIX) at the HITRAP location [3].

A brand new transportable frame for the S-EBIT has been manufactured which will allow one to move the source towards experimental installations in order to be able to combine with the already available and planned experiments [2]. Preparations of the new superconducting magnet (4T) have been finalized and it is now being tested for the performance in the new S-EBIT environment. In a superconducting Helmholtz coils configuration of the S-EBIT a special attention has to be paid to efficient cooling of the magnet as it has to perform with the currents of higher than 60 A. In order optimize that the new shielding and cooling parts have being manufactured which are currently undergoing their first cryogenic tests. Also, brand new drift tubes to fit the new 4T-superconducting magnet have been manufactured, which along with the optimized S-EBIT chamber feedthru system will allow a reliable fast ramping of the drift tubes potentials at up to +40 kV. In combination with the -220kV on the e-gun/collector terminal the electron beam energy of 260 keV can potentially be reached. In addition, the work on integrating the S-EBIT control system into the GSI/HITRAP infrastructure is on going.

References

[1] R.Schuch et al., JINST5, C12018 (2010)
[2] Z.Andelkovic et al., GSI Scientific Report 2013 (2014).
[3] M. Vogel, W. Quint, G.G. Paulus and Th. Stöhlker, Nucl. Instr. Meth. B 285, 65 (2012).

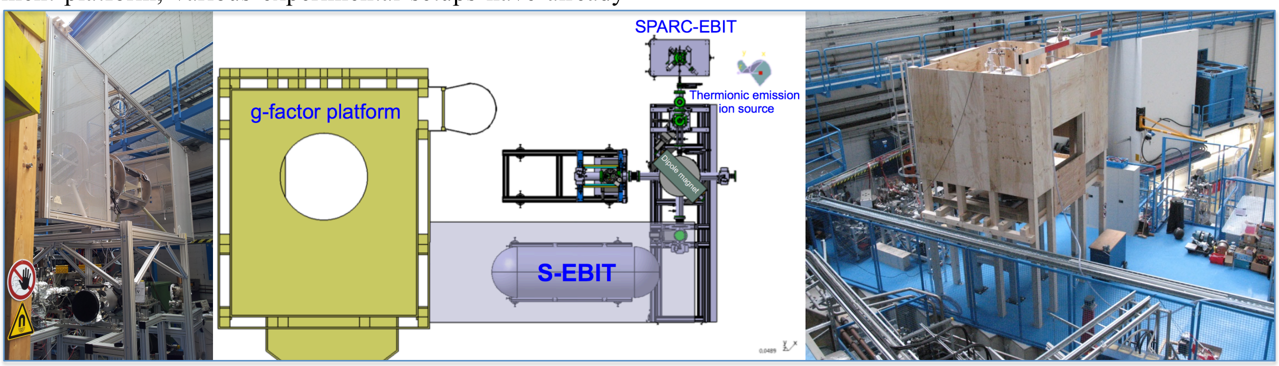

The status of the CRYRING@ESR project*

F. Herfurth[† 1], *M. Lestinsky*[1], *Z. Andelkovic*[1], *R. Bär*[1], *A. Bräuning-Demian*[1], *S. Litvinov*[1], *O. Dolinskii*[1], *W. Enders*[1], *M. Engström*[1], *S. Fedotova*[1], *B. Franzke*[1], *W. Geithner*[1], *O. Gorda*[1], *A. Källberg*[2], *N. Kotovskiy*[1], *A. Reiter*[1], *A. Simonsson*[2], *T. Sieber*[1], *J. Sjöholm*[2], *M. Steck*[1], *Th. Stöhlker*[1,3], *and G. Vorobjev*[1]

[1]GSI, Darmstadt, Germany; [2]MSL, Stockholm University, Stockholm, Sweden; [3]HIJ, Jena, Germany

The low energy storage ring LSR [1] shall provide highly charged ions and antiprotons at low energy for two collaborations at FAIR, SPARC and FLAIR. Those collaborations intend to perform precision experiments pursuing atomic and nuclear physics questions [3]. The LSR is a Swedish in-kind contribution to the FAIR facility in Darmstadt.

The LSR is the swedisch low energy storage ring CRYRING modernized and adapted to the additional needs for injection and ejection of antiprotons and highly charged ions at about 10 MeV/nucleon. CRYRING has been operated at the Manne Siegbahn Laboratory in Stockholm until 2010, was dismantled in 2012 and transported to GSI in the first months of 2013. At GSI it will be installed behind the ESR, as proposed and described in detail in 2012 by a swedish-german working group [2]. This proposal has been accepted end of 2012 by the relevant committees.

CRYRING can decelerate, cool and store heavy, highly charged ions and anti protons injected at about 10 MeV/nucleon down to a few 100 keV/nucleon. It provides a high performance electron cooler and a straight section for flexible experiment installations as for instance a gas jet target. It is equipped with it's own injector and ion source, to allow for standalone commissioning.

In 2014 the design and installation of infrastructure into the newly constructed Cave B included media supplies like cooling water or compressed air, power cabling, magnet cabling, water cooled cabling, signal cabling. The cable routing and cable tray planning and installation has almost been completed. For electrical supply a new low voltage distribution has been conceived and purchased. The integration into the GSI safety systems is ongoing and well advanced. For this the lock and gate system has been reinstalled to ensure controlled access to the cave.

One prerequisite for the physics part of the CRYRING@ESR project, the transport and injection of heavy, highly charged ions from the ESR, has been advanced. The beam line has been modified and setup in large parts. Furthermore, part of the beam time was used to test the extraction and transport of ESR beam. It has been shown successfully that even close to the lower limit of ESR operation, at 4 MeV/u beam energy, it was possible to extract ions towards CRYRING in Cave B and to transport it beyond the first three dipoles.

Figure 1: Photograph of the situation in the CRYRING cave end of 2014. In the foreground the local injector has been setup and is being aligned. In the background visible is the ring structure with its dipoles and the magnetic sections with quadrupole and sextupole magnets.

The local injector has been mechanically put in place. First pumping down tests of the RFQ were conducted successfully. The required pressure has been reached, showing that the RFQ is ready to be operated after all the refurbishing to update for instance it's cooling circuit.

Setting up of the first components of the ring has begun, i.e. all ring dipoles were installed and the GSI technical divisions are completing inspection and preparation of the subsystems installed in the straight sections.

The Electron cooler has been worked at to repair transport damages and to check primarily the vacuum conditions. A testing stand for cryogenic tests is under preparation.

References

[1] H. Danared, et al. (2011) “LSR - Low-energy Storage Ring, Technical design report”, Manne-Siegbahn Laboratory, Stockholm University, version 1.3.

[2] M. Lestinsky, et al. (2012) “CRYRING@ESR: A study group report”, Project study, GSI, Darmstadt,

[3] M. Lestinsky, et al. (2014), “CRYRING@ESR: Present Status and Future Research”, Proceedings of the STORI 2014, 9th International Conference on Nuclear Physics at Storage Rings, Sankt Goar, Germany.

* Work supported by GSI/HI Jena/FAIR@GSI PSP code:1.3.4.2./The SPARC collaboration/Uni Krakov/KVI Groningen

† F.Herfurth@gsi.de

SPARC Experiments at the HESR*

Thomas Stöhlker† [1,2,3], *Yuri A Litvinov*‡ [1,4], *and the SPARC Collaboration***
[1]GSI, Darmstadt; [2]HI Jena; [3]Uni Jena; [4]Uni Heidelberg;
**https://www.gsi.de/work/forschung/appapni/atomphysik/forschung/ap_und_fair/sparc

SPARC experiments at the High Energy Storage Ring (HESR) [1] were approved to be within the Modularized Start Version (MSV) of the future FAIR project. The HESR was primarily designed for experiments with stored and cooled anti-protons. However, a careful investigation of the ring parameters (injection, cooling, stacking, available place for equipment, beam emittance, ion optics, radiation safety, etc.) revealed a promising result that the ring is well-suited for operation with heavy ions without any significant ring modifications [2]. Stored and cooled beams at relativistic energies with γ-values ranging from 2 to 6 will be available. Such experimental conditions do presently not exist anywhere else in the world. SPARC experiments will focus on investigations of collision dynamics in strong electro-magnetic fields and fundamental interactions between electrons and heavy nuclei up to bare uranium.

Ion-optical simulations have shown that the "missing-dipole" locations in the HESR lattice are well suited to accommodate the SPARC internal target stations and the corresponding detector equipment. Two places are foreseen in the HESR, see Figure 1. For one position, the electron cooler is located upstream the target, which might pose a problem due to ion recombination with electrons in the cooler as well as the rest gas of the long straight section. Such recombination products can cause unwanted background. However, this location offers the highest spacial resolution for charge-exchange reaction products in the target [4].

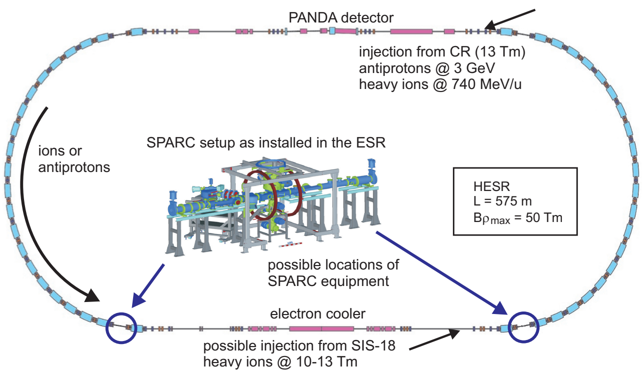

Figure 1: The High-Energy Storage Ring HESR [1]. The main parameters of the HESR are indicated as well as the locations of the PANDA and SPARC experiments. A scheme of the SPARC setup as it is presently constructed in the ESR is shown the insert [3].

The second location is proposed upstream the electron-cooler straight section. This location offers a somewhat lower spacial resolution but has a clear advantage that background due to recombination reaction products is not present. For more details the reader is referred to [4].

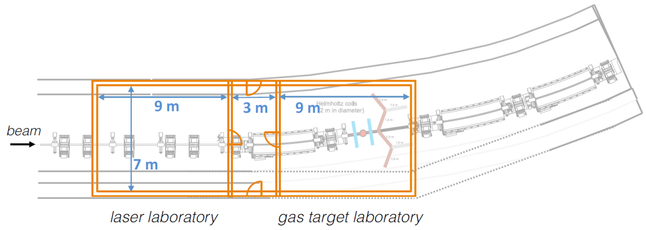

Figure 2: Schematic view of an infrastructure laboratory building on top of the HESR tunnel. The two laboratories, each about 7x9 m, need to be fully climatized.

Since the SPARC Experiments were not foreseen at the HESR from the beginning of the building planning, several modifications of the building are necessary to accommodate the SPARC infrastructure. Especially important are the parts which require access during the running of the HESR and have thus to be placed outside the radiation protection areas.

The HESR tunnel is foreseen to be surrounded by 1 m of concrete and an additional earth packet of about 3 m in thickness. Figure 2 shows a suggestion for a laboratory building on top of the tunnel in the south-east section of the HESR. The same building is also planned in the south-west section. The laboratory buildings will accommodate primarily the infrastructure for the gas-jet and laser experiments. However, also experiment electronics for various experiments can be located there. According to the dedicated beam transport calculations, the holes of 20 cm in diameter from the laboratory to the tunnel will pose no additional restrictions from the radiation protection side.

A proposed in [3] direct connection of the SIS-18 and the HESR would enable SPARC@HESR already at a very early stage of FAIR.

References

[1] R. Maier, Proc. PAC 2011, New York, p. 1 (2011).
[2] T. Stöhlker *et al* 2011*SPARC Experiments at the HESR: A Feasibility Study*.
[3] T. Stöhlker *et al* 2014 *Hyp. Interact.* **227** 45–53
[4] O. Kovalenko *et al.* 2015 *Phys. Scripta T* in press.

* Work supported by HI Jena, FZ Jülich, and Helmholtz-CAS Joint Research Group HCJRG-108.
† t.stoehlker@gsi.de
‡ y.litvinov@gsi.de

Improved accuracy of in-ring Laser spectroscopy by in-situ electron cooler voltage measurement*

Johannes Ullmann[1,2] *and the LIBELLE collaboration*

[1]Institut für Kernphysik, Technische Universität Darmstadt, Germany; [2]Helmholtz Institute Jena, Jena, Germany

Introduction

Laser spectroscopy experiments of highly charged, heavy ions at the experimental storage ring ESR have been performed for more than twenty years by now [1, 2, 3], aiming at tests of fundamental theories. A conclusive test of bound-state quantum electrodynamics (BS-QED) in strong fields, however, has not been reached so far, because of the large uncertainty arising from the unknown spatial distribution of the nuclear magnetization (Bohr-Weisskopf effect). The method formulated by Shabaev and coworkers [4], defining a specific difference between the hyperfine splittings in hydrogen- and lithium-like ions of the same species removes these uncertainties and provides the possibility to test BS-QED without nuclear uncertainties. Although the attempt in 2011 to measure the hyperfine splitting energies of the ground states in hydrogen- and lithium-like bismuth ions was for the first time successful in detecting both resonances, it yielded a large uncertainty caused by an inaccurate knowledge of the ion velocity [5]. Hence, a second attempt was performed in March 2014 with an improved setup.

Setup

The setup was similar to previous experiment in 2011 and is shown in fig. 1. Ions injected into the ESR were cooled with the electron cooler and confined into two bunches using a radio frequency (RF)-cavity, driven with the second harmonic of the revolution frequency. With a bunched beam, the fluorescence signal-to-background ratio could be improved by 50% compared to coasting beam operation. The bunching frequency was used for tagging the arrival times of single photon counts on the photomultiplier tubes by the data acquisition system with 3.3-ns resolution. This was realized using time-to-digital converters implemented on a VUPROM-device[1]. The fluorescence light detection efficiency was optimized in the two cases using two mirror systems adapted to the specific needs of the respective transition and shown on the right side of 1: For the hydrogen-like ions the detection chamber developed for [2] (upper part) and for the lithium-like species the system developed at the University of Münster [6] were used. The excitation of the hyperfine transition was performed by a dye laser system consisting of a Nd:YAG pump laser and a Sirah COBRA dye-laser that provided pulses with energies of 150 mJ. The target laboratory frame wavelengths of 591 nm and 641 nm were produced by Pyrromethene 597 dye and DCM Special dye, respectively, and the light was delivered to the ESR experimental hall using mirrors with a high-reflectivity coating.

A major improvement of the setup was the in situ measurement of the electron cooler voltage, which is used to determine the ions' velocity for Doppler shift compensation. The data analysis of the previous attempt in 2011 revealed that the calibration of the electron cooler voltage display was insufficient, leading to large uncertainties [7]. To circumvent this, an accurate high-voltage divider was installed. A newly established collaboration with the high-voltage metrology working group of PTB[2] enabled us to use a reference voltage divider featuring a relative accuracy of 10^{-5} [8]. An additional measurement of residual frequencies in the d.c. high voltage using a ripple probe developed at PTB revealed a very clean high voltage signal. Besides the anticipated leap in accuracy, the voltage measurement turned out to be a invaluable diagnostic tool. Energy fluctuations of the ion beam that emerged during beamtime could be identified to originate from a floating drift tube inside the electron cooler, and could be clearly distinguished from fluctuation of the high-voltage power supply that also arose during beamtime. The in-situ measurement allowed us to take all voltage fluctuations into account during the analysis.

First Results

The analysis of the fluorescence data was performed using GO4 and SciPy. A typical resonance for hydrogen-like bismuth recorded in one single scan of the laser wavelength with coasting ion beam is shown in the left part of fig. 2. The resonance wavelength in the laboratory frame was determined by fitting a Gaussian profile to the fluorescence data using the orthogonal distance regression algorithm [10] to take the uncertainty of the laser wavelength determination into account. Although the analysis is still ongoing, first results of the rest-frame wavelength of the ground state hyperfine transition in hydrogen-like bismuth could be obtained [9] demonstrating the advantage of the high-voltage measurements. The analysis of the resonances taken without bunching the ion beam ("coasting beam") resulted in a value roughly 10 times more accurate compared

* Work supported by HIC4FAIR, HGS-HIRe, BMBF contract Nos. 05P12PMFAE and 05P12RDFA4.

[1] **V**ME **U**niversal **Pro**cessing **M**odule, an FPGA-based module for VMEbus-systems developed at GSI's experiment electronics department

[2] Physikalisch Technische Bundesanstalt Braunschweig, the German national metrology institute

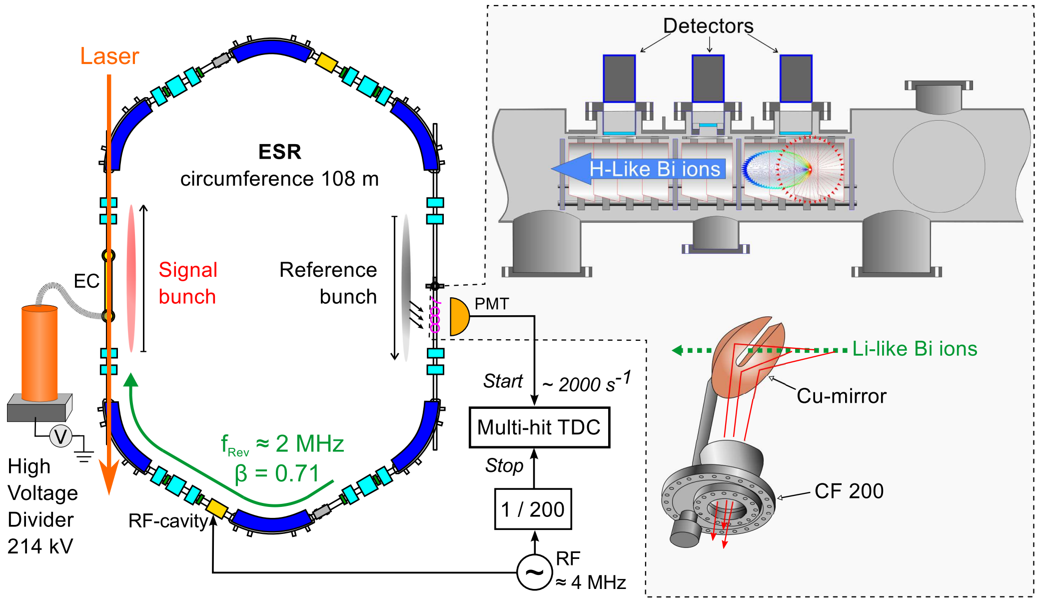

Figure 1: Experimental setup:The voltage of the electron cooler (EC) gun determines the ion velocity in the ESR and is measured with a precise high-voltage divider (HVDC2.1 from PTB). The upper part of the inset shows the detection section used for the hydrogen-like charge state which was reused from [2], the lower part shows the retractable parabolic mirror system [6] for detection of the forward cone-shaped emission characteristic of lithium-like bismuth. All photons detected at one of the two mirror systems are tagged on a VUPROM multi-hit TDC with an absolute time stamp as well as relative to the phase of the revolution frequency.

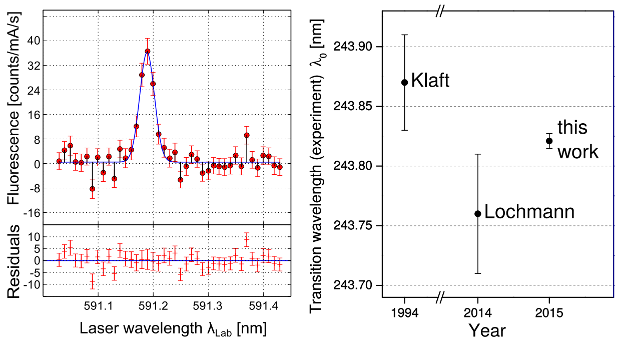

Figure 2: Left: Single resonance signal of hydrogen-like bismuth taken with a coasting ion beam. The fluorescence counts are normalized to ion current and live time of the data acquisition. A fit of a Gaussian profile and the corresponding residuals are also shown. Right: Result of the rest-frame wavelength of the ground state hyperfine transition in hydrogen-like bismuth, compared to previous attempts. The result is compatible with the prior values and its accuracy has been improved by a factor of 10 [9].

to the previous attempts, as shown in the right part of fig. 2.

Conclusion

According to the first results of the LIBELLE 2014 beam time, a QED test using the hyperfine splittings in bismuth ions is in reach now. The accuracy of the obtained hydrogen-like bismuth wavelength is an order of magnitude higher than in all previous attempts and promises a similar leap in accuracy for the lithium-like charge state and, consequently, also for the specific difference. Lifetime measurements for both transitions have been performed as well and are currently under evaluation at the University of Münster. Furthermore, it has been pointed out, that an accurate *in-situ* voltage measurement is vital for laser spectroscopic measurements at the ESR and a valuable diagnostic tool for other experiments using the electron cooler. Hence, a dedicated high voltage divider is currently commissioned and will soon be installed at the electron cooler.

References

[1] I. Klaft et al. *Phys. Rev. Lett.*, **73** (1994), 2425.

[2] P. Seelig et al. *Phys. Rev. Lett.*, **81** (1998), 4824.

[3] Winter. Dissertation, Universität Darmstadt (1999).

[4] V. M. Shabaev et al. *Phys. Rev. Lett.*, **86** (2001), 3959.

[5] M. Lochmann et al. *Phys. Rev. A*, **90** (2014), 030501. PRA.

[6] V. Hannen et al. *J. Instrum.*, **8** (2013), P09018.

[7] M. Lochmann. Ph.D. thesis, Johannes Gutenberg Universität Mainz (2013).

[8] J. Hallstrom et al. *IEEE Trans. Instrum. Meas.*, **63** (2014), 2264.

[9] J. Ullmann et al. *J. Phys. B: At. Mol. Opt. Phys.* (2015). Submitted.

[10] P. T. Boggs et al. *SIAM J. Sci. Comput.*, **8** (1987), 1052.

Beam current monitor based on a Cryogenic Current Comparator*

R. Geithner[1,2], *T. Stöhlker*[1,2,3], *R. Neubert*[4], *and P. Seidel*[4]

[1]Helmholtz Institute Jena, Germany; [2]Institute for Optics and Quantum Electronics, Friedrich Schiller University Jena, Germany; [3]GSI Helmholtzzentrum für Schwerionenforschung GmbH, Darmstadt, Germany; [4]Institute of Solid State Physics, Friedrich Schiller University Jena, Germany

A non-destructive beam monitoring system for particle beams in accelerators based on the Cryogenic Current Comparator (CCC) principle was recently developed [1] in a joint effort of Institute of Solid State Physics at FSU Jena and HI-Jena.

The CCC consists of a high-performance, low-temperature DC superconducting quantum interference device system (LTS-DC-SQUID), a superconducting toroidal pick-up coil, and an extremely effective meander-shaped superconducting niobium shield. This device allows the measurement of continuous as well as pulsed beam currents in the nA-range with a high time resolution. The resolution and the frequency response of the detector strongly depend on the toroidal pick-up coil and its embedded ferromagnetic core [2].

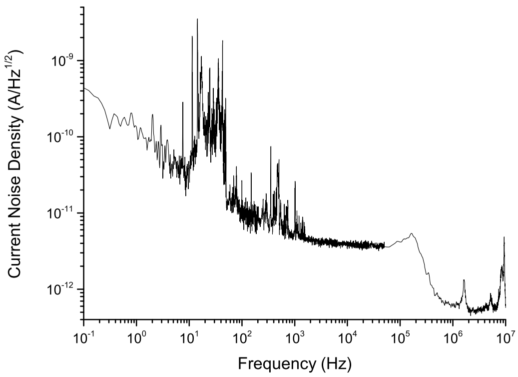

Figure 1: Current noise density of the improved CCC with Nanoperm M764 core, matching transformer and Supracon SQUID sensor CP2 blue. A Magnicon XXF-1 electronics was used.

The current noise of the CCC could be decreased by a factor of five compared to previous systems [3] and the bandwidth is increased to 200 kHz (see Fig. 1). This results from the usage of iron-based nanocrystalline Nanoperm as core material for the pick-up coil and state-of-the-art SQUID components. With this optimized CCC, a noise limited current resolution of 1 nA should be achievable in the experimental environment of an accelerator [3].

Figure 2 shows the response of the improved CCC to rectangular current signals applied to a beam simulating wire along the beam axis. There is no low pass filter or time-averaging used. The transfer function shows a high dynamic range with a linear behavior from 10 to 2000 nA (see inset in Fig. 2).

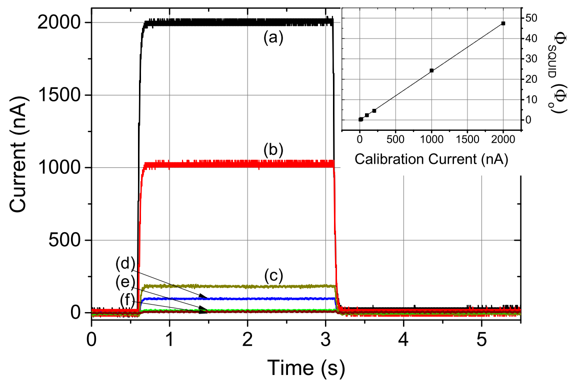

Figure 2: Response of the improved CCC to a rectangular current signal of 2 μA (a), 1 μA (b), 200 nA (c), 100 nA (d), 20 nA (e) and 10 nA (f) applied to a beam simulating wire along the beam axis. The inset shows the linear transfer function.

For the international FAIR project at Darmstadt it is foreseen to install several CCC detectors at the high-energy transport beam lines. Here, beam currents in the range between 10^{-4} and 10^{-2} mA are to be expected. In addition the installation of a CCC system at CRYRING is planned for highly accurate absolute current measurements at low beam energies and small particle numbers for ions as well as for antiprotons. In parallel to the tests at GSI/FAIR, the CCC will also be tested at the Antiproton Deceleration (AD) ring. The CERN low-energy antiproton physics experiments are currently served by the AD ring.

References

[1] Geithner R, Neubert R, Vodel W, Schwickert M, Reeg H, von Hahn R, Seidel P. “A Non-Destructive Beam Monitoring System Based on an LTS-SQUID”, IEEE Transactions on Applied Superconductivity, 21(3):444-447, 2011

[2] Geithner R, Heinert D, Neubert R, Vodel W, Seidel P, “Low temperature permeability and current noise of ferromagnetic pickup coils”, Cryogenics, 54:16-19, 2013

[3] Geithner R, Kurian F, Reeg H, Schwickert M, Neubert R, Seidel P, Stöhlker T. “A squid-based beam current monitor for FAIR / CRYRING”, accepted for publication by Physica Scripta, 2015

* Work supported by GSI (LOBI).

Interaction of ZnO nanostructured targets with intense laser pulses *

Z. Samsonova† [1,2], *R. Hollinger* [1], *D. Kartashov* [1], *M. Zürch* [1], *R. Röder* [3], *L. Trefflich* [3], *O. Rosmej* [4], *P. Neumayer* [4], *C. Ronning* [3], *and C. Spielmann* [1,2]

[1] Institute for Optics and Quantum Electronics, FSU Jena, Germany; [2] Helmholtz Institute Jena, Germany; [3] Institute of Solid State Physics, FSU Jena, Germany; [4] GSI, Darmstadt, Germany

The interaction of high-energy ultra short laser pulses with nanostructured surfaces has attracted a huge scientific interest due to various optical properties offered by such structures. Among many different investigated nonlinear processes are the generation of dense plasmas for hard x-ray generation acting as a backlighter for plasma heated with a heavy ion beam [1]. To better understand laser matter interaction we studied nanowire targets made of wide bandgap (3.37 eV) semiconductor zinc oxide. In a first step we studied the nonlinear optical response of ZnO nanostructed surfaces irradiated by a laser pulse at the intensity level of 10^{11}–10^{12} W/cm^2, which is an order of magnitude above the range previouly used [2,3].

Experimental details

The experiment setup is shown in Fig. 1. The experiments were carried out with the 1 kHz Ti:Sapphire laser with the pulse duration of 30 fs at a medium wavelength of 800 nm was used. The target is located slightly before focus of a 40 cm-length focusing lens L1 giving the spot size of 1.5 mm. This provides the intensity on a surface which is confidently below the threshold. The collecting system is mounted on a rotating rail with a sample placed on the rotation axis to measure the angular distribution of SHG emission. It consists of a focusing lens L2 and a UV optical fiber attached to a spectrometer (Ocean Optics USB4000 UV-VIS-ES).

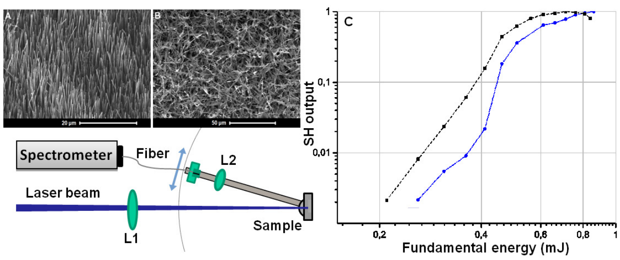

Figure 1: Experimental setup. The insets (A) and (B) shows SEM images of "grass-like" and "spaghetti-like" samples respectively. (C) - normalized SHG yield as a function of the pump energy for the "grass" (black dashed curve) and "spaghetti" (blue dashed-dotted curve) samples.

ZnO nanostructured targets

For the current experiment two morphologically different types of ZnO samples were produced by physical vapour deposition in the group of Prof. Ronning (IFK). The first type – "grass-like" sample –is a disordered array of ZnO crystalline wires with average spacing about 1 μm arranged vertically on a 500 μm thick ZnO substrate deposited on silicon wafer. The diameter of wires is about 350 nm, its average length is several microns. The second type – "spaghetti-like" sample – represents a pile of the similar wires but chaotically arranged along the surface (see the inset of Fig. 1).

Results and discussions

The dependence of SHG spectrum on the pump energy, observation angle and the laser repetition rate were measured. From both types of the samples a strong second harmonic emission with smooth maximum in specular direction was detected. The normalized spectra obtained at 100 Hz repetition rate and 0.9 mJ maximum pump energy are shown in Fig. 1C. At high repetition rate (1 kHz) the heat accumulation effect manifests itself in fluctuation of SHG signal within several seconds.Though the acceptance angle in case of nanostructured surfaces in our measurements was about 1% from the full solid angle, the yield of SHG from the "spaghetti-like" sample is four orders of magnitude higher than the yield from the polished ZnO surface and almost 15 times higher than from the "grass-like" sample. A long with SHG a weak green emission from defects (deep centers) was detected.

In our experiments we observed a strongly non-linear dependence of SHG yield on the pump energy which reaches saturation over 0.5 mJ and, in case of "grass-like" sample, even drops for the higher energies. To the best of our knowledge, such a strong dependence of SHG signal from ZnO nanowires on the pump intensity has not been reported yet. It can be barely explained by a power law and cardinally differs from the square dependence obtained in [4] with lower pump intensities.

References

[1] P. Neumayer, *et al.*, Diagnostic instrumentation for plasma physics experiments at the APPA cave, GSI Technical Design Review (2014)

[2] K. Pedersen, *et al.*, Phys. Status Solidi **5**(8), 2671 (2008)

[3] R. Prasanth, *et al.*, Appl. Phys. Lett. **88**, 181501 (2006)

[4] C. F. Zhang, *et al.*, Appl. Phys. Lett. **89**, 042117 (2006)

* Work supported by HI Jena.

† Zhanna.Samsonova@uni-jena.de

Theory

Proposed determination of small level splittings in highly charged ions

Z. W. Wu[1], *N. M. Kabachnik*[2], *A. Surzhykov*[1], *C. Z. Dong*[3], *and S. Fritzsche*[1,4]
[1]Helmholtz Institute Jena, Germany; [2]European XFEL, Hamburg, Germany; [3]Northwest University Lanzhou, China;
[4]University of Jena, Germany

Highly charged ions (HCI) are known as a unique tool for exploring the interaction of strong electromagnetic fields with matter. In particular the x-ray emission from these ions has been investigated for many years and helped reveal many details about the structure and dynamics of HCI [1]. Moreover, recent studies on the angular distribution and linear polarization of these x-rays provided not only insight into the electron-electron and electron-photon interactions but also showed a rather strong influence of the hyperfine interaction upon the angular x-ray emission of HCI, even if the fine and hyperfine structure of these lines cannot be resolved in detail [2].

Until the present, however, almost all experimental and theoretical investigations on the angular distribution of x-rays have dealt with the photon emission from well-isolated fine-structure levels. In contrast, little attention was paid to cascade emissions that proceed via two (or more) overlapping intermediate resonances. For such cascades, we have therefore explored, by using the density matrix theory, both the photon-photon correlation function as well as the angular distribution of the second photon (if the first photon remains unobserved). General expressions were derived for these distributions, independent of the particular shell structure of the HCI [3]. For the sake of simplicity, let us consider the two-step cascade

$$\begin{aligned} & 1s2p^2 \;\; J_i = 1/2, 3/2 \\ & \quad \longrightarrow \;\; \gamma_1 \; + \left\{ \begin{array}{l} 1s2s2p \;\; J = 1/2 \\ 1s2s2p \;\; J' = 3/2 \end{array} \right\} \\ & \quad \longrightarrow \;\; \gamma_1 \; + \; \gamma_2 \; + \; 1s^2 2s \;\; J_f = 1/2 \end{aligned} \tag{1}$$

of lithium-like ions. These ions have a relatively simple level structure and are known to exhibit a level crossing of the two $1s2s2p$ $J = 1/2, 3/2$ intermediate resonances between $74 \leq Z \leq 79$. For this decay cascade, indeed, a quite remarkable effect of the level splitting and the alignment of the initial $1s2p^2$ $J_i = 3/2$ resonance is found for the angular distribution of the emitted x-ray photons. For lithium-like W^{71+} ions, for example, Fig. 1 displays the angular distribution of the second-step photon emission for an initially aligned $1s2p^2$ $J_i = 3/2$ resonance with (alignment parameter) $\mathcal{A}_2 = -1.0$ and for four different splittings of the intermediate $J = 1/2$ and $3/2$ levels (all in a.u.).

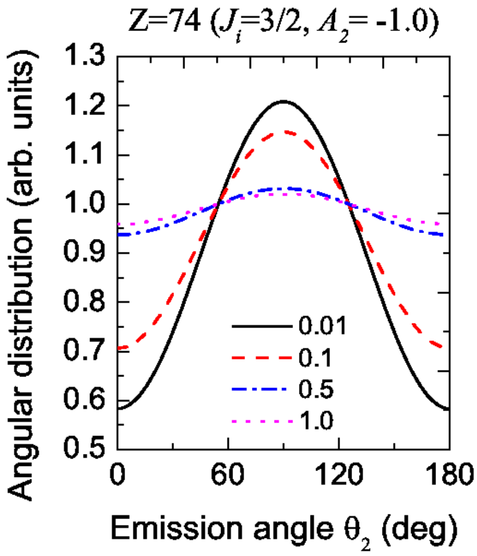

Figure 1: Angular distribution of the second-step photon emission for the cascade (1). See text for further discussions.

When compared with the photon emission of isolated levels, the x-ray emission via overlapping resonances is affected also by spin-spin and spin-orbit interactions that give rise to a depolarization (in time) of these intermediate levels. This effect of partially overlapping resonances upon the emission of photons and electrons has been termed *lifetime-induced depolarization* in the literature. If no further details are known about the exact time interval between the subsequent emission processes in some cascade, this depolarization can be characterized by means of so-called depolarization factors that just depend on the energy splitting and the natural width of the intermediate resonances.

Owing to the strong dependence of the photon-photon correlation and angular distribution functions upon the energy splitting of the intermediate levels, we conclude that accurate measurements of the angular x-ray emission may serve also as a tool for determining small level splittings in highly charged ions [3]. Such measurements of the photon angular distributions will be feasible with present-day x-ray detectors and could be carried out at both, heavy-ion storage rings and electron beam ion trap facilities.

References

[1] S. Fritzsche, P. Indelicato and T. Stöhlker, *J. Phys.* **B38**, S707 (2005).

[2] Z. W. Wu, A. Surzhykov and S. Fritzsche, *Phys. Rev.* **A89**, 022513 (2014).

[3] Z. W. Wu *et al.*, *Phys. Rev.* **A90**, 052515 (2014).

Elastic x–ray scattering by neutral atoms: Outer–shell effects *

A. Surzhykov†1*, V. A. Yerokhin*2*, Th. Stöhlker*1,3,4*, and S. Fritzsche*1,3

1Helmholtz Institute Jena, Germany; 2St. Petersburg State Polytechnical University, Russia; 3University of Jena, Germany; 4GSI Helmholtzzentrum, Darmstadt, Germany

With the recent progress in the setup of high brilliance third–generation synchrotron facilities, new opportunities arise to study the elastic scattering of x–rays by heavy atoms. For photon energies below 1 MeV, the main contribution to this elastic processes arises from the interaction of x–rays with bound atomic electrons. This so–called *Rayleigh* scattering attracts considerable attention as a valuable tool for studying the relativistic, many–body and even quantum electrodynamics (QED) effects in many–electron systems. During the last decades, a large number of experiments have been performed to explore the Rayleigh process for a wide range of photon energies and for various targets. In 2012, for example, the elastic scattering of (linearly polarized) hard x–rays by gold atoms has been observed at the PETRA III synchrotron facility in DESY [1]. To better understand the outcome of this experiment, a theoretical investigation of the elastic $\gamma + A \to \gamma + A$ process is required which would account for both the many–body phenomena and the relativistic non–dipole contributions to the electron–photon interaction.

The theoretical analysis of the elastic Rayleigh scattering is usually performed within the framework of the second–order perturbation theory. In this approach, all the properties of the scattered light can be expressed in terms of the transition amplitudes [2, 3]:

$$\mathcal{M}(\omega) = \sum_{\nu} \frac{\left\langle \psi_i \left| \hat{\mathcal{R}} \right| \psi_\nu \right\rangle \left\langle \psi_\nu \left| \hat{\mathcal{R}} \right| \psi_i \right\rangle}{\epsilon_i - \epsilon_\nu \pm \hbar\omega}\,, \qquad (1)$$

where ψ_i and ϵ_i are the (many–body) wave-function and the energy of the atomic state *before* (as well as *after*) the scattering, $\hbar\omega$ is the photon energy, and $\hat{\mathcal{R}}$ is the electron–photon interaction operator. In Eq. (1), moreover, the summation $\sum_\nu$ runs over the *complete* spectrum of an atom, including not only bound– but also positive and negative energy continuum–states. In order to perform this non–trivial summation over *many–electron* states we employed the independent particle approximation (IPA) in which the photon is scattered by a single (active) electron at a time, while the remaining electrons are kept “frozen” [2, 4].

By making use of Eq. (1) and the independent particle approximation, we have explored the elastic scattering of (completely linearly) polarized x–rays by heavy atoms [4]. In this study, special attention was paid to the question of how various atomic shells contribute to the Rayleigh process. In Fig. 1 we display, for example, the angle–differential Rayleigh cross section for the led target and the incident radiation with energy $\hbar\omega = 145$ keV. In our calculations, we have restricted the summation over the occupied electron shells to the K (red dotted line), KL (maroon dash–dotted line), KLM (green dash–dot–dot line), KLMN (blue dashed line) and the KLMNO shells (black solid line). As seen from the figure, the x–ray scattering by weakly bound outer–shell electrons may dramatically affect the differential cross section. The most pronounced effect can be observed at forward scattering angles, where the cross section is enhanced by more than two orders of magnitude if the interaction of incident radiation with (sub–) valence electrons is taken into account. We argue, therefore, that the angular–resolved measurements of the elastic Rayleigh process, as currently performed at the PETRA III facility, may provide valuable information about electronic shell structure of heavy atoms.

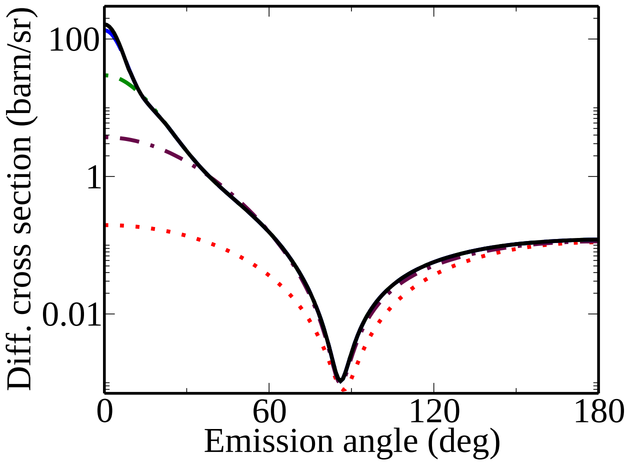

Figure 1: The angle–differential cross section for the elastic scattering of linearly polarized photons with energy $\hbar\omega$ = 145 keV by neutral lead atom. Calculations have been performed within the framework of the independent particle approximation and by taking various atomic shells into account. See text for further details. Data from Ref. [4].

References

[1] K. H. Blumenhagen *et al.*, this Annual Report (2015).

[2] S. C. Roy *et al.*, Rad. Phys. Chem. **56**, 1 (1999).

[3] A. Surzhykov *et al.*, Phys. Rev. A **88**, 062515 (2013).

[4] A. Surzhykov *et al.*, submitted to J. Phys. B.

* Work is supported by the BMBF under the project No. 05K13VHA.

† a.surzhykov@gsi.de

Dielectronic recombination of rubidium-like tungsten ions

Z. W. Wu[1,2]*, Y. Z. Zhang*[2]*, Y. B. Fu*[2]*, A. Surzhykov*[1]*, S. Fritzsche*[1,3]*, and C. Z. Dong*[2]
[1]Helmholtz Institute Jena, Germany; [2]Northwest Normal University, Lanzhou, China; [3]University of Jena, Germany

Owing to its high melting point, low sputtering rate and low absorption of tritium, tungsten has been utilized as a plasma-facing material in magnetically confined fusion facilities. Most recently, it was considered as a leading candidate for the divertor and main chamber regions of the International Thermonuclear Experimental Reactor (ITER) tokamak. Inevitably, tungsten ions are expected to be prominent impurities in fusion plasmas. The emitted radiation from excited tungsten leads to substantial plasma cooling that has to be well controlled in order to maintain conditions for nuclear fusion. In addition, dielectronic recombination (DR) is an important atomic process in such plasmas in which an initially free electron is captured by a target ion under simultaneous excitation of one of its bound electrons. This leads to a doubly excited state of the ion that may subsequently stabilize by photon emission. Accurate DR cross sections and rate coefficients are essential for simulating ionization balance of highly charged ions in high-temperature plasmas. Therefore, studies on the DR of tungsten ions have attracted much attention.

In the isolated-resonance approximation, if we assume that the electron velocity obeys the Maxwellian distribution in plasmas, DR rate coefficients can be given by

$$\alpha^{DR}(kT_e) = \left(\frac{2\pi\hbar^2}{m_e kT_e}\right)^{3/2} \frac{g_j}{2g_i} \, A^a_{ji} \, B^r_{j,f} \, \exp\left(-\frac{E_{ij}}{kT_e}\right). \quad (1)$$

Here, kT_e is the electron temperature, E_{ij} the resonance energy, g_i and g_j the statistical weights of initial and intermediate states, respectively. Moreover, $B^r_{j,f}$ denotes the radiative branching ratio and is defined in terms of the Auger decay rate A^a_{ji} and the radiative decay rate A^r_{jf}.

In order to learn importance of different subshell excitations, we perform *ab initio* calculations for DR of Rb-like W^{37+} through the intermediate doubly excited configurations [Ne]$(3s^2 3p^6 3d^{10})^{-1} 4s^2 4p^6 4d \, nl \, n^{'} l^{'}$ with $n^{'} \leq 16$ and $l^{'} \leq 9$, and [Ne]$3s^2 3p^6 3d^{10} (4s^2 4p^6 4d)^{-1} \, nl \, n^{'} l^{'}$ with $n^{'} \leq 18$ and $l^{'} \leq 12$, while the contribution from other configurations with larger $n^{'} l^{'}$ is estimated by using the extrapolation procedures [1]. In Figure 1, we display total DR rate coefficients of initially W^{37+} ions together with partial contributions as associated with excitations of the $3s$, $3p$, $3d$, $4s$, $4p$, and $4d$ subshells as functions of the electron temperature. These coefficients are calculated for electron temperatures from 1 eV to 5×10^4 eV. Each partial contribution to total DR rate coefficients is given here by the sum of rate coefficients for the doubly excited configurations [Ne]$(3s^2 3p^6 3d^{10} 4s^2 4p^6 4d)^{-1} nln^{'} l^{'}$ with all permitted nl and $n^{'} l^{'}$ combinations. As seen clearly in Figure 1, the excitation of $4p$ subshell dominates total DR rate coefficients in the whole region of electron temperature.

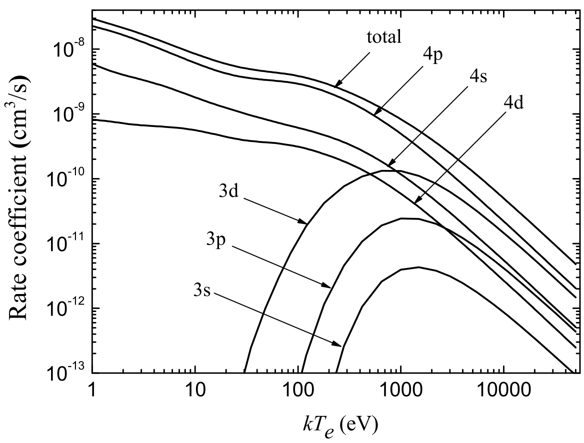

Figure 1: Total DR rate coefficients of initially Rb-like W^{37+} ion and the partial contributions associated with the excitations of $3s$, $3p$, $3d$, $4s$, $4p$ and $4d$ subshells as functions of the electron temperature kT_e. Each partial contribution gives the sum of rate coefficients for all DR channels corresponding to the excitations from nl subshells.

With respect to the excitation of $3l$ subshells, it is found that the DR rate coefficients for the excitation from $3d$ subshell are the largest and that the corresponding DR rate coefficients decrease with the quantum number l. For electron temperatures lower than 100 eV, the excitations of $3l$ subshells are much less significant than the ones of $4l$, and so its contributions to total DR rate coefficients can be neglected. However, as the electron temperature increases, the DR rate coefficients for the excitations of $3l$ subshells start to compete with their counterparts for the $4l$. This behavior arises mainly because of the influence of near-threshold states, since their resonance energies are quite small and since the DR rate coefficients have an $\exp(-E_{ij}/kT_e)$ dependence. Regarding the excitation of $4l$ subshells, the rate coefficients for the $4p$ excitation are the largest, while the contribution from $4s$ and $4d$ subshells cannot be neglected. The largest contributions to the total DR rate coefficients can reach 8% and 21% for the excitations from $4d$ and $4s$ subshells, respectively, even for electron temperatures below 100 eV.

References

[1] Z. W. Wu *et al.*, Eur. Phys. J. D, submitted (2014).

Polarization of atomic bremsstrahlung in coincidence studies *

R. A. Müller† [1,2], *V. A. Yerokhin* [3], *and A. Surzhykov* [2]

[1]Friedrich-Schiller-University Jena, Jena, Germany; [2]Helmholtz-Institute Jena, Jena, Germany; [3]Saint-Petersburg State Polytechnical University, St. Petersburg, Russia

The deceleration of an electron accompanied by the emission of a photon in the stationary field of an atom or ion is called *atomic* or *ordinary* bremsstrahlung. During the last decades investigations on this topic where mostly dedicated to the properties of the emitted bremsstrahlung photons while the scattered electron remained unobserved. Only a few studies have been performed considering coincident observation of the emitted photon and the scattered electron (see Ref. [1] and references therein). However the polarization of the emitted bremsstrahlung photons in such coincidence studies has not been investigated yet. A fortiori not for the scattering of spin polarized electrons.

In our previous work [2] we introduced a theory based on a density matrix approach and first order perturbation theory for the description of bremsstrahlung. We modified this theory to obtain results for coincidence scenarios. With this theory we achieve excellent agreement with experimental findings [1,3]. Moreover we applied it to perform detailed calculations for the polarization of bremsstrahlung if observed in coincidence with the scattered electron.

Within our theory the bremsstrahlung polarization, represented by the Stokes parameters P_i, is parametrized in terms of the final state photon density matrix

$$\frac{\langle \mathbf{k}\lambda|\hat{\varrho}_f(\mathbf{p}_i,\mathbf{p}_f)|\mathbf{k}\lambda'\rangle}{\sum_{\tilde{\lambda}}\langle \mathbf{k}\tilde{\lambda}|\hat{\varrho}_f(\mathbf{p}_i,\mathbf{p}_f)|\mathbf{k}\tilde{\lambda}\rangle} = \frac{1}{2}\begin{pmatrix} 1+P_3 & P_1-iP_2 \\ P_1+iP_2 & 1-P_3 \end{pmatrix}, \tag{1}$$

where we consider the emission of a photon with momentum $\mathbf{k}$ and helicity λ. Because the circular polarization is hard to access in the considered parameter range we focus on the linear polarization characterized by P_1 and P_2. In order to achieve a direct comparability with experimental data, we display in Fig. 1 not the Stokes parameters themselves but the degree of linear polarization $P_L = \sqrt{P_1^2+P_2^2}$ and the polarization angle $\chi = 1/2\arctan(P_2/P_1)$. In our calculations for Fig. 1 we fixed the electron scattering angle to $\theta_p = 90°$ (solid line). For comparison results are shown obtained under the assumption that the scattered electron is not observed (dashed line). In both cases we considered a completely polarized incident electron beam. It can be seen in Fig. 1 that the degree of linear polarization (upper panel) is remarkably increased compared to the case where the outgoing electron is unobserved. A similar difference is seen in the lower panel of Fig. 1 where even the sign of the polarization angle χ is changed if the electron scattering angle is fixed.

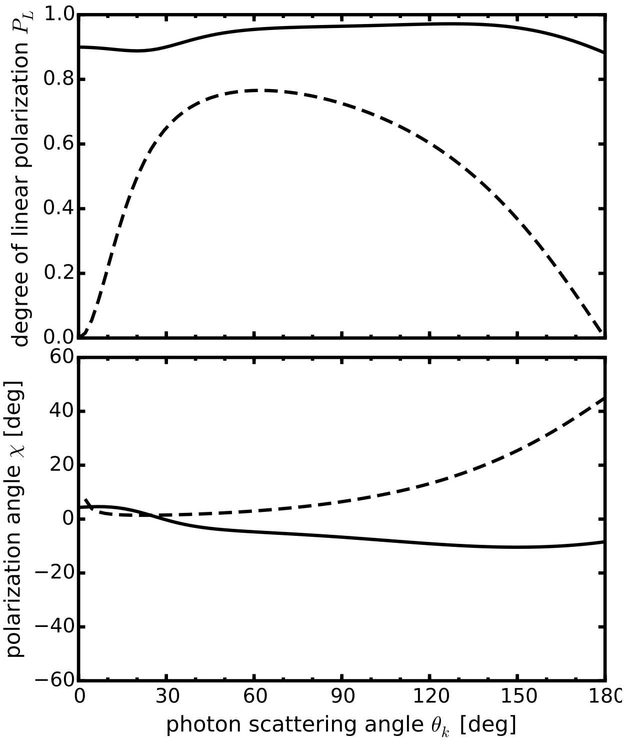

Figure 1: Degree of linear polarization P_L (upper panel) and polarization angle χ (lower panel) of bremsstrahlung radiation from a gold target as a function of the photon emission angle θ_k in a coplanar geometry. The incident electron energy is $\varepsilon_i = 100$keV and the final energy $\varepsilon_f = 1$keV. For details, see text and Ref. [1]

In summary we have developed a theory to describe the properties of bremsstrahlung in scenarios where the emitted bremsstrahlung photon is observed in coincidence with the scattered electron. We achieve a very good agreement with experiments [1,3] and predict an almost complete linear polarization of bremsstrahlung in particular coincidence scenarios.

* Work supported by the Helmholtz-Institute Jena and the Helmholtz Association under the project Nachwuchsgruppe VH-NG-421 as well as the Studienstiftung des Deutschen Volkes.

† robert.rm.mueller@uni-jena.de

References

[1] R. A. Müller, V. A. Yerokhin and A. Surzhykov, Phys. Rev. A **90**, 032707 (2014).

[2] V. A. Yerokhin and A. Surzhykov, Phys. Rev. A **82**, 062702 (2010).

[3] P.-M. Hillenbrand et al., Phys. Rev. A **90**, 022707 (2014).

Laser photon merging in an electromagnetic field inhomogeneity

H. Gies[1,2], *F. Karbstein*[1,2], *and R. Shaisultanov*[3]

[1]Helmholtz-Institut Jena, Germany; [2]Theoretisch-Physikalisches Institut, FSU Jena, Germany; [3]Nazarbayev University, Republic of Kazakhstan

We study the effect of laser photon merging, or equivalently high harmonic generation, in the quantum vacuum subject to inhomogeneous electromagnetic fields. Such a process is facilitated by the effective nonlinear couplings arising from charged particle-antiparticle fluctuations in the quantum vacuum in strong electromagnetic fields. We derive explicit results for general kinematic and polarization configurations involving optical photons. Concentrating on merged photons in reflected channels which are preferable in experiments for reasons of noise suppression, we demonstrate that photon merging is typically dominated by the competing nonlinear process of quantum reflection, though appropriate polarization and signal filtering could specifically search for the merging process. As a byproduct, we devise a novel systematic expansion of the photon polarization tensor in plane wave fields.

The discovery of quantum vacuum nonlinearities [1] under controlled laboratory conditions using real photons or macroscopic electromagnetic fields is a major goal of contemporary strong-field physics. Many proposals rely on a pump-probe scheme, where a well-controlled, say optical, photon beam probes a region of space that is exposed to a strong field ("pump"). A typical example is given by schemes intended to verify vacuum birefringence that can be searched for using macroscopic magnetic fields or with the aid of high-intensity lasers.

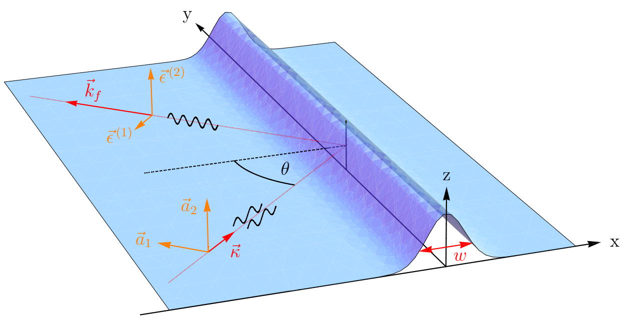

Figure 1: Schematic depiction of the two-photon merging process. Incident probe photons (wave vector $\vec{\kappa}$, energy $|\vec{\kappa}|$) hit a one-dimensional magnetic field inhomogeneity $\vec{B}(\mathrm{x}) = B(\mathrm{x})\vec{e}_{\mathrm{z}}$ of width w under an angle of θ. Due to nonlinear effective couplings between electromagnetic fields mediated by virtual charged particle fluctuations, the field inhomogeneity can impact incident probe photons to merge and form an outgoing photon (wave-vector $\vec{k}_f$) of twice the energy of the incident probe photons. Most notably, the inhomogeneity can affect the outgoing merged photons to reverse their momentum component along $\vec{e}_{\mathrm{x}}$ with respect to the incident probe photons.

The pump-probe scheme is typically also reflected by the theoretical description, in which the nonlinearities are kept for the pump-probe interaction, but the equations are linearized with respect to the probe propagation. In the present work, we rely again on an optical pump-probe setup which however requires a nonlinear treatment of the probe-field. The idea is to look for laser photon merging in the presence of an electromagnetic field inhomogeneity. This effect resembles the standard nonlinear optical process of *second harmonic generation* (SHG) – or in general *high harmonic generation* – with the nonlinear crystal replaced by the quantum vacuum subject to strong electromagnetic fields.

Laser photon merging in proton-laser collisions have been investigated in detail in [2], where a promising scenario has been proposed for a discovery of the merging phenomenon that involves a nowadays conventional optical high-intensity laser at a high-energy proton collider.

In the present work [3], we concentrate on an "all-optical" parameter regime realizable with high-intensity lasers. As the signal is expected to be very small, we consider specifically the kinematics of the reflection process for an appropriate signal-to-noise reduction. We limit ourselves to the study of time-independent field inhomogeneities, such that there is no energy transfer from the field inhomogeneity. Depending on the spatial field inhomogeneity, the propagation direction of the merged photons can differ from that of the incident probe photons. For the specific reflecting kinematic situation, the merged photons can even propagate – somewhat counter-intuitively – into the backward direction. For a straightforward comparison of the signals resulting from quantum reflection [4] and the photon merging scenario of this work, we focus on a one-dimensional magnetic field inhomogeneity. Our findings confirm the expectation that the merging process for the reflective scenario is dominated by the quantum reflection process for the all-optical parameter regime. Nevertheless, due to a different polarization and frequency dependence, filtering techniques might allow for a discovery of the merging process in this set up as well.

References

[1] W. Heisenberg and H. Euler, Z. Phys. **98**, 714 (1936).

[2] A. Di Piazza, K. Z. Hatsagortsyan and C. H. Keitel, Phys. Rev. Lett. **100**, 010403 (2008) and Phys. Rev. A **78**, 062109 (2008).

[3] H. Gies, F. Karbstein and R. Shaisultanov, Phys. Rev. D **90**, no. 3, 033007 (2014).

[4] H. Gies, F. Karbstein and N. Seegert, New J. Phys. **15**, 083002 (2013).

Quantum reflection of photons off spatio-temporal electromagnetic field inhomogeneities

Holger Gies[1,2], *Felix Karbstein*[1,2], *and Nico Seegert*[1,2]

[1]Helmholtz Institut Jena, Fröbelstieg 3, D-07743 Jena, Germany; [2]Theoretisch-Physikalisches Institut, FSU Jena, Max-Wien-Platz 1, D-07743 Jena, Germany

Photons which traverse an inhomogeneous electromagnetic field region can experience quantum reflection. We extend our previous theoretical investigation to include time-dependent field inhomogeneities varying in two spatial directions, allowing us to approximately describe quantum reflection for a realistic experimental scenario employing high-intensity lasers.

The vacuum of quantum electrodynamics (QED) is predicted to behave like a polarizable medium, facilitating nonlinear interactions between electromagnetic fields as they can couple to virtual electron-positron fluctuations [1]. Proposed signatures like vacuum birefringence, light-by-light scattering and photon splitting depend on the intensities involved and are suppressed by powers of $I/I_{\rm cr}$, where $I_{\rm cr} \approx 5\times10^{29}\,{\rm W/cm^2}$. Recent advancements in the development of high-intensity laser facilities exceeding intensities of $10^{22}\,{\rm W/cm^2}$ put the experimental verification of purely optical vacuum signatures in reach for the first time.

Recently, we introduced quantum reflection as an additional optical signature of the QED vacuum nonlinearity [2]. We envisaged a setup which employs the crossing of two high-intensity lasers in a pump-probe type set-up: The pump laser creates in its focal spot a strong, inhomogeneous electromagnetic field ("background"), which modifies the vacuum to act as an effective, attractive potential for traversing probe photons. The inhomogeneous background profile causes some probe photons to get reflected, which can then be measured by a suitably placed detector. Probe photons carrying the signature are therefore inherently separated from photons unaffected by the nonlinearity.

While [2] served to establish the effect by dealing with a purely magnetic field inhomogeneity $\vec{B}(\mathrm{x})$ varying only along a single spatial direction, in [3] we extended the formalism to deal with a plenitude of backgrounds, including those resembling more closely the focal spots of real lasers (see Fig 1). Starting from the effective, one-loop QED-action for constant background fields, we incorporated the inhomogeneity on the level of the polarization tensor. Such a locally constant field approximation requires the background fields to vary on scales much larger than the Compton's wavelength $\lambda_c = 1/m_e \approx 3.9\times10^{-13}$m and time $\tau_c = 1/m_e \approx 10^{-21}$s. In order not to spoil gauge invariance we identified settings "p" depending on the specific inhomogeneity under consideration, which leave the polarization of the probe beam unchanged. This requirement is in fact the only impediment to extending the formalism to arbitrary background fields.

For the setting depicted in Fig. 1, among others, we derived scattering coefficients in the limit of small field-

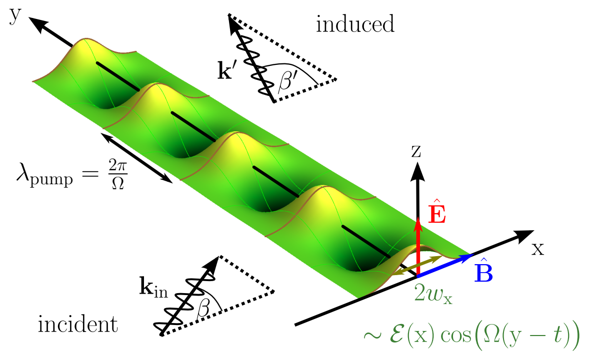

Figure 1: Quantum reflection for a 2 + 1 dimensional field inhomogeneity $\mathcal{E}(\mathrm{x},\mathrm{y},t)$. The background field propagates along y with frequency Ω, and falls off to zero asymptotically for large values of $|\mathrm{x}|$. The background electric and magnetic field are perpendicular to each other, and to the propagation direction y. The probe photons with wave vector $\vec{k}_{\rm in}$ hit the inhomogeneity under an angle β. The induced photons with wave vector $\vec{k}'$ are measured by a suitably placed detector.

strength ratios $\mathcal{E}/\mathcal{E}_{\rm cr} \ll 1$ and for arbitrary frequencies $\omega_{\rm in}$ of the probe photon beam,

$$R^{(\pm)}_{p,2n} = \Theta(k^2_{\mathrm{x},2n})\left|\frac{\alpha}{\pi}\frac{c_p(1+\delta_{n0})}{360}\frac{\omega^2_{\rm in}(1-\sin\beta)^2}{k_{\mathrm{x},2n}}\right. \\ \left.\times\int \mathrm{dx}\, \mathrm{e}^{i(\omega_{\rm in}\cos\beta\pm|k_{\mathrm{x},2n}|)\mathrm{x}}\left(\frac{e\mathcal{E}(\mathrm{x})}{m^2}\right)^2\right|^2, \quad (1)$$

with $k^2_{\mathrm{x},2n} = (\omega_{\rm in}-2n\Omega)^2 - (\omega_{\rm in}\sin\beta - 2n\Omega)^2$. Due to frequency mixing, the induced photon signature is made up of contributions with energies $\omega_{\rm in} - 2n\Omega$, where $n \in \{-1,0,1\}$. Quantum reflection is exponentially suppressed with the momentum transfer onto the probe photon, and hence forward scattering $(-)$ usually dominates over backward scattering $(+)$.

We employ parameters of contemporary high-intensity lasers with peak powers of $P = 1$PW for order-of-magnitude estimates. Results are promising and corroborate the robustness of the effect with respect to generalizations of the inhomogeneity. Hence, quantum reflection can be established as a promising candidate to probe QED vacuum nonlinearities.

References

[1] W. Heisenberg and H. Euler, Z. Phys. **98**, 714 (1936).

[2] H. Gies, F. Karbstein and N. Seegert, New J. Phys. **15**, 083002 (2013) [arXiv:1305.2320 [hep-ph]].

[3] H. Gies, F. Karbstein and N. Seegert, arXiv:1412.0951 [hep-ph].

Phase Structure of Many-Flavor QED$_3$

J. Braun[1,2], *H. Gies*[3,4], *L. Janssen*[5], *and D. Roscher*[1]

[1]TU Darmstadt, Germany; [2]EMMI, GSI, Darmstadt, Germany; [3]HI Jena, Germany; [4]TPI, FSU Jena, Germany; [5]Simon Fraser University, British Columbia, Canada

Quantum Electrodynamics (QED) underlies many relevant physical systems as the theoretical basis on a fundamental level. In addition to atomic physics and the high-intensity frontier, many layered condensed-matter systems require QED as an effective description of essential long-range properties. In turn, strong correlations which are difficult to realize at the high-intensity frontier can become accessible in many-body systems. This project has addressed the chiral-symmetry-breaking phase transition in many-flavor 2+1 dimensional QED, providing first indications for the existence of a Lorentz-breaking intermediate phase.

The competition between screening and anti-screening effects is at the heart of the intriguing diversity of phases occurring in asymptotically free theories. Not only thermal phase transitions governed by parameters such as temperature or chemical potentials, but also quantum phase transitions triggered by the number of active degrees of freedom have recently been of central interest. Most prominently, the number of light fermion degrees of freedom N_f often serves as a control parameter to tune the screening–anti-screening competition. One of the simplest models supporting such a competition is $2+1$ dimensional QED (QED$_3$), which has gained significance also from application to graphene, surface states of 3-dimensional topological insulators, and high-temperature cuprate superconductors. Whereas a chiral phase transition is also expected to occur in $3+1$ dimensional QED at highest intensities due to electromagnetic catalysis, being beyond any foreseeable reach, chiral symmetry breaking in QED$_3$ can be associated with the zero-temperature transition from the d-wave superconducting state into the antiferromagnetic state.

In this project [1], we analyzed the many-flavor phase diagram of QED$_3$. We computed the critical flavor number above which the theory is in the quasi-conformal massless phase. For this, we studied the renormalization group fixed-point structure in the space of gauge interactions and fermionic self-interactions, the latter of which are induced dynamically by electron-photon interactions. We find that a reliable estimate of the critical flavor number crucially relies on a careful treatment of the Fierz ambiguity in the fermionic sector. Using a Fierz-complete basis, our results indicate that the phase transition towards a chirally-broken phase occurring at small flavor numbers could be separated from the quasi-conformal phase at larger flavor numbers, allowing for an intermediate phase which is dominated by fluctuations in a vector channel. If these interactions approach criticality, the intermediate phase could be characterized by a Lorentz-breaking vector condensate.

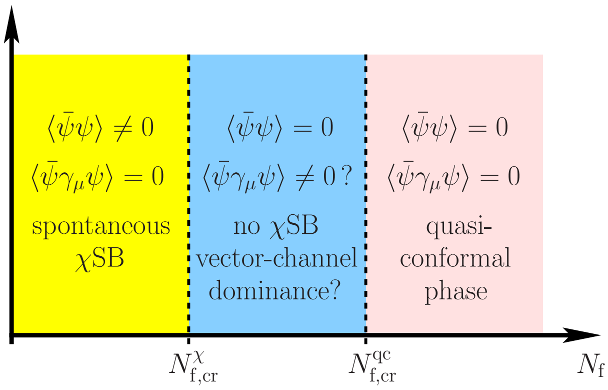

Figure 1: Sketch of the many-flavor phase diagram of QED$_3$. In addition to the phase governed by spontaneous chiral symmetry breaking (χSB) for small values of N_f, an intermediate phase driven by the vector-channel may exist, possibly exhibiting (spontaneous) breaking of Lorentz symmetry.

For large $N_\mathrm{f} > N_{\mathrm{f,cr}}^{\mathrm{qc}}$, the system is in a quasi-conformal phase which is indicative for an algebraic-Fermi-liquid phase, with striking consequences to the electronic, optical, and thermodynamic experimental observables. At $N_{\mathrm{f,cr}}^{\mathrm{qc}}$ which is characterized by a merger of the Gaußian and the "Thirring" fixed point, the system behaves similar to 4-dimensional many-flavor QCD, which gives rise to Kosterlitz-Thouless-type scaling behavior. Below a second critical flavor number $N_\mathrm{f} < N_{\mathrm{f,cr}}^{\chi}$, we observe chiral symmetry breaking. Our estimates for the critical flavor numbers, $N_{\mathrm{f,cr}}^{\chi} \simeq 4$, and $N_{\mathrm{f,cr}}^{\mathrm{qc}} \approx 4.1\ldots10.0$, entail the possibility of an intermediate phase for $N_{\mathrm{f,cr}}^{\chi} < N_\mathrm{f} < N_{\mathrm{f,cr}}^{\mathrm{qc}}$, which is vector-channel dominated. This phase could be characterized by a Lorentz-breaking vector condensate and a corresponding excitation spectrum with photonlike Goldstone bosons as well as a massive radial-type mode.

While it is certainly not inconceivable that $N_{\mathrm{f,cr}}^{\chi}$ and $N_{\mathrm{f,cr}}^{\mathrm{qc}}$ are in fact identical, we see no natural reason for this coincidence to hold. The fact that such an intermediate phase has so far been overlooked, is indicative for the fact that even such simple theories as QED can support a diversity of physical phenomena at the stong-correlation/high-intensity frontier.

References

[1] J. Braun, H. Gies, L. Janssen and D. Roscher, Phys. Rev. D **90**, no. 3, 036002 (2014) [arXiv:1404.1362 [hep-ph]].

Narrowband inverse Compton scattering x-ray sources at high laser intensities

D. Seipt[*1,2], *S. G. Rykovanov*[1,2], *A. Surzhykov*[1,2], *and S. Fritzsche*[2,3]

[1]Helmholtz-Institut Jena, Fröbelstieg 3, 07743 Jena; [2]GSI Helmholtzzentrum für Schwerionenforschung, Planckstraße 1, 64291 Darmstadt; [3]Universität Jena, Institut für Theoretische Physik, 07743 Jena

Bright narrowband x- and gamma-ray sources based on the inverse Compton scattering of laser light on high-energy electron beams rely on the Doppler upshift of the laser frequency $\omega' = 4\gamma^2\omega_0$. However, these sources suffer from a limitation of the maximum laser intensity because the longitudinal ponderomotive force in a high-intensity laser pulse will effectively slow-down the electrons, reducing their γ-factor. This gradual slow-down of the electrons as the intensity ramps up leads to a reduced Doppler up-shift causing spectral broadening of the generated x- or gamma-rays. Recent results [1, 2, 3] suggest that this ponderomotive broadening could be compensated by suitably chirped laser pulses. This compensation would allow to reduce the bandwidth of the generated x- and gamma-rays and to operate narrowband Compton sources in the high-intensity regime. Here we report on our recent findings on the determination of the optimal frequency modulation and its properties.

Let us assume a high-energy electron with asymptotic four-momentum p (and $\gamma \gg 1$) collides head-on with an intense short laser pulse propagating along the direction $n = (1, 0, 0, -1)$, described by the normalized vector potential $a^\mu = a_0 \varepsilon^\mu g(x^+) \cos \Phi(x^+)$. The laser is assumed to be chirped with a local frequency $\omega(x^+) = \partial\Phi/\partial x^+$, with the light-front time $x^+ = t + z$, and where g denotes the laser's envelope function that changes slowly on the time-scale $1/\omega$. When the electron enters the laser pulse, its momentum has to be supplemented by the pondermotive four-potential

$$p^\mu \to p^\mu + U^\mu\,, \quad U^\mu = \frac{m a_0^2 g^2(x^+)}{4\gamma} n^\mu\,, \tag{1}$$

that describes the longitudinal slow-down.

From the analysis of the scattering amplitude of nonlinear Compton scattering within the framework of strong-field QED in the Furry picture [3] we find the *local* frequency of the ℓ-th harmonic of the scattered x-rays as

$$\omega'_\ell = \frac{4\gamma^2 \ell \omega(x^+)}{1 + \gamma^2\vartheta^2 + \frac{a_0^2 g^2(x^+)}{2} + \chi(x^+)}\,, \tag{2}$$

where $\chi = 2\ell\omega\gamma/m$ denotes the electron recoil, and ϑ is the scattering angle. From Eq. (2) we can determine the optimal laser chirp via the condition $\mathrm{d}\omega'_\ell/\mathrm{d}x^+ = 0$. In other words: The optimal chirping prescription

$$\frac{\omega(x^+)}{\omega_0} = 1 + \frac{1}{1+\gamma^2\vartheta^2} \frac{a_0^2}{2} g^2(x^+) \tag{3}$$

* d.seipt@gsi.de

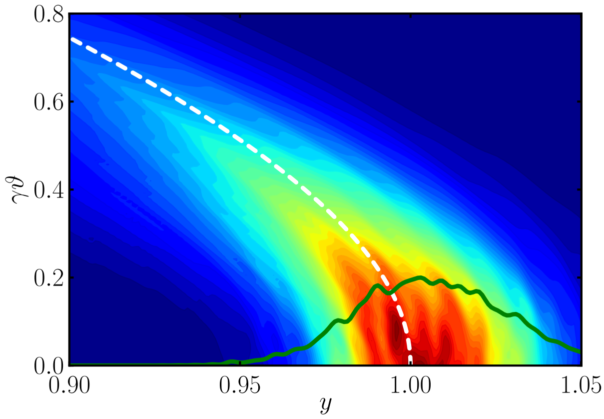

Figure 1: Simulated energy and angular radiation spectrum of a realistic electron beam interacting with a focused laser pulse with peak intensity $a_0 = 2.83$. The solid green line depicts the on-axis line-out of the radiation spectrum ($y = \omega'/4\gamma^2\omega_0$). For simulation parameters cf. Ref. [3].

describes how the laser frequency needs to increase during the time of high laser intensity in order to exactly balance the ponderomotive red-shift due to the slow-down of the electrons. Eq. (3) shows that the ponderomotive broadening can be compensated only for just one particular scattering angle ϑ. Moreover, the form of the optimal frequency modulation, Eq. (3), does not depend on the electron recoil during the scattering (no dependence on χ) and it removes the ponderomotive broadening from all higher harmonics in addition to the fundamental line (no dependence on ℓ). A numerical simulation of the compensated nonlinear Compton spectrum taking into account realistic laser focus geometries and electron bunches shows a reduction of the bandwidth from 80% to less than 5%, see Fig. 1.

To summarize, our analysis shows that the compensation of ponderomotive broadening by chirped laser pulses is a promising route towards operating narrowband Compton scattering x- and gamma-ray sources at high laser intensity.

References

[1] I. Ghebregziabher, B. A. Shadwick, and D. Umstadter, Phys. Rev. ST Accel. Beams **16**, 030705 (2013),

[2] B. Terzić, K. Deitrick, A. S. Hofler, and G. A. Krafft, Phys. Rev. Lett. **112**, 074801 (2014).

[3] D. Seipt, S. G. Rykovanov, A. Surzhykov and S. Fritzsche, arXiv:1412.2659.

Plasma undulator based on laser excitation of wakefields in a plasma channel*

S.G. Rykovanov†[1,2], *C.B. Schroeder*[2], *E. Esarey*[2], *C.G.R. Geddes*[2], *and W.P. Leemans*[2]
[1]Helmholtz Institute Jena, Jena, Germany; [2]Lawrence Berkeley National Laboratory, Berkeley, USA

Undulator magnets have numerous applications in beam physics, including the production of synchrotron radiation, the cooling of particle beams, and the production of coherent radiation via the free electron laser mechanism [1]. The wavelength λ of the radiation produced by an electron undergoing oscillations inside an undulator is $\lambda = \lambda_u \left(1 + K^2/2\right)/2\gamma^2$, where λ_u is the undulator period, γ is the Lorentz factor of the electron, and K is the undulator strength parameter. Presently, the lower limit to the undulator period for magnetic undulators with $K \sim 1$ is on the order of 5 mm [1]. Reducing λ_u is highly beneficial as it will decrease the required electron energy for the same specified radiation wavelength and, hence, decrease the size of the light source. In this work we propose a micro-undulator based on controlling the transverse forces experienced by an electron beam inside a laser-excited plasma channel. Plasma waves with the appropriate transverse fields can be created by initiating laser pulse centroid oscillations in the channel [2].

Laser pulse guiding inside a plasma channel at relativistic intensities (i.e. $I\lambda_L \approx 10^{18}\mathrm{W/cm}^2\mu\mathrm{m}^2$, where I and λ_L and laser pulse intensity and wavelength respectively) is routinely performed for efficient electron acceleration inside LPAs [3,4]. Consider a preformed plasma density profile that is assumed to be parabolic in the direction transverse to the laser propagation

$$n(r) = n_0\left[1 + (\Delta n/n_0)r^2/w_0^2\right], \qquad (1)$$

with r the transverse coordinate, n_0 the on-axis electron density, w_0 the laser spot size and Δn the channel depth. For moderate laser intensities, the laser spot size will remain constant during the propagation in such a channel and will be equal to w_0 if the channel depth is equal to $\Delta n = \left(\pi r_e w_0^2\right)^{-1}$, where $r_e = e^2/mc^2$ is the classical electron radius [5]. If the laser pulse enters the channel off-axis or under some angle, the laser beam centroid will oscillate as it propagates with characteristic length equal to Rayleigh range $Z_R = \pi w_0^2/\lambda_L$. The laser beam centroid oscillates according to

$$x_c(z) = x_{ci}\cos(z/Z_R + \varphi), \qquad (2)$$

where x_{ci} is maximum centroid displacement and φ is an arbitrary phase.

An illustration of the plasma undulator is depicted on Fig. 1: A short laser pulse (depicted with red color) is propagating through the plasma channel and exhibits oscillatory motion due to an initial centroid displacement. Wakefields created in the plasma also follow the oscillatory motion. An electron beam injected behind the laser pulse (depicted by a collection of points) experiences transverse, thus focusing field (lower panel). The periodically changing focusing field serves as an undulator and the oscillating electrons produce radiation.

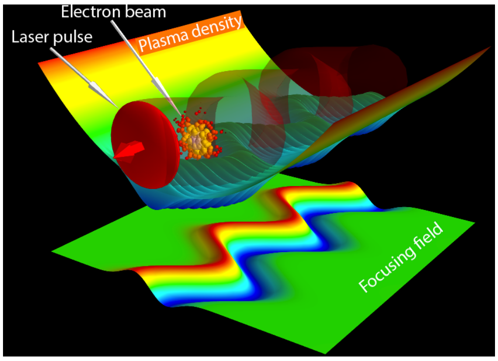

Figure 1: Schematic of the plasma undulator.

Using the linear plasma theory, one can derive the structure of the plasma wakefield driven by the laser pulse undergoing the centroid oscillations, trajectories of injected electrons and, hence, the undulator parameters [2]. Specifically, the plasma undulator wavelength and strength parameter are given by

$$\lambda_u = 2\pi^2 w_0^2/\lambda_L, \quad K \approx 10\, a_0^2 x_{ci}/\lambda_L. \qquad (3)$$

One can see, that undulator strength on the order of unity can be achieved for undulators with a period on the order of 1 mm, i.e. for laser pulse spot size $w_0 = 7\mu$m with $\lambda_L = 0.8\mu$m. For sufficiently high quality electron beams FEL instability can develop, leading to generation of partially coherent XUV/X-ray light. This may open a way to a compact, table-top FEL facility affordable to smaller laboratories working in biology, chemistry and material science.

References

[1] J. Clarke,"The Science and Technology of Undulators and Wigglers", Oxford University Press, 2004

[2] S.G. Rykovanov, *et al.*, accepted to Phys. Rev. Lett. (2015)

[3] C.G.R. Geddes, *et al.*, Phys. Rev. Lett, 95, 145002 (2005)

[4] W.P. Leemans, *et al.*, Nature Physics, 2, 696 (2006)

[5] E. Esarey, C.B. Schroeder, and W.P. Leemans, Rev. Mod. Phys., 81, 1229 (2009)

* Work supported in part by Helmholtz-Nachwuchsgruppe VH-NG-1037.

† s.rykovanov@gsi.de

Carrier-envelope-phase effects in high-order harmonics generation from overdense plasma surfaces*

S. Tietze[1], *M. Yeung*[1], *M. Zepf*[1,2], *and S.G. Rykovanov*[†1]
[1]Helmholtz Institute Jena, Jena, Germany; [2]Queen's University Belfast, UK

Overdense plasma (typically fully ionised solid density targets) irradiated by the relativistically intense short laser pulses is a source of attosecond XUV and X-ray pulses. This is due to the interplay between the $\vec{v} \times \vec{B}$ and restoring forces, which lead to the plasma surface oscillations [1]. A pulse reflected from such a Relativistically Oscillating Mirror (ROM) consists of periodic bursts of attosecond XUV pulses leading to appearance of the high-order harmonics in the reflected spectrum [2, 3].

We developed a simple single particle analytical model to describe the dynamics of a plasma surface irradiated by intense laser pulses under the normal incidence. Comparing the results of the model calculations to the 1D particle-in-a-cell (PIC) simulations, we find our model in good agreement (Fig. 1).

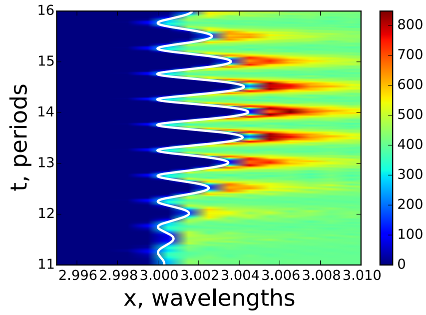

Figure 1: Comparison between spatio-temporal density distribution obtained by 1D PIC simulation and single particle model (white line).

It is known that carrier envelope phase (CEP) plays an important role in generation of attosecond pulses from atomic media [4]. For instance, it is important to use "cosine"-pulses for isolation of a single attosecond pulse. We show that for isolation of a single attosecond pulse generated from a ROM in the normal incidence geometry unexpectedly one has to use "sine"-pulses instead.

To derive an analytic expression for the field on the surface of the plasma, we consider a single incompressible electron layer, which is bound to the immobile ion layer. We take the superposition of the incident, reflected and transmitted field on the plasma surface to derive an expression for the field, which is driving the electron. For the incident laser pulse with transverse electric field component $E_y(t,x) = -E_0 \cos(\omega_L t - k_L x)$, we obtain the driving electric field

$$E_{\mathrm{dr}}(t,x) = \frac{2E_0}{\sqrt{1+n/n_{cr}}} \cos(\omega_L t - k_L x_p + \alpha), \quad (1)$$

where E_0, ω_L, k_L are laser pulse electric field amplitude, frequency and wavenumber, respectively, n is the target density, n_{cr} is the critical density, x_p is the location of the plasma boundary and $\alpha = \arctan(\sqrt{n/n_{cr}})$ is a phase shift depending on the density of the target. For overdense targets α approaches $\pi/2$, which leads to a shift from a sine to a cosine pulse and vice versa.

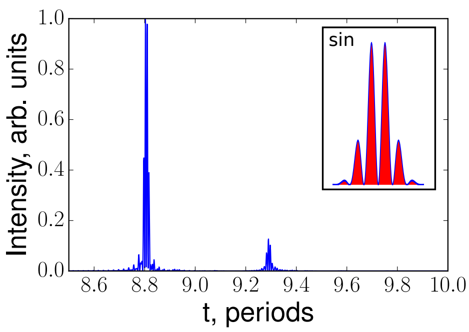

Figure 2: Reflected pulse, after filtering from the 40th to 100th harmonic. Inlet: Incident sine pulse used.

With the 1D PIC code PICWIG, we obtained the spectrum of the reflected intense two-cycle laser pulse. It contains high order harmonics, as predicted by the ROM model. Filtering reflected pulse in spectral domain from 40th to 100th harmonic, we observe 2 attosecond pulses for "cosine" incident laser pulse and a single attosecond pulse for a "sine" incident laser pulse (see Fig. 2). This is in contrast to the case of atomic medium where "cosine" pulse leads to a single attosecond emission.

In conclusion, we have derived an expression for the phase shift for the fields driving the plasma surface. Our result can have important consequences for CEP stabilised experiments aiming at generation of single attosecond pulses.

References

[1] S.V Bulanov, *et al.*, Phys. Plasmas 1, 745 (1994)

[2] R. Lichters, *et al.*, Phys. Plasmas 3, 3425 (1996)

[3] Dromey, *et al.*, Phys. Rev. Lett. 99 085001 (2007)

[4] F. Krausz and M. Ivanov, Rev. Mod. Phys. 81, 163 (2009)

* Work supported by Helmholtz-Nachwuchsgruppe VH-NG-1037.
† s.rykovanov@gsi.de

Numerical modeling of the electron–positron cascades in the strong electromagnetic fields*

V. Yu. Kharin† *and S. G. Rykovanov*
Helmholtz Institute, Jena, Germany

Intensities of the modern lasers will in the near future give us the possibility of observing essentially quantum electrodynamical effects in the laser field. One of the most fascinating effects (and probably the best studied one) is the particle production by colliding photons [1]. To provide such an event, the total energy of photons must be larger than two times the rest mass of the electron. Hence one needs either hard gamma–quanta or a large number of photons. Another interesting effect that has been described analytically is the nonlinear Compton scattering [2]. Electron in the electromagnetic field can absorb multiple photons and emit one quantum of very high energy. These two effects combined together can lead to cascade pair production in the intense laser field (that is repeating sequential nonlinear Compton scattering and electron-positron pair production during the interaction between scattered gamma quantum and incident field), which is currently the subject of intensive research [3,4].

The common procedure for the numerical simulation of electron–positron cascade development is the following [3]. At each time step the integration of the equations of motion for every particle is performed and rates of particle creation are calculated. It is essential that the inequality

$$W\Delta t \ll 1 \tag{1}$$

holds to exclude multiple emissions inside one time step. Here W is the corresponding rate [5] (of photon production or of pair production) and Δt is the time step. After that two random numbers are generated: one is to decide whether the production took place; another one is to extract the product energies from the probability distribution. Due to the complicated structure of the probability distributions and the necessity of their recalculation at each time step, the described simulation procedure is computationally expensive and has a few drawbacks.

To increase the accuracy of the numerical solution of motion equations we implemented the implicit integration routine based on two stage Runge–Kutta–Nyström method with iterating [6]. It demonstrates better stability and convergence than explicit Runge–Kutta methods. Restriction on the time step for Monte–Carlo evaluation can be overcome by using non-uniform time grid for every electron. This means that we do not trace the validity of (1). Instead, assuming that parameter variations are small within one step, we trace the probability that no single quantum event has occurred to the particle, i. e. we choose the random number $0 < r < 1$ and check whether

$$r < e^{-W\Delta t}. \tag{2}$$

If this inequality is false, then we calculate the time of the first event and the energy of products. Using this condition allows us to use arbitrary large time steps for Monte–Carlo routine. Since the non–uniform time grid is used, we can start integrating for the products exactly at that moment of time. Using these methods significantly improves algorithm performance.

Our numerical algorithm allows analyzing cascade pair production in arbitrary field configuration. Figure 1 demonstrates preliminary results obtained with our code. They correspond to the cascade produced from a single electron in the uniformly rotating electric field with frequency 1eV and amplitude of $a_0 = 10^4$. At relatively large timescale system demonstrates exponential growth of the pair number. Cascade rate can be obtained from the slope on Fig. 1.

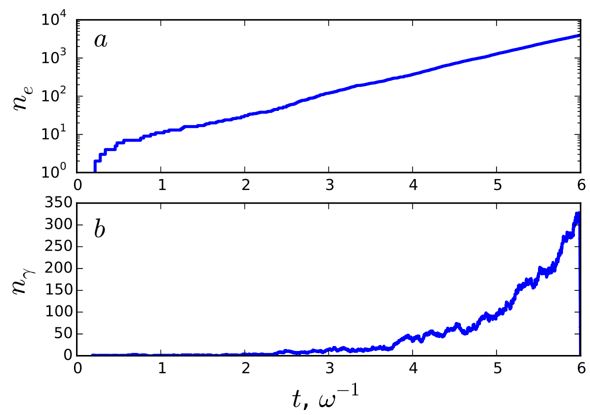

Figure 1: Time dependence of the concentrations of electrons (a) and γ–quanta (b)

References

[1] A. R. Bell and J. G. Kirk, Phys. Rev. Let. 101, 200403 (2008)
[2] F. Makenroth, A. Di Piazza, Phys. Rev. A 83, 032106 (2011)
[3] N. Elkina et. al, Phys. Rev. ST Accel. Beams 14, 054401 (2011)
[4] E. N. Nerush et al, Phys. Rev. Lett. 106, 035001 (2011)
[5] A. I. Nikishov and V. I. Ritus, Sov. Phys. JETP 19, 529 (1964)
[6] N. V. Elkina, A. M. Fedotov, C. Herzing, H. Ruhl, Phys. Rev. E 89, 053315 (2014)

* Work supported by Helmholtz-Nachwuchsgruppe VH-NG-1037.
† v.kharin@gsi.de

Publications

A. Alejo, S. Kar, H. Ahmed, A. G. Krygier, D. Doria, R. Clarke, J. Fernandez, R. R. Freeman, J. Fuchs, A. Green, J. S. Green, D. Jung, A. Kleinschmidt, C. L. S. Lewis, J. T. Morrison, Z. Najmudin, H. Nakamura, G. Nersisyan, P. Norreys, M. Notley, M. Oliver, M. Roth, J. A. Ruiz, L. Vassura, M. Zepf, and M. Borghesi
Characterisation of deuterium spectra from laser driven multi-species sources by employing differentially filtered image plate detectors in Thomson spectrometers
Review of Scientific Instruments **85**, 093303 (2014).

A. Artemyev, V. Serbo, and A. Surzhykov
Double lepton pair production with electron capture in relativistic heavy-ion collisions
The European Physical Journal C **74**, 2829 (2014).

B. Aurand, B. Elkin, L.-O. Heim, B. Lommel, B. Kindler, M. Tomut, C. Rödel, S. Kuschel, O. Jäckel, and T. Kühl
Ultra-thin polymer foils for laser-ion acceleration
Journal of Radioanalytical and Nuclear Chemistry **299**, 965 (2014).

B. Aurand, S. Kuschel, O. Jäckel, C. Rödel, H. Zhao, S. Herzer, A. Paz, J. Bierbach, J. Polz, B. Elkin, A. Karmakar, P. Gibbon, M. C. Kaluza, and T. Kühl
Enhanced radiation pressure-assisted acceleration by temporally tuned counter-propagating pulses
Nuclear Instruments and Methods in Physics Research Section A: Accelerators, Spectrometers, Detectors and Associated Equipment **740**, 83 (2014).

D. Banaś, P. Jagodziński, M. Pajek, A. Gumberidze, A. Surzhykov, and Th. Stöhlker
Monte-Carlo simulations of the radiative recombination of ions with electrons in cold magnetized plasma
Physica Scripta **T161**, 014001 (2014).

W. Becker, S. P. Goreslavski, D. B. Milošević, and G. G. Paulus
Low-energy electron rescattering in laser-induced ionization
Journal of Physics B: Atomic, Molecular and Optical Physics **47**, 204022 (2014).

A. Blinne, and H. Gies
Pair production in rotating electric fields
Physical Review D **89**, 085001 (2014).

R. Bödefeld, M. Hornung, J. Hein, and M. C. Kaluza
High precision elimination of angular chirp in CPA laser systems with large stretching factors or high bandwidth
Applied Physics B **115**, 419 (2014).

A. Bondarevskaya, E. A. Mistonova, K. N. Lyashchenko, O. Yu. Andreev, A. Surzhykov, L. N. Labzowsky, G. Plunien, D. Liesen, F. Bosch, and Th. Stöhlker
Method for the production of highly charged ions with polarized nuclei and zero total electron angular momentum
Phyical Review A **90**, 064701 (2014).

B. Botermann, D. Bing, C. Geppert, G. Gwinner, T. Hänsch, G. Huber, S. Karpuk, A. Krieger, T. Kühl, W. Nörtershäuser, C. Novotny, S. Reinhardt, R. Sanchez, D. Schwalm, T. Stöhlker, A. Wolf, and G. Saathoff
Test of Time Dilation Using Stored Li^+ Ions as Clocks at Relativistic Speed
Physical Review Letters **113**, 120405 (2014).

J. Braun, H. Gies, L. Janssen, and D. Roscher
Phase structure of many-flavor QED_3
Physical Review D **90**, 036002 (2014).

S. Breitkopf, T. Eidam, A. Klenke, L. v. Grafenstein, H. Carstens, S. Holzberger, E. Fill, T. Schreiber, F. Krausz, A. Tünnermann, I. Pupeza, and J. Limpert
A concept for multiterawatt fibre lasers based on coherent pulse stacking in passive cavities
Light: Science & Applications **3**, e211 (2014).

C. R. D. Brown, D. O. Gericke, M. Cammarata, B. I. Cho, T. Döppner, K. Engelhorn, E. Förster, C. Fortmann, D. Fritz, E. Galtier, S. H. Glenzer, M. Harmand, P. Heimann, N. L. Kugland, D. Q. Lamb, H. J. Lee, R. W. Lee, H. Lemke, M. Makita, A. Moinard, C. D. Murphy, B. Nagler, P. Neumayer, K.-U. Plagemann, R. Redmer, D. Riley, F. B. Rosmej, P. Sperling, S. Toleikis, S. M. Vinko, J. Vorberger, S. White, T. G. White, K. Wünsch, U. Zastrau, D. Zhu, T. Tschentscher, and G. Gregori
Evidence for a glassy state in strongly driven carbon
Scientific Reports **4**, 5214 (2014).

S. Busold, A. Almomani, V. Bagnoud, W. Barth, S. Bedacht, A. Blažević, O. Boine-Frankenheim, C. Brabetz, T. Burris-Mog, T. Cowan, O. Deppert, M. Droba, H. Eickhoff, U. Eisenbarth, K. Harres, G. Hoffmeister, I. Hofmann, O. Jäckel, R. Jäger, M. Joost, S. Kraft, F. Kroll, M. Kaluza, O. Kester, Z. Lecz, T. Merz, F. Nürnberg, H. Al-Omari, A. Orzhekhovskaya, G. Paulus, J. Polz, U. Ratzinger, M. Roth, G. Schaumann, P. Schmidt, U. Schramm, G. Schreiber, D. Schumacher, T. Stöhlker, A. Tauschwitz, W. Vinzenz, F. Wagner, S. Yaramyshev, and B. Zielbauer
Shaping laser accelerated ions for future applications – The LIGHT collaboration
Nuclear Instruments and Methods in Physics Research Section A: Accelerators, Spectrometers, Detectors and Associated Equipment **740**, 94 (2014).

S. Busold, K. Philipp, A. Otten, and M. Roth
Image plate characterization and absolute calibration to low kilo-electron-volt electrons
Review of Scientific Instruments **85**, 113306 (2014).

S. Busold, D. Schumacher, O. Deppert, C. Brabetz, F. Kroll, A. Blažević, V. Bagnoud, and M. Roth
Commissioning of a compact laser-based proton beam line for high intensity bunches around 10 MeV
Physical Review Special Topics - Accelerators and Beams **17**, 031302 (2014).

W. Chen, G. Vorobyev, D. Guo, F. Herfurth, P.-M. Hillenbrand, U. Spillmann, S. Trotsenko, A. Gumberidze, and Th. Stöhlker
Metal vapor target for precise studies of ion-atom collisions
Review of Scientific Instruments **85**, 053513 (2014).

D. J. Corvan, G. Sarri, and M. Zepf
Design of a compact spectrometer for high-flux MeV gamma-ray beams
Review of Scientific Instruments **85**, 6 (2014).

H. Dachraoui, G. v. d. Laan, N. Müller, T. Milde, M. Porer, R. Manzke, R. Huber, S. Fritzsche, and U. Heinzmann
Mapping spin-orbit activated interchannel coupling
Europhysics Letters **106**, 13001 (2014).

D. Denis-Petit, M. Comet, T. Bonnet, F. Hannachi, F. Gobet, M. Tarisien, M. Versteegen, G. Gosselin, V. Méot, P. Morel, J.-C. Pain, F. Gilleron, A. Frank, V. Bagnoud, A. Blazevic, F. Dorchies, O. Peyrusse, W. Cayzac, and M. Roth
Identification of X-ray spectra in the Na-like to O-like rubidium ions in the range of 3.8–7.3 Å
Journal of Quantitative Spectroscopy and Radiative Transfer **148**, 70 (2014).

A. Frank, J. Fuchs, L. Lancia, G. Lehmann, J. R. Marques, G. Mourou, C. Riconda, K. H. Spatschek, T. Toncian, L. Vassura, and S. Weber
Amplification of ultra-short light pulses by ion collective modes in plasmas
European Physical Journal Special Topics **223**, 1153 (2014).

S. Fritzsche
The Feynman tools for quantum information processing: Design and implementation
Computer Physics Communications **185**, 1697 (2014).

C. Gaida, F. Stutzki, F. Jansen, H.-J. Otto, T. Eidam, C. Jauregui, O. de Vries, J. Limpert, and Tünnermann
Triple-clad large-pitch fibers for compact high-power pulsed fiber laser systems
Optics Letters **39**, 209 (2014).

H. Gies, F. Karbstein, and R. Shaisultanov
Laser photon merging in an electromagnetic field inhomogeneity
Physical Review D **90**, 033007 (2014).

X. Gong, M. Kunitski, K. J. Betsch, Q. Song, L. Ph. H. Schmidt, T. Jahnke, N. Kling, O. Herrwerth, B. Bergues, A. Senftleben, J. Ullrich, R. Moshammer, G. G. Paulus, I. Ben-Itzhak, M. Lezius, M. F. Kling, H. Zeng, R. R. Jones, and J. Wu
Multielectron effects in strong-field dissociative ionization of molecules
Phyical Review A **89**, 043429 (2014).

M. Gräfe, A. Hoffmann, and C. Spielmann
Ultrafast fluorescence spectroscopy for axial resolution of flurorophore distributions
Applied Physics B **117**, 833 (2014).

D. Gwynne, S. Kar, D. Doria, H. Ahmed, M. Cerchez, J. Fernandez, R. J. Gray, J. S. Green, F. Hanton, D. A. MacLellan, P. McKenna, Z. Najmudin, D. Neely, J. A. Ruiz, A. Schiavi, M. Streeter, M. Swantusch, O. Willi, M. Zepf, and M. Borghesi
Modified Thomson spectrometer design for high energy, multi-species ion sources
Review of Scientific Instruments **85**, 033304 (2014).

S. Hädrich, A. Klenke, J. Rothhardt, M. Krebs, A. Hoffmann, O. Pronin, V. Pervak, J. Limpert, and A. Tünnermann
High photon flux table-top coherent extreme-ultraviolet source
Nature Photonics **8**, 779 (2014).

S. B. Hansen, J. Colgan, A. Ya. Faenov, J. Abdallah, S. A. Pikuz, I. Yu. Skobelev, E. Wagenaars, N. Booth, O. Culfa, R. J. Dance, G. J. Tallents, R. G. Evans, R. J. Gray, T. Kämpfer, K. L. Lancaster, P. McKenna, A. K. Rossall, K. S. Schulze, I. Uschmann, A. G. Zhidkov, and N. C. Woolsey
Detailed analysis of hollow ions spectra from dense matter pumped by X-ray emission of relativistic laser plasma
Physics of Plasmas **21**, 031213 (2014).

P. Hansinger, G. Maleshkov, I. L. Garanovich, D. V. Skryabin, D. N. Neshev, A. Dreischuh, and G. G. Paulus
Vortex algebra by multiply cascaded four-wave mixing of femtosecond optical beams
Optics Express **22**, 11079 (2014).

P. Hansinger, G. Maleshkov, N. Gorunski, N. Dimitrov, A. Dreischuh, and G. G. Paulus
Interaction between one-dimensional dark spatial solitons and semi-infinite dark stripes
Optics Communications **313**, 106 (2014).

A. Hayrapetyan, O. Matula, A. Aiello, A. Surzhykov, and S. Fritzsche
Interaction of Relativistic Electron-Vortex Beams with Few-Cycle Laser Pulses
Physical Review Letters **112**, 134801 (2014).

A. Herrmann, S. Kuhn, M. Tiegel, C. Russel, J. Korner, D. Klopfel, J. Hein, and M. Kaluza
Structure and fluorescence properties of ternary aluminosilicate glasses doped with samarium and europium
Journal of Materials Chemistry C **2**, 4328 (2014).

V. Hilbert, C. Rödel, G. Brenner, T. Döppner, S. Düsterer, S. Dziarzhytski, L. Fletcher, E. Förster, S. H. Glenzer, M. Harmand, N. J. Hartley, L. Kazak, D. Komar, T. Laarmann, H. J. Lee, T. Ma, M. Nakatsutsumi, A. Przystawik, H. Redlin, S. Skruszewicz, P. Sperling, J. Tiggesbäumker, S. Toleikis, and U. Zastrau
Spatio-temporal coherence of free-electron laser radiation in the extreme ultraviolet determined by a Michelson interferometer
Applied Physics Letters **105**, 101102 (2014).

P.-M. Hillenbrand, S. Hagmann, D. Atanasov, D. Banaś, K.-H. Blumenhagen, C. Brandau, W. Chen, E. De Filippo, A. Gumberidze, D. L. Guo, D. H. Jakubassa-Amundsen, O. Kovtun, C. Kozhuharov, M. Lestinsky, Yu. A. Litvinov, A. Müller, R. A. Müller, H. Rothard, S. Schippers, M. S. Schöffler, U. Spillmann, A. Surzhykov, S. Trotsenko, N. Winckler, X. L. Yan, V. A. Yerokhin, X. L. Zhu, and Th. Stöhlker
Radiative-electron-capture-to-continuum cusp in U^{88+} + N_2 collisions and the high-energy endpoint of electron-nucleus bremsstrahlung
Phyical Review A **90**, 022707 (2014).

P.-M. Hillenbrand, S. Hagmann, A. B. Voitkiv, B. Najjari, D. Banaś, K.-H. Blumenhagen, C. Brandau, W. Chen, E. De Filippo, A. Gumberidze, D. L. Guo, C. Kozhuharov, M. Lestinsky, Yu. A. Litvinov, A. Müller, H. Rothard, S. Schippers, M. S. Schöffler, U. Spillmann, S. Trotsenko, X. L. Zhu, and Th. Stöhlker
Electron-loss-to-continuum cusp in U^{88+} + N_2 collisions
Phyical Review A **90**, 042713 (2014).

A. Hoffmann, M. Zürch, M. Gräfe, and C. Spielmann
Spectral broadening and compression of sub-millijoule laser pulses in hollow-core fibers filled with sulfur hexafluoride
Optics Express **22**, 12038 (2014).

M. Hornung, H. Liebetrau, A. Seidel, S. Keppler, A. Kessler, J. Körner, M. Hellwing, F. Schorcht, D. Klöpfel, A. K. Arunachalam, G. A. Becker, A. Sävert, J. Polz, J. Hein, and M. C. Kaluza
The all-diode-pumped laser system POLARIS – an experimentalist's tool generating ultra-high contrast pulses with high energy
High Power Laser Science and Engineering **2**, e20 (2014).

M. Huttula, S.-M. Huttula, S. Fritzsche, P. Lablanquie, F. Penent, J. Palaudoux, and L. Andric
Core-valence double photoionization of atomic mercury
Phyical Review A **89**, 013411 (2014).

P. Jagodziński, M. Pajek, D. Banaś, H. Beyer, M. Trassinelli, and Th. Stöhlker
Ray-tracing simulations of spherical Johann diffraction spectrometer for in-beam X-ray experiments
Nuclear Instruments and Methods in Physics Research Section A: Accelerators, Spectrometers, Detectors and Associated Equipment **753**, 121 (2014).

T. Jahrsetz, S. Fritzsche, and A. Surzhykov
Inelastic Raman scattering of light by hydrogenlike ions
Phyical Review A **89**, 042501 (2014).

D. Jakubassa-Amundsen, R. Müller, A. Surzhykov, and V. Yerokhin
Relativistic theory for radiative forward electron emission in heavy ion-atom encounters
The European Physical Journal D **68**, 367 (2014).

F. Karbstein
Quark-antiquark static energy from a restricted Fourier transform
Journal of High Energy Physics **4**, 144 (2014).

F. Karbstein, A. Peters, and M. Wagner
$\Lambda_{\overline{\mathrm{MS}}}^{(n_f=2)}$ from a momentum space analysis of the quark-antiquark static potential
Journal of High Energy Physics **9**, 114 (2014).

S. Keppler, M. Hornung, R. Bödefeld, A. Sävert, H. Liebetrau, J. Hein, and M. C. Kaluza
Full characterization of the amplified spontaneous emission from a diode-pumped high-power laser system
Optics Express **22**, 11228 (2014).

A. Kessler, M. Hornung, S. Keppler, F. Schorcht, M. Hellwing, H. Liebetrau, J. Körner, A. Sävert, M. Siebold, M. Schnepp, J. Hein, and M. C. Kaluza
16.6 J chirped femtosecond laser pulses from a diode-pumped Yb:CaF_2 amplifier
Optics Letters **39**, 1333 (2014).

M. Kienel, A. Klenke, T. Eidam, S. Hädrich, J. Limpert, and A. Tünnermann
Energy scaling of femtosecond amplifiers using actively controlled divided-pulse amplification
Optics Letters **39**, 1049 (2014).

M. Kienel, M. Müller, S. Demmler, J. Rothhardt, A. Klenke, T. Eidam, J. Limpert, and A. Tünnermann
Coherent beam combination of Yb:YAG single-crystal rod amplifiers
Optics Letters **39**, 3278 (2014).

M. Klaiber, E. Yakaboylu, C. Müller, H. Bauke, G. G. Paulus, and K. Z. Hatsagortsyan
Spin dynamics in relativistic ionization with highly charged ions in super-strong laser fields
Journal of Physics B: Atomic, Molecular and Optical Physics **47**, 065603 (2014).

A. Klenke, S. Hädrich, T. Eidam, J. Rothhardt, M. Kienel, S. Demmler, T. Gottschall, J. Limpert, and A. Tünnermann
22 GW peak-power fiber chirped-pulse-amplification system
Optics Letters **39**, 6875 (2014).

A. Klenke, S. Hädrich, M. Kienel, T. Eidam, J. Limpert, and A. Tünnermann
Coherent combination of spectrally broadened femtosecond pulses for nonlinear compression
Optics Letters **39**, 3520 (2014).

C. Kohlfürst, H. Gies, and R. Alkofer
Effective mass signatures in multiphoton pair production
Physical Review Letters **112**, 050402 (2014).

Y. S. Kozhedub, V. M. Shabaev, I. I. Tupitsyn, A. Gumberidze, S. Hagmann, G. Plunien, and Th. Stöhlker
Relativistic calculations of x-ray emission following a Xe-Bi^{83+} collision
Phyical Review A **90**, 042709 (2014).

J. Körner, V. Jambunathan, J. Hein, R. Seifert, M. Loeser, M. Siebold, U. Schramm, P. Sikocinski, A. Lucianetti, T. Mocek, and M. C. Kaluza
Spectroscopic characterization of Yb^{3+}-doped laser materials at cryogenic temperatures
Applied Physics B **116**, 75 (2014).

M. Kübel, A. S. Alnaser, B. Bergues, T. Pischke, J. Schmidt, Y. Deng, C. Jendrzejewski, J. Ullrich, G. G. Paulus, A. M. Azzeer, U. Kleineberg, R. Moshammer, and M. F. Kling
Strong-field control of the dissociative ionization of N_2 O with near-single-cycle pulses
New Journal of Physics **16**, 065017 (2014).

M. Kübel, K. J. Betsch, N. G. Kling, A. S. Alnaser, J. Schmidt, U. Kleineberg, Y. Deng, I. Ben-Itzhak, G. G. Paulus, T. Pfeifer, J. Ullrich, R. Moshammer, M. F. Kling, and B. Bergues
Non-sequential double ionization of Ar: from the single- to the many-cycle regime
New Journal of Physics **16**, 033008 (2014).

H. Liebetrau, M. Hornung, A. Seidel, M. Hellwing, A. Kessler, S. Keppler, F. Schorcht, J. Hein, and M. C. Kaluza
Ultra-high contrast frontend for high peak power fs-lasers at 1030 nm
Optics Express **22**, 24776 (2014).

J. Limpert, A. Klenke, M. Kienel, S. Breitkopf, T. Eidam, S. Hädrich, C. Jauregui, and A. Tünnermann
Performance Scaling of Ultrafast Laser Systems by Coherent Addition of Femtosecond Pulses
IEEE Journal of Selected Topics in Quantum Electronics **20**, 0901810 (2014).

M. Lochmann, R. Jöhren, C. Geppert, Z. Andelkovic, D. Anielski, B. Botermann, M. Bussmann, A. Dax, N. Frömmgen, M. Hammen, V. Hannen, T. Kühl, Y. Litvinov, R. Lopez-Coto, T. Stöhlker, R. Thompson, J. Vollbrecht, A. Volotka, C. Weinheimer, W. Wen, E. Will, D. Winters, R. Sanchez, and W. Nörtershäuser
Observation of the hyperfine transition in lithium-like bismuth $^{209}Bi^{80+}$: Towards a test of QED in strong magnetic fields
Phyical Review A **90**, 030501 (2014).

W. Ma, J. Bin, H. Wang, M. Yeung, C. Kreuzer, M. Streeter, P. Foster, S. Cousens, D. Kiefer, B. Dromey, X. Yan, J. Meyer-ter-Vehn, M. Zepf, and J. Schreiber
Bright Subcycle Extreme Ultraviolet Bursts from a Single Dense Relativistic Electron Sheet
Physical Review Letters **113**, 235002 (2014).

B. Marx, K. S. Schulze, I. Uschmann, T. Kämpfer, O. Wehrhan, H. C. Wille, K. Schlage, R. Röhlsberger, E. Weckert, E. Förster, Th. Stöhlker, and G. G. Paulus
High precision measurement of undulator polarization in the regime of hard x-rays
Applied Physics Letters **105**, 024103 (2014).

O. Matula, A. G. Hayrapetyan, V. G. Serbo, A. Surzhykov, and S. Fritzsche
Radiative capture of twisted electrons by bare ions
New Journal of Physics **16**, 053024 (2014).

M. Möller, F. Meyer, A. M. Sayler, G. G. Paulus, M. F. Kling, B. E. Schmidt, W. Becker, and D. B. Milošević
Off-axis low-energy structures in above-threshold ionization
Phyical Review A **90**, 023412 (2014).

R. A. Müller, V. A. Yerokhin, and A. Surzhykov
Polarization of atomic bremsstrahlung in coincidence studies
Phyical Review A **90**, 032707 (2014).

M. Nicolai, A. Sävert, M. Reuter, M. Schnell, J. Polz, O. Jäckel, L. Karsch, M. Schürer, M. Oppelt, J. Pawelke, and M. C. Kaluza
Realizing a laser-driven electron source applicable for radiobiological tumor irradiation
Applied Physics B **116**, 643 (2014).

H.-J. Otto, A. Klenke, C. Jauregui, F. Stutzki, J. Limpert, and A. Tünnermann
Scaling the mode instability threshold with multicore fibers
Optics Letters **39**, 2680 (2014).

H.-J. Otto, F. Stutzki, N. Modsching, C. Jauregui, J. Limpert, and A. Tünnermann
2 kW average power from a pulsed Yb-doped rod-type fiber amplifier
Optics Letters **39**, 6446 (2014).

M. J. Prandolini, R. Riedel, M. Schulz, A. Hage, H. Höppner, and F. Tavella
Design considerations for a high power, ultrabroadband optical parametricchirped-pulse amplifier
Optics Express **22**, 1594 (2014).

R. Riedel, J. Rothhardt, K. Beil, B. Gronloh, A. Klenke, H. Höppner, M. Schulz, U. Teubner, C. Kränkel, J. Limpert, A. Tünnermann, M. Prandolini, and F. Tavella
Thermal properties of borate crystals for high power optical parametric chirped-pulse amplification
Optics Express **22**, 17607 (2014).

R. Riedel, A. Stephanides, M. J. Prandolini, B. Gronloh, B. Jungbluth, T. Mans, and F. Tavella
Power scaling of supercontinuum seeded megahertz-repetition rate optical parametric chirped pulse amplifiers
Optics Letters **39**, 1422 (2014).

C. Rothhardt, J. Rothhardt, A. Klenke, T. Peschel, R. Eberhardt, J. Limpert, and A. Tünnermann
BBO-sapphire sandwich structure for frequency conversion of high power lasers
Optical Materials Express **4**, 1092 (2014).

J. Rothhardt, S. Hädrich, S. Demmler, M. Krebs, S. Fritzsche, J. Limpert, and A. Tünnermann
Enhancing the Macroscopic Yield of Narrow-Band High-Order Harmonic Generation by Fano Resonances
Physical Review Letters **112**, 233002 (2014).

J. Rothhardt, S. Hädrich, A. Klenke, S. Demmler, A. Hoffmann, T. Gotschall, T. Eidam, M. Krebs, J. Limpert, and A. Tünnermann
53 W average power few-cycle fiber laser system generating soft x rays up to the water window
Optics Letters **39**, 5224 (2014).

J. Rothhardt, M. Krebs, S. Hädrich, S. Demmler, J. Limpert, and A. Tünnermann
Absorption-limited and phase-matched high harmonic generation in the tight focusing regime
New Journal of Physics **16**, 033022 (2014).

S. G. Rykovanov, C. G. R. Geddes, J.-L. Vay, C. B. Schroeder, E. Esarey, and W. P. Leemans
Quasi-monoenergetic femtosecond photon sources from Thomson Scattering using laser plasma accelerators and plasma channels
Journal of Physics B: Atomic, Molecular and Optical Physics **47**, 234013 (2014).

G. Sarri, D. Corvan, W. Schumaker, J. Cole, A. Di Piazza, H. Ahmed, C. Harvey, C. Keitel, K. Krushelnick, S. Mangles, Z. Najmudin, D. Symes, A. Thomas, M. Yeung, Z. Zhao, and M. Zepf
Ultrahigh Brilliance Multi-MeV γ-Ray Beams from Nonlinear Relativistic Thomson Scattering
Physical Review Letters **113**, 224801 (2014).

H. M. Scholz-Marggraf, S. Fritzsche, V. G. Serbo, A. Afanasev, and A. Surzhykov
Absorption of twisted light by hydrogenlike atoms
Phyical Review A **90**, 013425 (2014).

K. S. Schulze, B. Marx, I. Uschmann, E. Förster, Th. Stöhlker, and G. G. Paulus
Determination of the polarization state of x rays with the help of anomalous transmission
Applied Physics Letters **104**, 151110 (2014).

D. Seipt, and B. Kämpfer
Laser-assisted Compton scattering of x-ray photons
Phyical Review A **89**, 023433 (2014).

D. Seipt, A. Surzhykov, and S. Fritzsche
Structured x-ray beams from twisted electrons by inverse Compton scattering of laser light
Phyical Review A **90**, 012118 (2014).

L. Senje, M. Yeung, B. Aurand, S. Kuschel, C. Rödel, F. Wagner, K. Li, B. Dromey, V. Bagnoud, P. Neumayer, M. Roth, C.-G. Wahlström, M. Zepf, T. Kuehl, and D. Jung
Diagnostics for studies of novel laser ion acceleration mechanisms
Review of Scientific Instruments **85**, 113302 (2014).

J. Seres, E. Seres, B. Landgraf, B. Ecker, B. Aurand, A. Hoffmann, G. Winkler, S. Namba, T. Kuehl, and C. Spielmann
Parametric amplification of attosecond pulse trains at 11 nm
Scientific Reports **4**, 4254 (2014).

J. Seres, E. Seres, B. Landgraf, B. Ecker, B. Aurand, T. Kuehl, and C. Spielmann
High-harmonic generation and parametric amplification in the soft X-rays from extended electron trajectories
Scientific Reports **4**, 4234 (2014).

N. I. Shvetsov-Shilovski, E. Räsänen, G. G. Paulus, and L. B. Madsen
Asymmetric photoelectron momentum distributions due to quantum interference in strong-field ionization by a few-cycle pulse
Phyical Review A **89**, 043431 (2014).

C. Spielmann
Electrons take the fast track through silicon
Science **346**, 1293 (2014).

E. Stambulchik, E. Kroupp, Y. Maron, U. Zastrau, I. Uschmann, and G. G. Paulus
Absorption-aided x-ray emission tomography of planar targets
Physics of Plasmas **21**, 033303 (2014).

Th. Stöhlker, Y. Litvinov, A. Bräuning-Demian, M. Lestinsky, F. Herfurth, R Maier, D. Prasuhn, R. Schuch, and M. Steck
SPARC collaboration: new strategy for storage ring physics at FAIR
Hyperfine Interactions **227**, 45 (2014).

F. Stutzki, C. Gaida, M. Gebhardt, F. Jansen, A. Wienke, U. Zeitner, F. Fuchs, C. Jauregui, D. Wandt, D. Kracht, J. Limpert, and Tünnermann
152 W average power Tm-doped fiber CPA system
Optics Letters **39**, 4671 (2014).

N. Tahir, V. Kim, B. Schlitt, W. Barth, L. Groening, I. Lomonosov, A. Piriz, Th. Stöhlker, and H. Vormann
Three-dimensional thermal simulations of thin solid carbon foils for charge stripping of high current uranium ion beams at a proposed new heavy-ion linac at GSI
Physical Review Special Topics - Accelerators and Beams **17**, 041003 (2014).

S. Tashenov, T. Bäck, R. Barday, B. Cederwall, J. Enders, A. Khaplanov, Y. Fritzsche, A. Surzhykov, V. A. Yerokhin, and D. Jakubassa-Amundsen
Electron polarimetry with bremsstrahlung
Journal of Physics: Conference Series **488**, 012057 (2014).

S. Tashenov, D. Banaś, H. Beyer, C. Brandau, S. Fritzsche, A. Gumberidze, S. Hagmann, P.-M. Hillenbrand, H. Jörg, I. Kojouharov, Ch. Kozhuharov, M. Lestinsky, Yu. A. Litvinov, A. V. Maiorova, H. Schaffner, V. M. Shabaev, U. Spillmann, Th. Stöhlker, A. Surzhykov, and S. Trotsenko
Observation of Coherence in the Time-Reversed Relativistic Photoelectric Effect
Physical Review Letters **113**, 113001 (2014).

D. Tiedemann, K. E. Stiebing, D. F. A. Winters, W. Quint, V. Varentsov, A. Warczak, A. Malarz, and Th. Stöhlker
A pulsed supersonic gas jet target for precision spectroscopy at the HITRAP facility at GSI
Nuclear Instruments and Methods in Physics Research Section A: Accelerators, Spectrometers, Detectors and Associated Equipment **764**, 387 (2014).

M. Tiegel, A. Herrmann, S. Kuhn, C. Rüssel, J. Körner, D. Klöpfel, R. Seifert, J. Hein, and M. C. Kaluza
Fluorescence and thermal stress properties of Yb^{3+}-doped alumino silicate glasses for ultra high peak power laser applications
Laser Physics Letters **11**, 115811 (2014).

F. Wagner, S. Bedacht, A. Ortner, M. Roth, A. Tauschwitz, B. Zielbauer, and V. Bagnoud
Pre-plasma formation in experiments using petawatt lasers
Optics Express **22**, 29505 (2014).

F. Wagner, C. João, J. Fils, T. Gottschall, J. Hein, J. Körner, J. Limpert, M. Roth, T. Stöhlker, and V. Bagnoud
Temporal contrast control at the PHELIX petawatt laser facility by means of tunable sub-picosecond optical parametric amplification
Applied Physics B **116**, 429 (2014).

C. Wandt, S. Klingebiel, S. Keppler, M. Hornung, M. Loeser, M. Siebold, C. Skrobol, A. Kessel, S. Trushin, Z. Major, J. Hein, M. C. Kaluza, F. Krausz, and S. Karsch
Development of a Joule-class Yb:YAG amplifier and its implementation in a CPA system generating 1 TW pulses
Laser & Photonics Reviews **8**, 875 (2014).

H. Y. Wang, X. Q. Yan, and M. Zepf
Collimated proton acceleration in light sail regime with a tailored pinhole target
Physics of Plasmas **21**, 063113 (2014).

H. Y. Wang, C. Lin, B. Liu, Z. M. Sheng, H. Y. Lu, W. J. Ma, J. H. Bin, J. Schreiber, X. T. He, J. E. Chen, M. Zepf, and X. Yan
Laser-driven three-stage heavy-ion acceleration from relativistic laser-plasma interaction
Physical Review E **89**, 013107 (2014).

T. G. White, N. J. Hartley, B. Borm, B. J. B. Crowley, J. W. O. Harris, D. C. Hochhaus, T. Kaempfer, K. Li, P. Neumayer, L. K. Pattison, F. Pfeifer, S. Richardson, A. P. L. Robinson, I. Uschmann, and G. Gregori
Electron-Ion Equilibration in Ultrafast Heated Graphite
Physical Review Letters **112**, 145005 (2014).

Z. W. Wu, N. M. Kabachnik, A. Surzhykov, C. Z. Dong, and S. Fritzsche
Determination of small level splittings in highly charged ions via angle-resolved measurements of characteristic x rays
Phyical Review A **90**, 052515 (2014).

Z. W. Wu, A. Surzhykov, and S. Fritzsche
Hyperfine-induced modifications to the angular distribution of the Kα_1 x-ray emission
Phyical Review A **89**, 022513 (2014).

X. Xie, K. Doblhoff-Dier, H. Xu, S. Roither, M. Schöffler, D. Kartashov, S. Erattupuzha, T. Rathje, G. Paulus, K. Yamanouchi, A. Baltuška, S. Gräfe, and M. Kitzler
Selective Control over Fragmentation Reactions in Polyatomic Molecules Using Impulsive Laser Alignment
Physical Review Letters **112**, 163003 (2014).

X. Xie, S. Roither, M. Schöffler, E. Lötstedt, D. Kartashov, L. Zhang, G. G. Paulus, A. Iwasaki, A. Baltuška, K. Yamanouchi, and M. Kitzler
Electronic Predetermination of Ethylene Fragmentation Dynamics
Physical Review X **4**, 021005 (2014).

X. Xie, S. Roither, M. Schöffler, H. Xu, S. Bubin, E. Lötstedt, S. Erattuphuza, A. Iwasaki, D. Kartashov, K. Varga, G. G. Paulus, A. Baltuška, K. Yamanouchi, and M. Kitzler
Role of proton dynamics in efficient photoionization of hydrocarbon molecules
Phyical Review A **89**, 023429 (2014).

V. A. Yerokhin, A. Surzhykov, and S. Fritzsche
Relativistic configuration-interaction calculation of Kα transition energies in berylliumlike iron
Phyical Review A **90**, 022509 (2014).

V. A. Yerokhin, A. Surzhykov, and S. Fritzsche
Relativistic calculations of double K-shell-photoionization cross sections for neutral medium-Z atoms
Phyical Review A **90**, 063422 (2014).

M. Yeung, B. Dromey, S. Cousens, T. Dzelzainis, D. Kiefer, J. Schreiber, J. Bin, W. Ma, C. Kreuzer, J. Meyer-ter-Vehn, M. Streeter, P. Foster, S. Rykovanov, and M. Zepf
Dependence of Laser-Driven Coherent Synchrotron Emission Efficiency on Pulse Ellipticity and Implications for Polarization Gating
Physical Review Letters **112**, 123902 (2014).

U. Zastrau, L. Fletcher, E. Förster, E. Galtier, E. Gamboa, S. Glenzer, P. Heimann, H. Marschner, B. Nagler, A. Schropp, O. Wehrhan, and H. Lee
Bent crystal spectrometer for both frequency and wavenumber resolved x-ray scattering at a seeded free-electron laser
Review of Scientific Instruments **85**, 093106 (2014).

U. Zastrau, and E. Förster
Integrated reflectivity measurements of hydrogen phthalate crystals for high-resolution soft x-ray spectroscopy
Journal of Instrumentation **9**, P09008 (2014).

U. Zastrau, P. Sperling, A. Becker, T. Bornath, R. Bredow, T. Döppner, S. Dziarzhytski, T. Fennel, L. B. Fletcher, E. Förster, C. Fortmann, S. H. Glenzer, S. Göde, G. Gregori, M. Harmand, V. Hilbert, B. Holst, T. Laarmann, H. J. Lee, T. Ma, J. P. Mithen, R. Mitzner, C. D. Murphy, M. Nakatsutsumi, P. Neumayer, A. Przystawik, S. Roling, M. Schulz, B. Siemer, S. Skruszewicz, J. Tiggesbäumker, S. Toleikis, T. Tschentscher, T. White, M. Wöstmann, H. Zacharias, and R. Redmer
Equilibration dynamics and conductivity of warm dense hydrogen
Physical Review E **90**, 013104 (2014).

U. Zastrau, P. Sperling, M. Harmand, A. Becker, T. Bornath, R. Bredow, S. Dziarzhytski, T. Fennel, L. Fletcher, E. Förster, S. Göde, G. Gregori, V. Hilbert, D. Hochhaus, B. Holst, T. Laarmann, H. Lee, T. Ma, J. Mithen, R. Mitzner, C. Murphy, M. Nakatsutsumi, P. Neumayer, A. Przystawik, S. Roling, M. Schulz, B. Siemer, S. Skruszewicz, J. Tiggesbäumker, S. Toleikis, T. Tschentscher, T. White, M. Wöstmann, H. Zacharias, T. Döppner, S. Glenzer, and R. Redmer
Resolving Ultrafast Heating of Dense Cryogenic Hydrogen
Physical Review Letters **112**, 105002 (2014).

V. A. Zaytsev, A. V. Maiorova, V. M. Shabaev, A. V. Volotka, S. Tashenov, G. Plunien, and Th. Stöhlker
Parity-nonconservation effect in the dielectronic recombination of polarized electrons with heavy He-like ions
Physical Review A **89**, 032703 (2014).

M. Zhou, S. Zhao, H. Wang, C. Lin, H. Lu, Y. Lu, T. Tajima, X. He, C. Chen, Y. Gu, and X. Yan
Instability-free ion acceleration by two laser pulses
The European Physical Journal Special Topics **223**, 1031 (2014).

N. A. Zubova, Y. S. Kozhedub, V. M. Shabaev, I. I. Tupitsyn, A. V. Volotka, G. Plunien, C. Brandau, and Th. Stöhlker
Relativistic calculations of the isotope shifts in highly charged Li-like ions
Phyical Review A **90**, 062512 (2014).

M. Zürch, A. Hoffmann, M. Gräfe, B. Landgraf, M. Riediger, and Ch. Spielmann
Characterization of a broadband interferometric autocorrelator for visible light with ultrashort blue laser pulses
Optics Communications **321**, 28 (2014).

M. Zürch, J. Rothhardt, S. Hädrich, S. Demmler, M. Krebs, J. Limpert, A. Tünnermann, A. Guggenmos, U. Kleineberg, and C. Spielmann
Real-time and Sub-wavelength Ultrafast Coherent Diffraction Imaging in the Extreme Ultraviolet
Scientific Reports **4**, 7356 (2014).